Study of the time-dependent CP asymmetry in neutral B meson decays with the Belle detector

DISSERTATION
Presented in Partial Fulfillment of the Requirements for the Degree of Doctor of Science in the Graduate School of Osaka University

Kazutaka Sumisawa
Osaka University

February 2001

Acknowledgment

First, I would like to thank my advisor, Prof. Yorikiyo Nagashima, for giving me a chance to work on research in high energy physics, and his gentle support. I wish to express my gratitude to Prof. A. Maki, Prof. Y. Kuno, Prof. T.Yamanaka, Dr. M. Takita, Dr. T. Hara, and Dr. K. Trabelsi for his helpful advice. I am specially grateful to Dr. D. Jackson for his kind advice and continuous support in the statistical analysis.

I would like to thank all the Belle charmonium, ICPV, flavor tagging, and CP-fit groups for their generous cooperation. I am specially grateful to Prof. K. Abe, Prof. H. Aihara, Prof. Y. Sakai, Dr R. Ito, Dr. H. Hamasaki, Dr. K. Hanagaki, Dr. T. Kawasaki, Dr. J. Suzuki, Dr. S. Schrenk, Dr. H. Tajima, Dr. S. Uno, Mr. K. Behera, Ms. F. Fang, Mr. T. Higuchi, and Mr. J. Tanaka.

I owe thanks to all the member of the Belle SVD and vertexing groups for their help and valuable suggestions. I am specially thankful to Prof. M. Tanaka, Dr. T. Tsuboyama, Dr. Y. Yamada, Mr. M. Yokoyama, Mr. T. Tomura, Mr. T. Nakadaira for their supports in the construction of the Belle SVD.

My thanks go to all the members of the Belle collaboration and the KEKB accelerator group for keeping the experiment stable and providing excellent data.

I express my gratitude to the members of the Nagashima Group at Osaka University for the good companionship and encouragement. Dr. K. Senyo, Mr. S. Hidaka, Mr. M. Yoshida, Mr. J. Ryuko, Mr. T. Hojo, Mr. K. Nitta, Mr. H. Miyake, Ms. Y. Kajiyama, Mr. M. Matumoto, Mr. H. Tagomori, Ms. Y. Ikemoto, Mr. T. Ishikawa, Mr. K. Kurahata and Mr. M. Tuchihashi. I enjoyed the life at the university with them. I am specially thankful to Mr. K. Hara for continuous support in the flavor tagging. I am deeply indebted to Ms. S. Tsuzuki for her encouragement and help.

At the last, I would like to express my special thanks to Dr. Masashi Hazumi. I am sure this thesis did not exist without his help and advice. I have learnt so many things from him through long hours of discussion. I can't thank him enough for his kindness and useful instruction.

Abstract

This thesis describes a study of the time-dependent CP asymmetry using the Belle detector. A sample of 6.3×10^6 $B\bar{B}$ pairs obtained with the KEKB asymmetric electron-positron collider operating at the $\Upsilon(4S)$ resonance is used. The neutral B meson is fully reconstructed via its decay into a CP eigenstate: $J/\psi K_S$, $\psi(2S)K_S$, and $\chi_{c1}K_S$. The flavor of the accompanying B meson is identified mainly from the charge of high-momentum leptons or kaons among its decay products. The time interval between the two decays is determined from the distance between the decay vertices. A maximum likelihood fitting method is used to extract $\sin 2\phi_1$ from the asymmetry in the time interval distribution of 50 $B \to$ charmonium $+ K_S$ events. We obtain

$$\sin 2\phi_1 = 0.58^{+0.51}_{-0.56}(stat.)^{+0.10}_{-0.09}(syst.).$$

This result is consistent with the region allowed by the other experimental data and the Standard Model.

Contents

List of Figures

List of Tables

Chapter 1

Introduction

One of the major unresolved issues in our understanding of the universe is how the present universe, which is composed entirely of matter, evolved from the matter-antimatter-symmetric Big Bang. The laws of the nature have a high degree of symmetry between matter and antimatter. The excess of matter over antimatter is not an easily explained property of the universe. CP violation is a key to the puzzle of the matter dominance in the universe[1].

Since the first observation of CP violation in the neutral kaon system in 1964[2], an enormous amount of theoretical work has been done to try to understand the phenomenon. In a remarkable paper published in 1973, Kobayashi and Maskawa (KM) noted that CP violation could be accommodated in the framework of the Standard Model (SM) only if there were at least six quark flavors, twice the number of quark flavors known at that time[3]. Subsequent discoveries of c, b and t quarks have proven the six-quark KM hypothesis, and the KM model for CP violation is now considered to be an essential part of the SM.

However, the KM scheme is not the only model that can accommodate the CP violation to the SM and in spite of a considerable amount of experimental effort over the past three decades, there remain other theoretical proposals that are consistent with presently-available experimental data.

In 1980, Sanda and Carter pointed out that the KM model contained a possibility of sizable CP violating asymmetries in certain decay modes of the B mesons[4]. An observation of CP violation in B meson decays would strengthen the validity of the KM model. The key to the test of the SM is the measurement of the "unitarity triangle" which shows relations between the Cabibbo-Kabayashi-Maskawa (CKM) matrix elements. The KM model provides definitive predictions for three CP angles, ϕ_1, ϕ_2, ϕ_3, which can be extracted from measurements of asymmetries between B and $\bar{B}^0$ in various decay modes.

The largest observable effects are expected to show up in the difference of the decay rates between B^0 and $\bar{B}^0$ mesons to the same CP eigenstate. A resonance $\Upsilon(4S)$ is a good place to obtain pure samples of B^0 and $\bar{B}^0$. However, the time integrated CP asymmetry would vanish because of C=odd nature of $\Upsilon(4S)$. Therefore measurements of CP asymmetries using $B^0\bar{B}^0$ pairs from $\Upsilon(4S)$ decays must be derived from comparisons of the time evolution of the B^0 and $\bar{B}^0$ decays. The most favorable experimental situation is an asymmetric e^+e^- storage ring at the $\Upsilon(4S)$ resonance[5]. This would boost the decaying B^0 mesons in the laboratory frame, allowing current vertex measurement technology to measure the time order of $B^0\bar{B}^0$ decay pairs, even with the short B meson flight distance. The proper time difference Δt is given by

$$\Delta t \simeq \Delta z / c\beta\gamma,$$

where $\beta\gamma$ is the Lorentz boost factor due to the asymmetric beam energy, c the speed of light and Δz is the distance between the decay vertices of the two B mesons along the beam direction. In addition to the feasibility of the measurement of the proper time distribution, the asymmetric e^+e^- collider on $\Upsilon(4S)$ is expected to provide a large number of $B^0\bar{B}^0$ pairs. Hence it will become possible to obtain a sizable number of fully-reconstructed B decays into CP eigenstates in spite of the fact that each decay has a typical branching ratio of 10^{-4}.

The KEK B-factory has been constructed to achieve the goal specified above. The accelerator, referred to as KEKB, promises to provide the luminosity of $10^{34}\mathrm{cm}^{-2}\mathrm{s}^{-1}$ with asymmetric $\Upsilon(4S)$ production at a $\beta\gamma$ of 0.425 (with 8.0GeV electrons on 3.5 GeV positrons). In this condition, the mean decay length of B meson would be $\sim 200\mu$m. It is therefore possible to measure the dependence of the relative decay time of two B mesons on the CP asymmetry. A total number of 10^8 $\Upsilon(4S)$ in a year is expected, from which one can perform a precise measurement of the CP violating parameters in the CKM matrix. For example in $B^0 \to J/\psi K_S$, the asymmetry, A, is related to the CP angle ϕ_1 as

$$A(\Delta t) = \frac{\Gamma(\bar{B}^0(\Delta t) \to J/\psi K_S) - \Gamma(B^0(\Delta t) \to J/\psi K_S)}{\Gamma(\bar{B}^0(\Delta t) \to J/\psi K_S) + \Gamma(B^0(\Delta t) \to J/\psi K_S)} = \sin 2\phi_1 \cdot \sin(\Delta m_B \Delta t)$$

where Δm_B is the mass difference of two mass eigenstates of B^0 meson. The resolution of vertex measurement directly affects the accuracy of CP angle measurement. The detector, referred to as Belle, must be capable of efficient reconstruction of extremely rare exclusive final states of B mesons. This requirement places a premium on solid angle coverage, charged particle momentum resolution, particle species identification, detection efficiency of photons with good resolution.

Among the three CP angles of unitarity triangle, ϕ_1 is expected to be the most accessible experimentally, and its measurement is one of the primary goals of the B-factory experiment. The decay $B^0 \to J/\psi K_S$ is generally considered to be the cleanest channel for measuring ϕ_1. This is because of the fact that its final state, namely J/ψ decays into a pair of leptons and K_S into a pair of charged pions, is essentially background-free, and its decay diagram is dominated by a single diagram, allowing a straightforward extraction of CP angle. For the precise measurement, however, we need a large sample and therefore we have incorporated other similar decay modes such as, $B^0 \to \psi(2S)K_S$ and $B^0 \to \chi_{c1}K_S$, all of them provide alternative possibilities for measuring ϕ_1.

The importance of the research of CP violation in B decays is reflected in the number of laboratories engaged in the measurement of the asymmetry of B decays. The BaBar[6] experiment at SLAC and the HERAB[7] experiment at DESY are taking data with competitive schedules with Belle. Other projects addressing to this physics are also planned at the Tevatron collider[8] and at LHC[9]. A goal of the Belle experiment is to establish the CP violation in B decays.

The Belle experiment commenced taking data in June 1999. The integrated luminosity accumulated by July 2000 is 6.8 fb^{-1} where 6.2 fb^{-1} was taken on the $\Upsilon(4S)$ resonance and 0.6 fb^{-1} off the resonance, and 6.3×10^6 $B\bar{B}$ pairs were created. In this thesis, we present a study for the measurement of the time dependent CP asymmetry and extract $\sin 2\phi_1$ from the decay mode, $B \to \text{charmonium} + K_S$ using data sample taken in June 1999 - July 2000.

The outline of this thesis is as follows: Physics formalism for CP violation is given in Chapter 2. An overview of the experimental apparatus, the KEKB accelerator, the Belle detector, and software are described in Chapter 3. Reconstruction of $B \to \text{charmonium} + K_S$ is explained in Chapter 4. The CP asymmetry parameter $\sin 2\phi_1$ is estimated in Chapter 5, with the evaluation of the statistical and systematic errors. Finally, the conclusion of this thesis is given in Chapter 6.

Chapter 2

CP violation in B meson decays

The violation of CP symmetry is one of the most interesting topics of high-energy physics today. Experimentally, it is one of the least tested properties of the Standard Model. This chapter explains a basic theory of CP violation in B decays and ways to measure the angles of the unitarity triangle. First of all, we explain the discovery of CP violation in K decays in Section 2.1. After describing phenomenology of mixing-induced CP violation in B decays, we discuss the origin of CP violation and Cabibbo-Kobayashi-Maskawa matrix in the framework of the Standard Model in Section 2.3. The expected magnitude of the mixing-induced CP violation based on the present experimental constraints is also given. In the end the basis of the measurement of mixing-induced CP violation at an asymmetric B-factory is described in Section 2.4.

2.1 Discovery of CP violation

In quantum theory, there are conservation laws corresponding to discrete transformations. One of these is reflection in space ("parity operation") **P**. Invariance of laws of nature under **P** means that a mirror image experiment yields the same result in its reflected frame of reference as the original experiment in the original frame of reference. This means that "left" and "right" cannot be defined in an absolute sense.

Similarly, the particle-antiparticle conjugation **C** transforms each particle into its antiparticle, by which all additive quantum numbers change their sign. **C** invariance of laws means that experiments in a **C**-conjugate world consisting mainly of antiparticles will give identical results as the one in our world provided all names of particles are "anti" relative to ours.

A third transformation of this kind is time reversal **T**, which reverses momenta and angular momenta. This formally corresponds to an inversion of direction of time. According to the CPT theorem of Lüders and Pauli[10] there is a connection among these three transformations such that under rather weak assumptions in a local field theory, all processes are invariant under the combined operation **CPT**.

For a long time it was assumed that all the elementary processes are also invariant under the application of each of the three operation **C**, **P**, and **T** separately. However, the work of Lee and Yang[11] questioned this assumption, and the subsequent experiments demonstrated the violation of **P** and **C** invariance in weak decays of nuclei[12] and of pions and muons[13, 14]. At that time **CP** was still considered to be invariant, replacing the separate **P** and **C** invariance of weak interactions.

One consequence of this postulated CP invariance for the neutral K mesons was predicted by Gell-Mann and Pais: there should be a long-lived partner to known $V^0(K_1^0)$ particle of short lifetime ($\sim 10^{-10}$ sec). According to this proposal these two particles are mixtures of two strangeness eigenstates, $K^0(S=+1)$ and $\bar{K}^0(S=-1)$ produced in strong interactions. Weak interactions do not conserve strangeness and the physical particles should be eigenstates of CP if the weak interactions are CP invariant. These eigenstates are(with $\bar{K}^0 = \mathbf{CP}K^0$)

$$\begin{aligned} \mathbf{CP}K_1 = \mathbf{CP}[(K^0+\bar{K}^0)/\sqrt{2}] = (\bar{K}^0+K^0)/\sqrt{2} = K_1, \\ \mathbf{CP}K_2 = \mathbf{CP}[(K^0-\bar{K}^0)/\sqrt{2}] = (\bar{K}^0-K^0)/\sqrt{2} = -K_2. \end{aligned} \tag{2.1}$$

Because of $\mathbf{CP}(\pi^+\pi^-) = (\pi^+\pi^-)$ for π mesons in a state with the zero angular momentum, the decay into $\pi^+\pi^-$ is allowed for the K_1, but forbidden for the K_2; hence the longer lifetime of K_2 , which was indeed confirmed when the K_2 was discovered.

In 1964, however, Christenson, Cronin, Fitch and Turlay discovered that the long-lived neutral K meson also decays to $\pi^+\pi^-$ with a branching ratio of $\sim 2\times10^{-3}$[2]. Since then the long-lived state was called K_L because it was no longer identical to the CP eigenstate K_2; similarly, the short-lived state was called K_S. The CP violation that manifested itself by the decay $K_L \to \pi^+\pi^-$ was confirmed by subsequent discoveries of the $K_L \to \pi^0\pi^0$[15], and of a charge asymmetry in the decays $K_L \to \pi^\pm e^\mp \nu$[16] and $K_L \to \pi^\pm \mu^\mp \nu$[17].

In spite of all the experimental efforts made so far, however, CP violation was seen in the kaon system only. In the next section, we will describe CP violation in B decays which has the greatest possibilities other than the kaon system today.

2.2 Phenomenology of mixing-induced CP violation in B decays

One of the most promising ways to observe CP violation in B decays is to measure the difference between the time-dependent decay rates of B^0 and $\bar{B}^0$ mesons into a common CP eigenstate. As the mixing between $\bar{B}^0$ and B^0 plays a key role in this mechanism, we call this “mixing-induced” CP violation hereafter. In this section we first explain the phenomenology of time evolution of neutral B mesons. Then we consider the case that both B^0 and $\bar{B}^0$ decay into the same CP eigenstate which as a good place to observe the CP violation.

2.2.1 Time evolution of neutral B mesons

B^0 and $\bar{B}^0$ can mix through second order weak interactions known as the “Box Diagrams”(Figure 2.1). Therefore an arbitrary neutral B meson state is written as the admixture of B^0 and $\bar{B}^0$,

$$|\Phi(t)\rangle = a(t)|B^0\rangle + b(t)|\bar{B}^0\rangle, \tag{2.2}$$

which is governed by the time-dependent Schrödinger equation

$$i\hbar\frac{\partial}{\partial t}|\Phi(t)\rangle = \mathbf{H}|\Phi(t)\rangle. \tag{2.3}$$

The matrix $\mathbf{H}$ is given by

$$\mathbf{H} = \mathbf{M} - \frac{i}{2}\mathbf{\Gamma} = \begin{pmatrix} M_{11} - \frac{i}{2}\Gamma_{11} & M_{12} - \frac{i}{2}\Gamma_{12} \\ M_{21} - \frac{i}{2}\Gamma_{21} & M_{22} - \frac{i}{2}\Gamma_{22} \end{pmatrix}, \tag{2.4}$$

where $\mathbf{M}$ and $\mathbf{\Gamma}$ are Hermitian 2×2 matrices, which are called the mass and decay matrices, respectively. Note that B^0 and $\bar{B}^0$ are flavor eigenstates containing the $\bar{b}$ and b quarks, respectively, and are not the mass eigenstates. The two mass eigenstates, B_H and B_L (H means heavy mass and L means light mass)[1], are given by;

$$\begin{aligned} |B_L\rangle &= p|B^0\rangle + q|\bar{B}^0\rangle, \\ |B_H\rangle &= p|B^0\rangle - q|\bar{B}^0\rangle, \end{aligned} \tag{2.5}$$

where the ratio q/p is expressed as follows assuming the CPT symmetry:[2]

$$\frac{q}{p} = +\sqrt{\frac{M_{12}^* - \frac{i}{2}\Gamma_{12}^*}{M_{12} - \frac{i}{2}\Gamma_{12}}}. \tag{2.6}$$

The time evolution of these states is given by

$$\begin{aligned} |B_L(t)\rangle &= e^{-iM_L t}e^{-\frac{\Gamma_L t}{2}}|B_L(0)\rangle, \\ |B_H(t)\rangle &= e^{-iM_H t}e^{-\frac{\Gamma_H t}{2}}|B_H(0)\rangle, \end{aligned} \tag{2.7}$$

where $M_{L(H)}$ and $\Gamma_{L(H)}$ are the mass and width of the $B_{L(H)}$ state, respectively. The differences in the eigenvalues are expressed with the off-diagonal elements of $\mathbf{M}$ and $\mathbf{\Gamma}$ as follows:

$$\begin{aligned} \Delta m &\equiv M_H - M_L \\ &= -2\mathrm{Re}\left(\frac{q}{p}(M_{12} - \frac{i}{2}\Gamma_{12})\right) \\ \Delta\Gamma &\equiv \Gamma_L - \Gamma_H \\ &= -4\mathrm{Im}\left(\frac{q}{p}(M_{12} - \frac{i}{2}\Gamma_{12})\right) \end{aligned} \tag{2.8}$$

In the B meson system, $\Delta\Gamma$ is much smaller than the average width defined as $\mathit{\Gamma} \equiv (\Gamma_L + \Gamma_H)/2$, because the difference is produced by common decay channels to B^0 and $\bar{B}^0$ with branching ratios of order 10^{-3} or less. Thus the relation $e^{\Delta\Gamma t} = e^{\frac{\Delta\Gamma}{\Gamma}\Gamma t} \simeq 1$ holds.

[1] On the mass difference between the two states within the framework of the Standard Model with the Kobayashi-Maskawa ansatz, see [18].

[2] Here the phase convention is chosen such that the relation $CP|B^0\rangle = |\bar{B}^0\rangle$ holds.

On the other hand the mass difference, Δm, is comparable to Γ and is measured to be $\Delta m/\Gamma \sim 0.73$ [19].

In an actual experiment, a pair of B^0 and $\bar{B}^0$ is produced where each B meson carries a specific quark flavor. Therefore what is practically important is the time evolution of an initially pure B^0 or $\bar{B}^0$ state which is obtained from equations (2.5), (2.7) and (2.8):

$$\begin{aligned} |B^0(t)\rangle &= e^{-iMt}e^{-\frac{1}{2}\Gamma t}\left\{\cos\left(\tfrac{1}{2}\Delta mt\right)|B^0\rangle + i\tfrac{q}{p}\sin\left(\tfrac{1}{2}\Delta mt\right)|\bar{B}^0\rangle\right\}, \\ |\bar{B}^0(t)\rangle &= e^{-iMt}e^{-\frac{1}{2}\Gamma t}\left\{i\tfrac{p}{q}\sin\left(\tfrac{1}{2}\Delta mt\right)|B^0\rangle + \cos\left(\tfrac{1}{2}\Delta mt\right)|\bar{B}^0\rangle\right\}, \end{aligned} \tag{2.9}$$

where M is the average mass defined as $M \equiv (M_L + M_H)/2$.

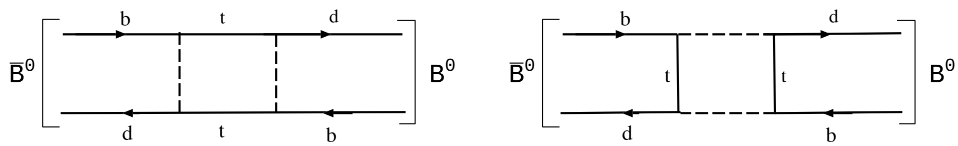

Figure 2.1: *Box diagrams for the $B^0 - \bar{B}^0$ mixing in the Standard Model.*

2.2.2 B meson decay into a CP eigenstate

Now we consider a decay of neutral B mesons into a CP eigenstate f_{CP}. The decay amplitudes of B^0 and $\bar{B}^0$ are expressed by

$$A(f_{CP}) \equiv \langle f_{CP}|H_W|B^0\rangle,\ \bar{A}(f_{CP}) \equiv \langle f_{CP}|H_W|\bar{B}^0\rangle, \tag{2.10}$$

where H_W is the weak-decay Hamiltonian. The key point here is that both B^0 and $\bar{B}^0$ can decay into f_{CP}. For convenience we introduce the ratio of the two amplitudes:

$$\bar{\rho}(f_{CP}) \equiv \frac{\bar{A}(f_{CP})}{A(f_{CP})},\ \rho(f_{CP}) \equiv \frac{A(f_{CP})}{\bar{A}(f_{CP})} = \frac{1}{\bar{\rho}(f_{CP})}. \tag{2.11}$$

From (2.9), (2.10) and (2.11), we can calculate the time-dependent decay rate of initially pure B^0 and $\bar{B}^0$ states:

$$\begin{aligned} \Gamma(B^0(t) \to f_{CP}) &= |\langle f_{CP}|H_W|B^0(t)\rangle|^2 \\ &= e^{-\Gamma t}|A(f_{CP})|^2\left[\frac{1+\cos\Delta mt}{2} + \left|\frac{q}{p}\right|^2 |\bar{\rho}(f_{CP})|^2\frac{1-\cos\Delta mt}{2}\right. \\ &\qquad \left. - \operatorname{Im}\left[\left(\frac{q}{p}\right)\bar{\rho}(f_{CP})\right]\sin\Delta mt\right] \end{aligned} \tag{2.12}$$

$$\begin{aligned} \Gamma(\bar{B}^0(t) \to f_{CP}) &= |\langle f_{CP}|H_W|\bar{B}^0(t)\rangle|^2 \\ &= e^{-\Gamma t}|\bar{A}(f_{CP})|^2\left[\frac{1+\cos\Delta mt}{2} + \left|\frac{p}{q}\right|^2 |\rho(f_{CP})|^2\frac{1-\cos\Delta mt}{2}\right. \\ &\qquad \left. - \operatorname{Im}\left[\left(\frac{p}{q}\right)\rho(f_{CP})\right]\sin\Delta mt\right] \end{aligned} \tag{2.13}$$

As the decay $B^0(t) \to f_{CP}$ is the CP-conjugate process of $\bar{B}^0(t) \to f_{CP}$, the CP invariance is violated if

$$\Gamma(B^0(t) \to f_{CP}) \neq \Gamma(\bar{B}^0(t) \to f_{CP}).$$

For convenience we also introduce the product

$$\lambda_{CP} \equiv \frac{q}{p} \cdot \bar{\rho}(f_{CP}), \tag{2.14}$$

which is independent of phase conventions and thus physically meaningful. Then the time-dependent CP asymmetry is expressed as follows:

$$\begin{aligned} a_{CP}(t) &\equiv \frac{\Gamma(\bar{B}^0(t) \to f_{CP}) - \Gamma(B^0(t) \to f_{CP})}{\Gamma(\bar{B}^0(t) \to f_{CP}) + \Gamma(B^0(t) \to f_{CP})} \\ &= \frac{(|\lambda_{CP}|^2 - 1)\cos \Delta m t + 2\mathrm{Im}(\lambda_{CP}) \cdot \sin \Delta m t}{1 + |\lambda_{CP}|^2}. \end{aligned} \tag{2.15}$$

CP asymmetry arises if $\mathrm{Im}(\lambda_{CP}) \neq 0$, *i.e.* if the phase in $B^0 - \bar{B}^0$ mixing is different from the phase in the decay. In the next section, we will show that this condition is satisfied in the Standard Model and indeed a large CP asymmetry is predicted in a special case.

CP invariance is also violated if $|\lambda_{CP}|^2 \neq 1$. We will explain in the next section that $|q/p| \simeq 1$ holds with good accuracy. Assuming that, the condition $|\lambda_{CP}|^2 \neq 1$ is satisfied only if the sizes of the decay amplitudes, $|A(f_{CP})|$ and $|\bar{A}(f_{CP})|$, are different from each other. As this occurs solely in the decay without a help of $B^0 - \bar{B}^0$ mixing, it is often called direct CP violation. This can be realized if there are more than one Feynman diagrams describing the decay with different weak-decay phases. As shown in the next section, however, decays to important CP eigenstates are described with a single dominant amplitude. Hence the cosine dependence in equation (2.15) vanishes with good accuracy.

When there is only one amplitude (or more than one but with the same weak phase) contributing to the decay to a CP eigenstate, $|\lambda_{CP}| = 1$ holds. As a result, equations (2.12), (2.13) and (2.15) become much simpler:

$$\Gamma(B^0(t) \to f_{CP}) = e^{-\Gamma t}|A(f_{CP})|^2 \left[1 - \mathrm{Im}(\lambda_{CP}) \cdot \sin \Delta m t\right], \tag{2.16}$$

$$\Gamma(\bar{B}^0(t) \to f_{CP}) = e^{-\Gamma t}|A(f_{CP})|^2 \left[1 + \mathrm{Im}(\lambda_{CP}) \cdot \sin \Delta m t\right], \tag{2.17}$$

$$a_{CP}(t) = Im(\lambda_{CP}) \cdot \sin \Delta m t. \tag{2.18}$$

So far we have examined the phenomenological aspects of the mixing-induced CP violation in B decays. In the next section, we describe the CP violation in the Standard Model, explaining that $\mathrm{Im}(\lambda_{CP})$ is directly related to elements of Cabibbo-Kobayashi-Maskawa matrix.

2.3 CP violation in the Standard Model

In this section, we first explain the Cabibbo-Kobayashi-Maskawa matrix and the unitarity triangle. Then we show that the CP violation in $B^0 \to J/\psi K_S$ is proportional to $\sin 2\phi_1$, where ϕ_1 is an angle of the unitarity triangle. After describing the present experimental constraints on the unitarity triangle that imply a rather large value of $\sin 2\phi_1$, we comment on other decay modes usable to measure $\sin 2\phi_1$.

2.3.1 The CKM matrix and the unitarity triangle

In terms of the mass eigenstates, a Lagrangian of charged-current weak interaction forms

$$\mathcal{L}_{int} = -\frac{g}{\sqrt{2}} \left(\bar{u_\mathrm{L}}, \bar{c_\mathrm{L}}, \bar{t_\mathrm{L}}\right) \gamma^\mu V \begin{pmatrix} d_\mathrm{L} \\ s_\mathrm{L} \\ b_\mathrm{L} \end{pmatrix} W_\mu + h.c.. \tag{2.19}$$

The CKM (Cabibbo-Kobayashi-Maskawa) mixing matrix V is a unitary matrix in the flavor space. In the general case of n quark generations, V would be an $n \times n$ matrix. For the case of three generations, V is then, explicitly,

$$V = \begin{pmatrix} V_{11} & V_{12} & V_{13} \\ V_{21} & V_{22} & V_{23} \\ V_{31} & V_{32} & V_{33} \end{pmatrix} = \begin{pmatrix} V_{ud} & V_{us} & V_{ub} \\ V_{cd} & V_{cs} & V_{cb} \\ V_{td} & V_{ts} & V_{tb} \end{pmatrix}, \tag{2.20}$$

which can be parametrized by three Euler angles and six phases, five of which can be removed by adjusting the relative phases of left-handed quark fields. Hence, three angles θ_{ij} and observable phase δ remain in the quark mixing matrix, as was first pointed out by Kobayashi and Maskawa[3]. The imaginary part of the mixing matrix is necessary to describe CP violation in the Standard Model. In general, CP is violated in flavor-changing decays if there is no degeneracy of any two quark masses, and if the quantity $J_{CP} \neq 0$, where

$$J_{CP} = \left| Im(V_{ij} V_{kl} V^*_{il} V^*_{kj}) \right|; i \neq k, j \neq l. \tag{2.21}$$

It can be shown that all the CP-violating amplitudes in the Standard Model are proportional to J_{CP}, and that this quantity is invariant under phase redefinitions of the quark fields[20, 21].

For many applications, it is convenient to use an approximate parametrization of the CKM matrix, called Wolfenstein parametrization[22], which makes explicit the strong hierarchy observed experimentally:

$$V \cong \begin{pmatrix} 1-(\lambda^2/2) & \lambda & A\lambda^3(\rho - i\eta) \\ -\lambda & 1-(\lambda^2/2) & A\lambda^2 \\ A\lambda^3(1-\rho-i\eta) & -A\lambda^2 & 1 \end{pmatrix}. \tag{2.22}$$

Using this parametrization, we obtain

$$J_{CP} \simeq A^2 \eta \lambda^6, \tag{2.23}$$

which shows that J_{CP} is of order 10^{-4} for $\lambda \simeq 0.22$ and $A \simeq 0.8$.

The CKM matrix is unitary. A simple visualization of the implications of unitarity is provided by the so-called unitarity triangle, which uses the fact that the unitarity equation

$$\sum_{i=1}^{3} V_{ij}V_{ik}^{*} = 0 \quad (j \neq k) \tag{2.24}$$

can be represented as the equation of a closed triangle in the complex plane. Most useful from the phenomenological point of view is the triangle relation

$$V_{ud}V_{ub}^{*} + V_{cd}V_{cb}^{*} + V_{td}V_{tb}^{*} = 0, \tag{2.25}$$

since it contains the most poorly-known entries in the CKM matrix. In the parametrization (2.22), $V_{cd}V_{cb}^{*}$ is real, and the unitarity triangle has the form shown in Figure 2.2. It is useful to rescale the triangle by dividing all sides by $|V_{cd}V_{cb}^{*}|$. The rescaled triangle has the coordinates (0,0),(1,0), and ($\bar{\rho}$,$\bar{\eta}$), where

$$\bar{\rho} = \left(1 - \frac{\lambda^2}{2}\right)\rho, \qquad \bar{\eta} = \left(1 - \frac{\lambda^2}{2}\right)\eta \tag{2.26}$$

are related to the Wolfenstein parameters ρ and η appearing in (2.22). CP is violated when the area of the triangle does not vanish, *i.e.* when all the angles are different from zero. The three angles of the triangle are defined as [23]

$$\phi_1 = \pi - \arg\left(\frac{-V_{td}V_{tb}^{*}}{-V_{cb}^{*}V_{cd}}\right), \phi_2 = \arg\left(\frac{V_{tb}^{*}V_{td}}{-V_{ub}^{*}V_{ud}}\right), \phi_3 = \arg\left(\frac{V_{ub}^{*}V_{ud}}{-V_{cb}^{*}V_{cd}}\right). \tag{2.27}$$

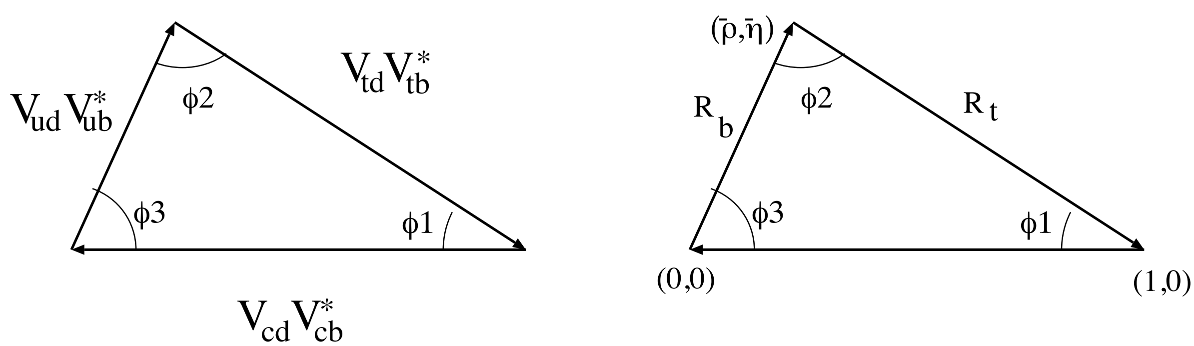

Figure 2.2: *The unitarity triangle of the CKM matrix (left) and its rescaled form in the ($\bar{\rho} - \bar{\eta}$) plane (right).*

2.3.2 CP Asymmetry in $B^0 \to J/\psi K_S$

The combination of relatively large branching fractions, readily accessible final states with small backgrounds and negligible theoretical uncertainty have earned the decay $B^0 \to$

$J/\psi K_S$ the name "gold-plated mode". Among all $B \to$ charmonium + K_S channels, $J/\psi K_S$ is the most effective decay mode experimentally to measure ϕ_1.

As described in the previous section, the size of the mixing-induced CP violation is expressed with the parameter $\mathrm{Im}(\lambda_{J/\psi K_S})$ (where the symbol "CP" is replaced with "$J/\psi K_S$"). The decay $B^0 \to J/\psi K_S$ is based on the quark transition $b \to c\bar{c}s$, for which a single Feynman diagram, called tree diagram shown in the left side of Figure 2.3, is dominant. The contamination from the loop diagram, often called a penguin diagram shown in the right side of Figure 2.3, is extremely small[4]. Furthermore because of the relation $V_{tb}V_{ts}^* = -V_{cb}V_{cs}^* + \mathcal{O}(\lambda^4)$, it follows that up to very small corrections the penguin contributions have the same weak phase as the tree diagram. Therefore it is quite unlikely to exhibit direct CP violation; thus with good accuracy

$$|\bar{A}(J/\psi K_S)| = |A(J/\psi K_S)|, \;\; |\bar{\rho}(J/\psi K_S)| = 1. \tag{2.28}$$

Detailed estimates show that the level of uncertainty is only of order 10^{-3}[24]. Also $\bar{\rho}(J/\psi K_S)$ is expressed with the CKM elements as follows:

$$\bar{\rho}(J/\psi K_S) = \frac{\bar{A}(J/\psi K_S)}{A(J/\psi K_S)} = \frac{V_{cb}V_{cs}^*}{V_{cb}^*V_{cs}}. \tag{2.29}$$

Now we turn to estimate q/p. Within the Standard Model, one can explicitly calculate the ratio Γ_{12}/M_{12}, obtaining $\sim 10^{-2}$[25]. Thus (2.6) becomes

$$\frac{q}{p} \simeq +\sqrt{\frac{M_{12}^*}{M_{12}}} = \frac{V_{tb}^*V_{td}}{V_{tb}V_{td}^*}. \tag{2.30}$$

This also implies $|q/p| \simeq 1$. This combination of CKM parameters can be read off directly from the vertices of the box diagram in Figure 2.1, which in the Standard Model are responsible for the non-diagonal element M_{12} of the mass matrix. Notice that for the real part of the box diagrams, which determines M_{12}, the contributions of c and u quarks in the loops can be neglected.

Some care is required before we obtain the final expression of $\mathrm{Im}(\lambda_{J/\psi K_S})$. First of all, we need to take into account the phase from the $K^0 - \bar{K}^0$ mixing amplitude because of the K_S in the final state. The additional factor is

$$\left(\frac{q}{p}\right)_K \equiv \frac{V_{cs}V_{cd}^*}{V_{cs}^*V_{cd}}. \tag{2.31}$$

Also there is an extra minus sign due to $J/\psi K_S$ being a CP odd state. Thus from (2.29), (2.30) and (2.31), one finally finds

$$\lambda_{J/\psi K_S} = -\left(\frac{q}{p}\right)\cdot\left(\frac{q}{p}\right)_K \cdot \frac{\bar{A}(J/\psi K_S)}{A(J/\psi K_S)} \simeq -\frac{V_{tb}^*V_{td}}{V_{tb}V_{td}^*}\cdot\frac{V_{cs}V_{cd}^*}{V_{cs}^*V_{cd}}\cdot\frac{V_{cb}V_{cs}^*}{V_{cb}^*V_{cs}} = -e^{-2i\phi_1}, \tag{2.32}$$

Therefore we readily obtain

$$\mathrm{Im}\lambda_{J/\psi K_S} \simeq \sin 2\phi_1. \tag{2.33}$$

Hence a measurement of mixing-induced CP violation in $B^0 \to J/\psi K_S$ is a direct measurement of $\sin 2\phi_1$ which constrains the unitarity triangle.

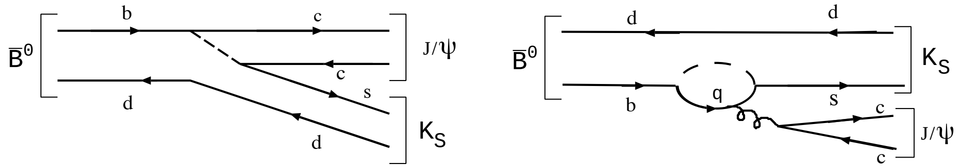

Figure 2.3: *Tree (left) and penguin (right) diagrams for the decay $B \to J/\psi K_S$.*

2.3.3 Constraints on the unitarity triangle and $\sin 2\phi_1$

In this section we review the present experimental constraints on the unitarity triangle, which allow us to derive a constraint on $\sin 2\phi_1$.

The entries in the first two rows of the CKM matrix are accessible in so-called direct (tree-level) processes, *i.e.* in weak decays of hadrons containing the corresponding quarks. In practice, $|V_{ud}|$ and $|V_{us}|$ are known to an accuracy of better than 1%, $|V_{cb}|$ is known to 5%, and $|V_{cd}|$ and $|V_{cs}|$ are known to about 10∼20%. Hence, the two Wolfenstein parameters λ and A are rather well determined experimentally:

$$\lambda = |V_{us}| = 0.2205 \pm 0.0018, \qquad A = \left|\frac{V_{cb}}{V_{us}^2}\right| = 0.80 \pm 0.04. \tag{2.34}$$

On the other hand, $|V_{ub}|$ has an uncertainty of about 30%, and the same is true for $|V_{td}|$, which is obtained from $B^0 - \bar{B}^0$ mixing. This implies a rather significant uncertainty in the values of the Wolfenstein parameters ρ and η. A more precise determination of these parameters will be a challenge to experiments and theory over the next decade.

To determine the shape of the triangle, one can aim for measurements of the two sides R_b and R_t, and three angles ϕ_1, ϕ_2, and ϕ_3 (Figure 2.2). So far, experimental information is available only on the sides of the triangle.

R_b or $\left|\frac{V_{ub}}{V_{cb}}\right|$ can be extracted from semileptonic B decays,

$$R_b = \sqrt{\bar{\rho}^2 + \bar{\eta}^2} = \left(1 - \frac{\lambda^2}{2}\right)\frac{1}{\lambda}\left|\frac{V_{ub}}{V_{cb}}\right|. \tag{2.35}$$

To determine R_t , one needs information on $|V_{td}|$:

$$R_t = \sqrt{(1-\bar{\rho}^2) + \bar{\eta}^2} = \frac{1}{\lambda}\left|\frac{V_{td}}{V_{cb}}\right|. \tag{2.36}$$

We are able to extract this value from the measurement of $B^0 - \bar{B}^0$ mixing. In the Standard Model, the mass difference Δm between the two neutral B meson states is calculable from the box diagrams shown in Figure 2.1. The theoretical expression is

$$\Delta m_{B_d} = \frac{G_F^2 m_W^2}{6\pi^2}\eta_B B_{B_d} f_{B_d}^2 m_{B_d} S(m_t/m_W)|V_{td}V_{tb}^*|^2, \tag{2.37}$$

where η_{B_d} accounts for the QCD corrections[26], and $S(m_t/m_W)$ is a function of the top quark mass[27]. The product $B_{B_d} f_{B_d}^2$ parameterizes the hadronic matrix element of a local four-quark operator between B_d-meson states. $\sqrt{B_{B_d}} f_{B_d}$ has a theoretical uncertainty of about 20% from systematic errors in the lattice QCD calculation[28, 29, 30]. Another way of improving the determination of R_t is through a measurement of $B_s^0 - \bar{B}_s^0$ mixing,

$$R_t^2 = \left(\frac{f_{B_s}\sqrt{B_{B_s}}}{f_{B_d}\sqrt{B_{B_d}}} \right)^2 \frac{m_{B_s}}{m_{B_d}} \frac{\Delta m_{B_d}}{\Delta m_{B_s}} \frac{1-\lambda^2(1-2\bar{\rho})}{\lambda^2} \tag{2.38}$$

The advantage of this determination over the one from Δm_{B_d} alone is that the dependence on m_t and $|V_{cb}|$ has been eliminated and that the ratio f_{B_s}/f_{B_d} can be more precisely determined than each decay constant itself. Presently only a lower limit on Δm_{B_s} has been obtained. Thus Δm_{B_s} value gives us an upper limit on R_t.

Equations (2.35) and (2.36) yield constraints on the Wolfenstein parameters $\bar{\rho}$ and $\bar{\eta}$, which have the form of rings centered at $(\bar{\rho}, \bar{\eta}) = (0,0)$ and (0,1). Another constraint can be obtained from the measurement of indirect CP violation in the kaon system. The experimental result on the parameter ϵ_K measuring CP violation in $K^0 - \bar{K}^0$ mixing implies that the unitarity triangle lies in the upper half plane. The constraint arising in the $\bar{\rho} - \bar{\eta}$ plane has the form of a hyperbola, the shape of which depends on a hadronic parameter B_K[31].

Figure 2.4 shows experimental constraints on the unitarity triangle in the $\bar{\rho} - \bar{\eta}$ plane[32]. In Figure 2.4, we show the constraints which the measurements of R_b, R_t,

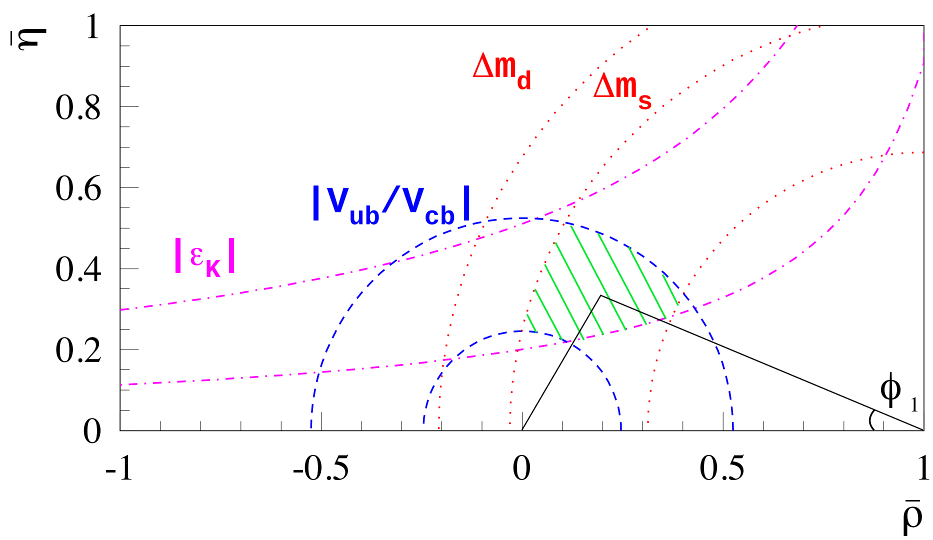

Figure 2.4: *Experimental constraints on the unitarity triangle in the $\bar{\rho} - \bar{\eta}$ plane. The region between the dashed (dotted) circles is allowed by the measurement of R_b (R_t) discussed in the text. The dot-dashed curves show the constraint from the measurement of the ε_k parameter in the kaon system. Each constraint shows the region with the confidence level of 95%. An example of allowed unitarity triangle is also shown.*

and ϵ_K imply in the $\bar{\rho} - \bar{\eta}$ plane. Given the present theoretical and experimental uncertainties in the analysis of charmless B-decays, $B^0 - \bar{B}^0$ mixing, and CP violation in the kaon system, there is still a rather large region allowed for the Wolfenstein parameters. The allowed region for $\sin 2\phi_1$ obtained from Figure 2.4 is

$$0.50 < \sin 2\phi_1 < 0.85$$

at the 95% C.L. Thus large mixing-induced CP violation is expected. There also exist other estimations by several groups with different sizes of the error,[33, 34, 35] but the central values more or less agree.

2.3.4 Comments on the other decay modes

All processes, which have quark transition of $b \to c\bar{c}s$, follow the same line described in previous sections, except the CP eigenvalue of the final states. In order to minimize the statistical error, one needs to include similar decay modes as many as possible. Table 2.1 shows observed branching ratios for $B^0(B^\pm) \to$ charmonium + $K(K^*)$. The decay

Table 2.1: *Branching ratios of* $B \to$ Charmonium $+ K(K^*)$

Decay mode	Experimental Branching Ratio[19]
$J/\psi \bar{K}^0$	$(8.9 \pm 1.2) \times 10^{-4}$
$J/\psi K^-$	$(10.0 \pm 1.0) \times 10^{-4}$
$J/\psi \bar{K}^{*0}$	$(1.50 \pm 0.17) \times 10^{-3}$
$J/\psi K^{*-}$	$(1.48 \pm 0.27) \times 10^{-3}$
$\psi(2S)\bar{K}^0$	$\leq 8 \times 10^{-4}$
$\psi(2S)K^-$	$(5.8 \pm 1.0) \times 10^{-4}$
$\psi(2S)\bar{K}^{*0}$	$(9.3 \pm 2.3) \times 10^{-4}$
$\psi(2S)K^{*-}$	$\leq 3 \times 10^{-3}$
$\chi_{c1}\bar{K}^0$	$\leq 2.7 \times 10^{-3}$
$\chi_{c1}\bar{K}^-$	$(1.0 \pm 0.4) \times 10^{-3}$
$\chi_{c1}\bar{K}^*$	$\leq 2.1 \times 10^{-3}$
$\chi_{c1}\bar{K}^{*-}$	$\leq 2.1 \times 10^{-3}$

modes $B^0(\bar{B}^0) \to \psi(2S)K_S$ and $B^0(\bar{B}^0) \to \chi_{c1}K_S$ are promising. Although the branching fraction has not been established yet, the accompanying charged modes show the similar branching fractions to that of $J/\psi K^-$. Assuming isospin symmetry, one can also expect a similar situation in the decays of neutral B mesons. Another experimental advantage is that these decays have a decay topology similar to $J/\psi K_S$. The vertex resolution is also expected to be almost identical as the final states include J/ψ in all cases. Thus we will include these decay modes in this study.

The decay modes $J/\psi \bar{K}^{*0}$ and $\psi(2S)\bar{K}^{*0}$ have the large branching fractions. However these are mixtures of CP-even and CP-odd states because the final state consists of two vector particles. In order to disentangle one from the other, we need to investigate the angular distributions of decay particles which are rather complicated. Therefore we will not include them.

So far we have concentrated on the final states including K_S. The other interesting option is to use K_L in the final state, namely $J/\psi K_L$. As the event topology is quite different in this case, the analysis method is also rather different. Hence it is not included in this study.

2.4 Mixing-induced CP violation at an asymmetric B-factory

In the KEK B-factory experiment, the B meson pair in $\Upsilon(4S) \to B^0\bar{B}^0$ is produced into a **C** odd configuration with the two mesons flying apart from each other at time of production $t = 0$. Subsequently oscillations between B^0 and $\bar{B}^0$ start that are highly correlated for **C** = -1. Bose statistics tells us that if one of the mesons is a B^0 at some time t, the other one cannot be a B^0 as well at the same time, since the state must be odd under exchange of the two mesons. The time evolution of the pair is then given by

$$|(B^0\bar{B}^0)_{\mathbf{C}=-}(t)\rangle = e^{-\Gamma t}\frac{1}{\sqrt{2}}\left[|B^0(\vec{k})\bar{B}^0(-\vec{k})\rangle - |B^0(-\vec{k})\bar{B}^0(\vec{k})\rangle\right], \tag{2.39}$$

where $\vec{k}$ and $-\vec{k}$ are momenta of B mesons in the $\Upsilon(4S)$ rest frame. Once one of the B has decayed, this coherence is lost, and the remaining $\bar{B}$ will oscillate without the production constraint.

If one B decays to a CP eigenmode, $B \to$ charmonium $+ K_S$ in our case, and the other decays to a state that can come from either B^0 or $\bar{B}^0$, but not both[3], the event can be used to examine the time dependence of CP asymmetry (Figure 2.5).

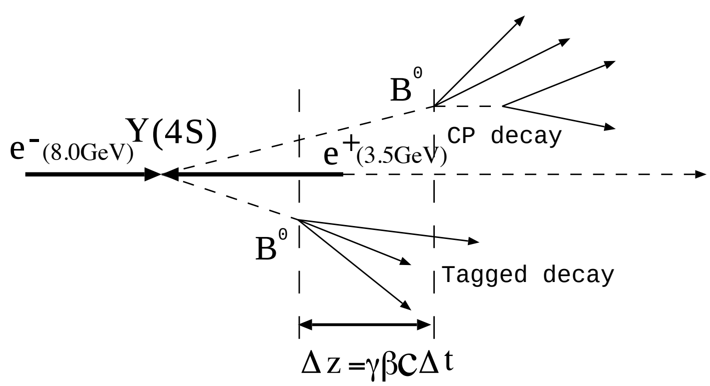

Figure 2.5: *Decay scheme of the $B^0\bar{B}^0$ system at the asymmetric B factory. The proper time is measured from the distance of two B decays.*

[3]Such a state is called "flavor-specific" hereafter.

CP asymmetry appears in difference of the decay rates between B^0 and $\bar{B}^0$. When one B decays to a CP eigenmode and the other decays to a flavor-specific mode, the decay rates are expressed as

$$\begin{aligned}\Gamma(f(t_1), B^0(t_2)) &= e^{-\Gamma_B(t_1+t_2)}(1 + \sin 2\phi_1 \cdot \sin \Delta m(t_1 - t_2)) \\ \Gamma(f(t_1), \bar{B}^0(t_2)) &= e^{-\Gamma_B(t_1+t_2)}(1 - \sin 2\phi_1 \cdot \sin \Delta m(t_1 - t_2)).\end{aligned}$$

where f is defined as a certain CP eigenstate. Integrating this equation over $(t_1 + t_2)$ to $(t_1 - t_2)(\equiv \Delta t)$, the proper time distribution becomes the same form as (2.16) and (2.17).

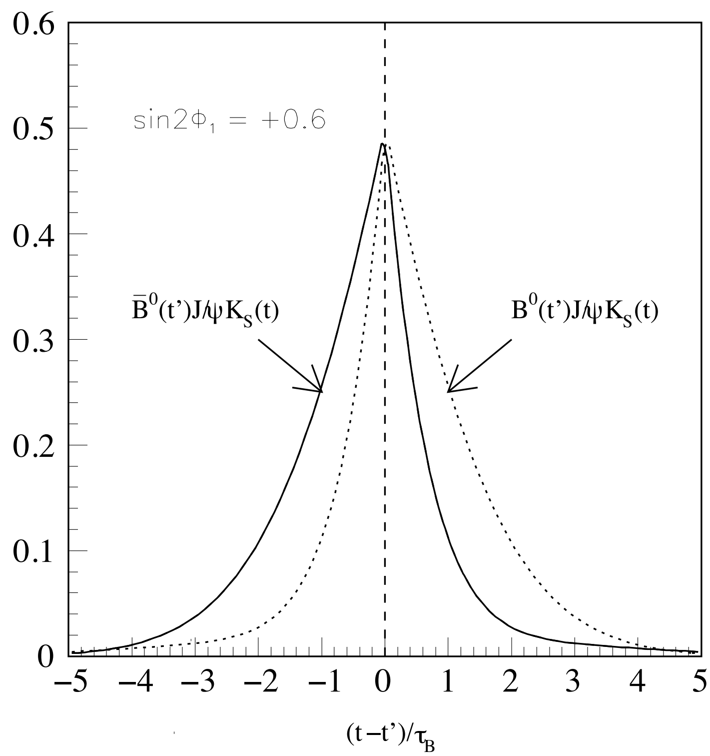

Figure 2.6: *Proper time distribution for $B^0(\bar{B}^0) \to J/\psi K_S$.*

Figure 2.6 shows the proper time distribution for $B^0 \to J/\psi K_S$ decays for the case of $\sin 2\phi_1 = +0.6$ as a function of the time distribution in the unit of the B lifetime, τ_B. The solid and dotted lines are the decay rates of the $\bar{B}^0$ and B^0, respectively. The difference between the positive and negative time scale reflects the CP asymmetry. This can be seen either in the solid and dotted curves separately, or in the sum after the time scale of the dotted curve is reversed.

The proper time of B decay is measured with the distance of vertices of two B mesons as

$$\Delta t \simeq \Delta z / c\beta\gamma, \tag{2.40}$$

where $\beta\gamma$ is the Lorentz boost factor due to the asymmetric beam energy ($\beta\gamma = 0.425$ at KEKB) and Δz is the distance between the decay vertices of the two B mesons along the beam direction. Figure 2.5 shows the measurement scheme of proper time of B mesons.

One of the key issues in an experimental point of view is to find flavor-specific decays efficiently. This process is called “flavor tagging”.

The following informations are useful to tag the flavor of the B meson:

- The charge of leptons from semi-leptonic decay of B meson.,
- the charge of kaons which signatures a cascade decay $b \to c \to s$,
- the charge of slow pions from $B \to D^{*\pm}X, D^{*\pm} \to D^0\pi^{\pm}$.

As shown in Figure 2.7, the lepton’s charge from the b-quark ($\bar{b}$-quark) that decays into $c\mathrm{W}^-$ ($\bar{c}\mathrm{W}^+$) indicates the flavor of the B meson. Also as shown in Figure 2.8, the flavor of the B meson has correlation with the charge of the kaon in the final state. Yet another method is to tag pions in the decay $D^{*\pm} \to \pi^{\pm}D^0$, because about 1/4 of B mesons decay into states with D^*. The detail of the methods of the flavor tagging in this study is described in Section 4.6.

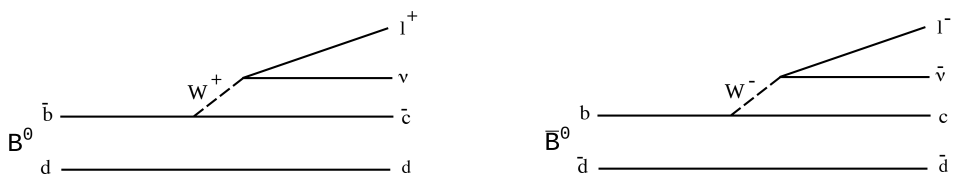

Figure 2.7: *Diagrams for flavor tagging with leptons.*

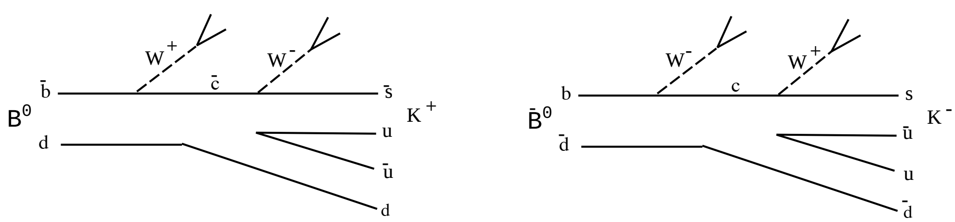

Figure 2.8: *Diagrams for flavor tagging with charged kaons.*

2.5 Previous experimental results

The first direct measurement of $\sin 2\phi_1$ was performed by the OPAL collaboration with $B^0 \to J/\psi K_S$ at the energy of the Z^0 peak. They have measured $\sin 2\phi_1$ with 24 $J/\psi K_S$ events including background. The result was[36]

$$\mathrm{OPAL} \quad : \qquad \sin 2\phi_1 = 3.2^{+1.8}_{-2.0}(stat.) \pm 0.5(syst.).$$

The CDF collaboration measured with 395 ± 31 $B^0 \to J/\psi K_S$ events in $p\bar{p}$ collisions at $\sqrt{s} = 1.8$ TeV. The result was [37]

$$\text{CDF} \quad : \qquad \sin 2\phi_1 = 0.79^{+0.41}_{-0.44}(stat. + syst.).$$

The ALEPH collaboration also measured with 23 candidates. The preliminary result was [38]

$$\text{ALEPH} \quad : \qquad \sin 2\phi_1 = 0.84^{+0.82}_{-1.04}(stat.) \pm 0.16(syst.)$$

Belle and BaBar recently reported the following preliminary results with $6.2 fb^{-1}$ sample and $9.0 fb^{-1}$ sample respectively [39, 32]:

$$\begin{aligned} \text{Belle} \quad &: \qquad \sin 2\phi_1 = 0.45^{+0.43}_{-0.44}(stat)^{+0.07}_{-0.09}(syst) \\ \text{BaBar} \quad &: \qquad \sin 2\phi_1 = 0.12 \pm 0.37(stat) \pm 0.09(syst), \end{aligned}$$

where the result from Belle is based on $B^0 \to J/\psi K_L,\ J/\psi\pi^0,\ J/\psi K_S(\to \pi^0\pi^0)$, as well as the modes covered in this thesis which had the dominant contribution.

Chapter 3

Experimental apparatus and software

In this chapter, we describe the KEK B-factory and its apparatus, the Belle detector and the KEKB accelerator, for the CP violation measurement at the neutral B system.

The KEKB accelerator is designed to produce a large number of B mesons like a factory. The Belle detector is optimized to detect particles from B meson decays efficiently. These are built at KEK (High Energy Accelerator Research Organization). The experiment was started in June, 1999. In Section 3.1, a brief introduction of the KEKB accelerator is given. In Section 3.2, an overview of the Belle detector follows. In Section 3.3, the software used in this study is described.

3.1 KEKB accelerator

The KEKB is an asymmetric e^+e^- collider. The energy of electrons and positrons are 8 GeV and 3.5 GeV, respectively. Hence the center-of-mass energy is 10.58 GeV, where the $\Upsilon(4S)$ resonance resides, and the Lorentz boost parameter $\beta\gamma$ is 0.425. Electrons have higher energy than positrons in order to avoid ion trapping, which happens only at low energies. The KEKB consists of two rings as illustrated in Figure 3.1. The electron ring is called HER (High Energy Ring) and the positron ring is called LER (Low Energy Ring). These rings are located side by side in the existing TRISTAN tunnel with the circumference of about 3 km. A single interaction point (IP) is located in the Tsukuba experimental hall.("Tsukuba Area")

Electrons (positrons) can be directly injected from the LINAC to the HER (LER) at Fuji area and circulate clockwise (anti-clockwise). At the KEKB, electron and positron beams collide at a finite angle of ± 11 mrad, in order to avoid parasitic collisions near the IP. To achieve the design luminosity of $10^{34}\, cm^{-2}s^{-1}$ which corresponds to 10^8 $\Upsilon(4S)$ a year, 5000 bunches need to be injected in each ring, where the bunch interval is only 2 ns (or 60cm). As of July 2000, the achieved luminosity is $2 \times 10^{33}\, cm^{-2}s^{-1}$ with 1146 bunches and the spacing between them of 240 cm. The achieved beam currents are 465 mA for the LER and 420 mA for the HER. Main parameters of the KEKB are summarized in Table 3.1.

The detailed description for KEKB is given in [40].

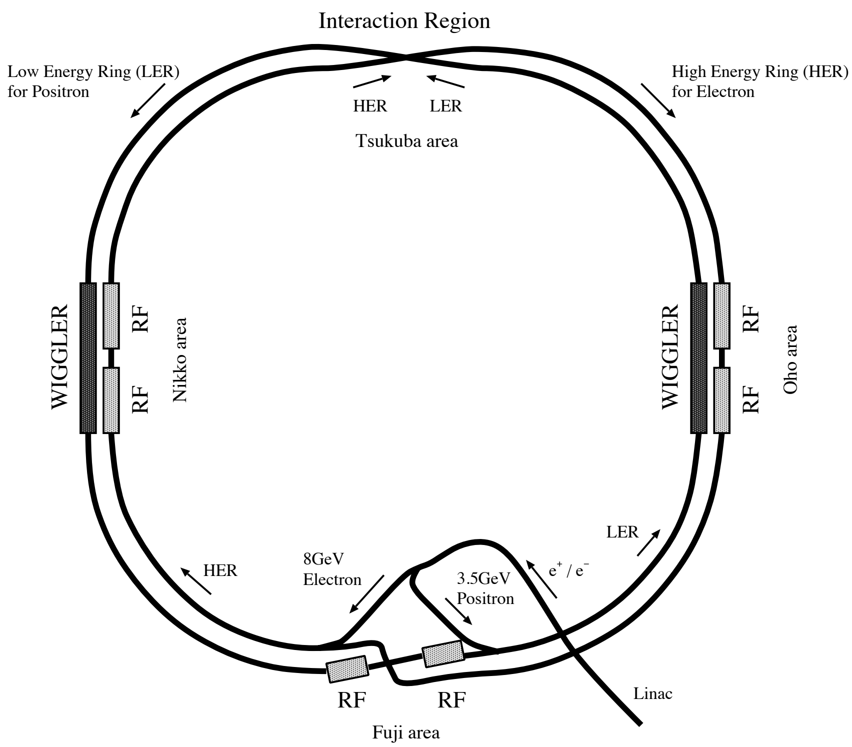

Figure 3.1: *Configuration of the KEKB accelerator*

3.2 Belle Detector

The configuration of the Belle detector is shown in Figure 3.2 and Figure 3.3.

Because of the asymmetry of the beam energy, the detector itself also has the asymmetry: *i.e.* it has a larger acceptance in the direction of electrons (which is defined as "the forward region"). B meson decay vertices are measured by a silicon strip detector (SVD) just outside a beryllium beam pipe. Charged particles are reconstructed by the central drift chamber (CDC). Particle identification is provided by dE/dx measurements in the CDC, the Aerogel Čerenkov counter (ACC) and the time of flight (TOF) counter arrays outside the CDC. Electromagnetic showers are detected in the CsI(Tl) electromagnetic calorimeter (ECL) located inside the superconducting solenoid, which provides magnetic field of 1.5 Tesla. K_L mesons and muon counters (KLM), which consist of resistive plate counters (RPCs), are interspersed in the iron return yoke of the magnet.

The performance of each detector is summarized in Table 3.2. The details of each detector component except SVD is described in [41]. A brief description of these components follows.

Table 3.1: *Main parameters of KEKB.*

Ring		LER	HER	
Energy	E	3.5	8.0	GeV
Circumference	C	3016.26		m
Luminosity	$\mathcal{L}$	1×10^{34}		$\mathrm{cm}^{-2}\mathrm{s}^{-1}$
Crossing angle	θ_x	± 11		mrad
Tune shifts	ξ_x/ξ_y	0.039/0.052		
Beta function at IP	β_x^*/β_y^*	0.33/0.01		m
Beam current	I	2.6	1.1	A
Natural bunch length	σ_z	0.4		cm
Energy spread	σ_ε	7.1×10^{-4}	6.7×10^{-4}	
Bunch spacing	s_b	0.59		m
Particle/bunch	N	3.3×10^{10}	1.4×10^{10}	
Emittance	$\varepsilon_x/\varepsilon_y$	$1.8 \times 10^{-8}/3.6 \times 10^{-10}$		m
Synchrotron tune	ν_s	$0.01 \sim 0.02$		
Betatron tune	ν_x/ν_y	45.52/45.08	47.52/43.08	
Momentum compaction factor	α_p	$1 \times 10^{-4} \sim 2 \times 10^{-4}$		
Energy loss/turn	U_o	0.81†/1.5‡	3.5	MeV
RF voltage	V_c	$5 \sim 10$	$10 \sim 20$	MV
RF frequency	f_{RF}	508.887		MHz
Harmonic number	h	5120		
Longitudinal damping time	τ_ε	43†/23‡	23	ms
Total beam power	P_b	2.7†/4.5‡	4.0	MW
Radiation power	P_{SR}	2.1†/4.0‡	3.8	MW
HOM power	P_{HOM}	0.57	0.15	MW
Bending radius	ρ	16.3	104.5	m
Length of bending magnet	ℓ_B	0.915	5.86	m

†: without wigglers, ‡: with wigglers

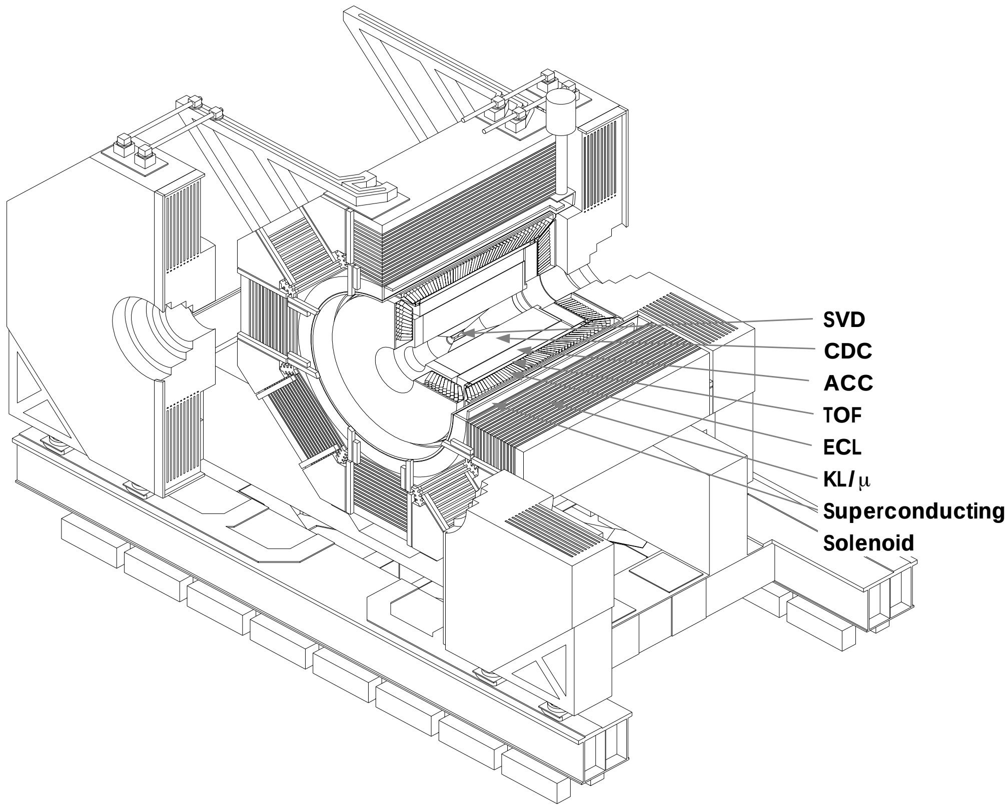

Figure 3.2: *Belle detector*

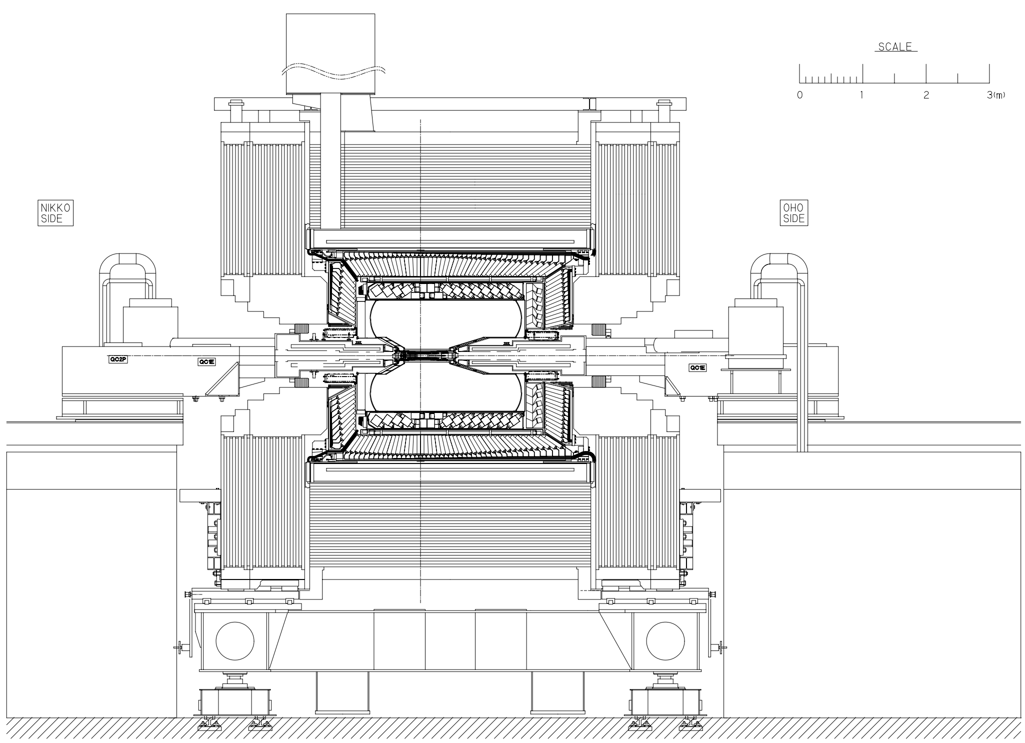

Figure 3.3: *Side view of the Belle detector*

3.2.1 Silicon Vertex Detector (SVD)

It is crucially important to measure the flight length in the z direction of the produced two B mesons in studying the CP violation. The Silicon Vertex Detector (SVD) provides information necessary for the reconstruction of decay vertices close to the IP. Therefore the SVD is one of the most important detectors in the mixing-induced CP analysis.

The configuration of the the SVD is shown in Figure 3.4. The SVD has three cylindrical detection layers consisting of 8, 10 and 14 units of Double-sided Silicon Strip Detectors (DSSDs) with $300\mu m$ thickness. The position of each sensor is 3.0cm, 4.55cm, and 6.05cm in the radial direction, respectively. The polar angle coverage is from 23° to 140°. The number of readout channels is 81920. The impact parameter[1] resolution at the IP is $(19 + 50/p\beta \sin^{3/2}\theta)\mu m$ in r-ϕ and $(36 + 42/p\beta \sin^{5/2}\theta)\mu m$ in z direction, as shown in Figure 3.5.

The details of SVD are described in [42].

3.2.2 Central Drift Chamber (CDC)

The role of the Central Drift Chamber (CDC) is to measure the momentum and dE/dx of charged particles used for the particle identification.

The configuration of the the CDC is shown in Figure 3.6. The inner and outer radii of CDC are 8 cm and 88cm, respectively. The CDC is a small-cell drift chamber containing a total of 50 sense wire layers (32 axial wire layers and 18 stereo wire layers) and 3 cathode strip layers. The sense-wire layers are grouped into 11 super layers. Stereo angles range from 42.5 mrad to 72.1 mrad. The number of readout channels is 8,400 for anode wires and 1,792 for cathode strips. A 50% helium-50% ethane gas mixture is used in the chamber to minimize the multiple Coulomb scattering contribution to the momentum resolution.

The position resolution is estimated to be $\sigma_{r\phi} = 130\mu m$. The transverse momentum resolution σ_t/p_t is $(0.20p_t \oplus 0.29)$% where p_t is the transverse momentum in GeV/c (Figure 3.7). The dE/dx resolution is $\sigma_{dE/dx} = 7.8\%$ and 6% for minimum ionizing pions from K_S^0 decay and for Bhabha and μ-pair events, respectively (Figure 3.8). The details of the CDC are described elsewhere [43].

3.2.3 Aerogel Čherenkov Counter (ACC)

The ACC is mainly used for separation of kaons and pions in the high momentum range ($1.2 < p < 3.5\,\mathrm{GeV}/c$). The ACC consists of blocks of silica aerogel in 0.2mm-thick aluminum boxes. This material is a colloidal form of glass, in solid form, transparent and very light.

The barrel part consists of 960 aerogel counters segmented into 16 division in z and 60 in ϕ. Counters with five different refractive indices, namely, $n = 1.010$, 1.013, 1.015, 1.020 and 1.028 are used depending on the polar angle. The Čerenkov light from each barrel counter is fed into two fine-mesh photomultipliers (FMPMTs) attached to the aerogel

[1] An impact parameter is defined as the distance between a position at the closest approach to one point and the point.

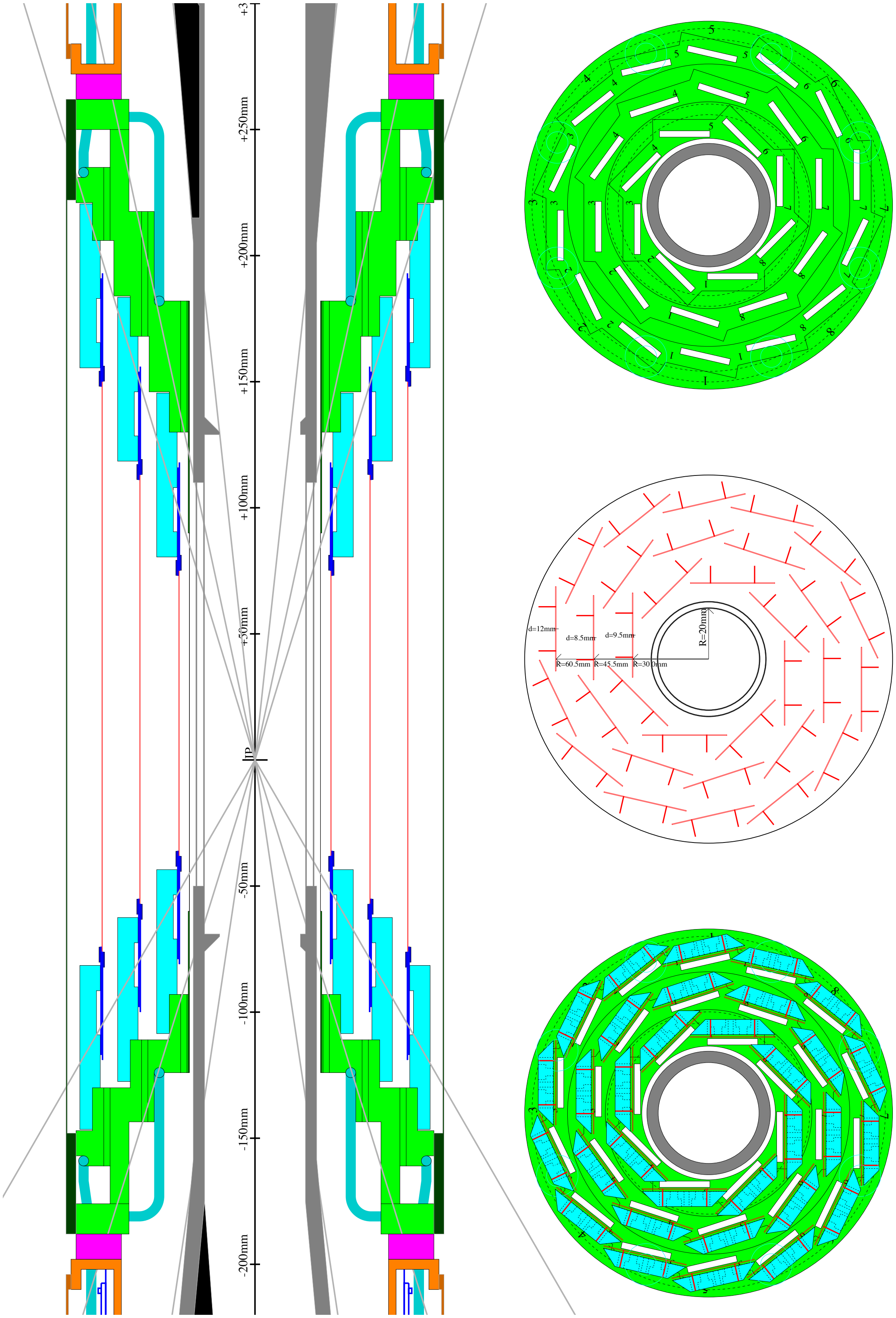

Figure 3.4: *SVD : side*

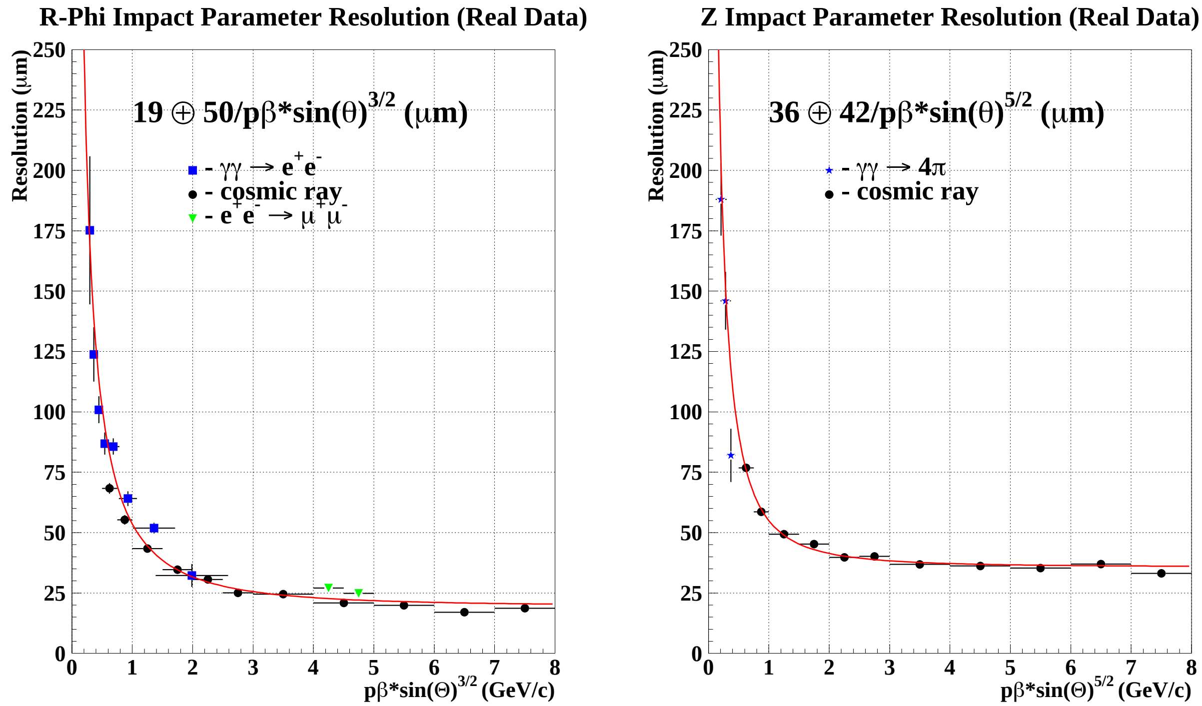

Figure 3.5: *The impact parameter resolutions at the IP. Left figure shows this resolution in the r-ϕ plane and right figure shows that in the Z plane.*

radiator modules. FMPMTs can work within the 1.5 T magnetic field. Forward endcap has a total of 224 counters with $n = 1.03$ and is structured in five concentric rings with 60-, 48-, 48-, 36- and 36-fold segmentations. Each endcap counter is connected to one FMPMT. The number of readout channels is 1,560 in the barrel and 228 in the endcap. The configurations of barrel and endcap aerogel Čerenkov counter are shown in Figure 3.9 and Figure 3.10.

3.2.4 Time of Flight counter (TOF)

The TOF is used to distinguish kaons from pions up to 1.2 GeV/c. The Trigger Scintillation Counter (TSC) also generates timing signal for trigger. They measure the elapsed time between a collision at the IP and the time which the particle hits the TOF layer. With the particle momentum measured by the CDC, this time difference gives an identification of the particle mass.

One 5 mm-thick TSC layer and one 4 cm-thick Time-of-Flight counter (TOF) layer are placed at the position of 120 cm in radius from the IP with a 2 cm gap. TOF is segmented into 128 in ϕ sectors and each counter is read out by one FMPMT at each end. TSC's have a 64-fold segmentation and are read out only from the backward end by a single FMPMT. The total number of readout channels is 256 for TOF and 64 for TSC. The time resolution is $\sigma_t = 100$ ps. The TOF hit efficiency is found to be 95% for single-end

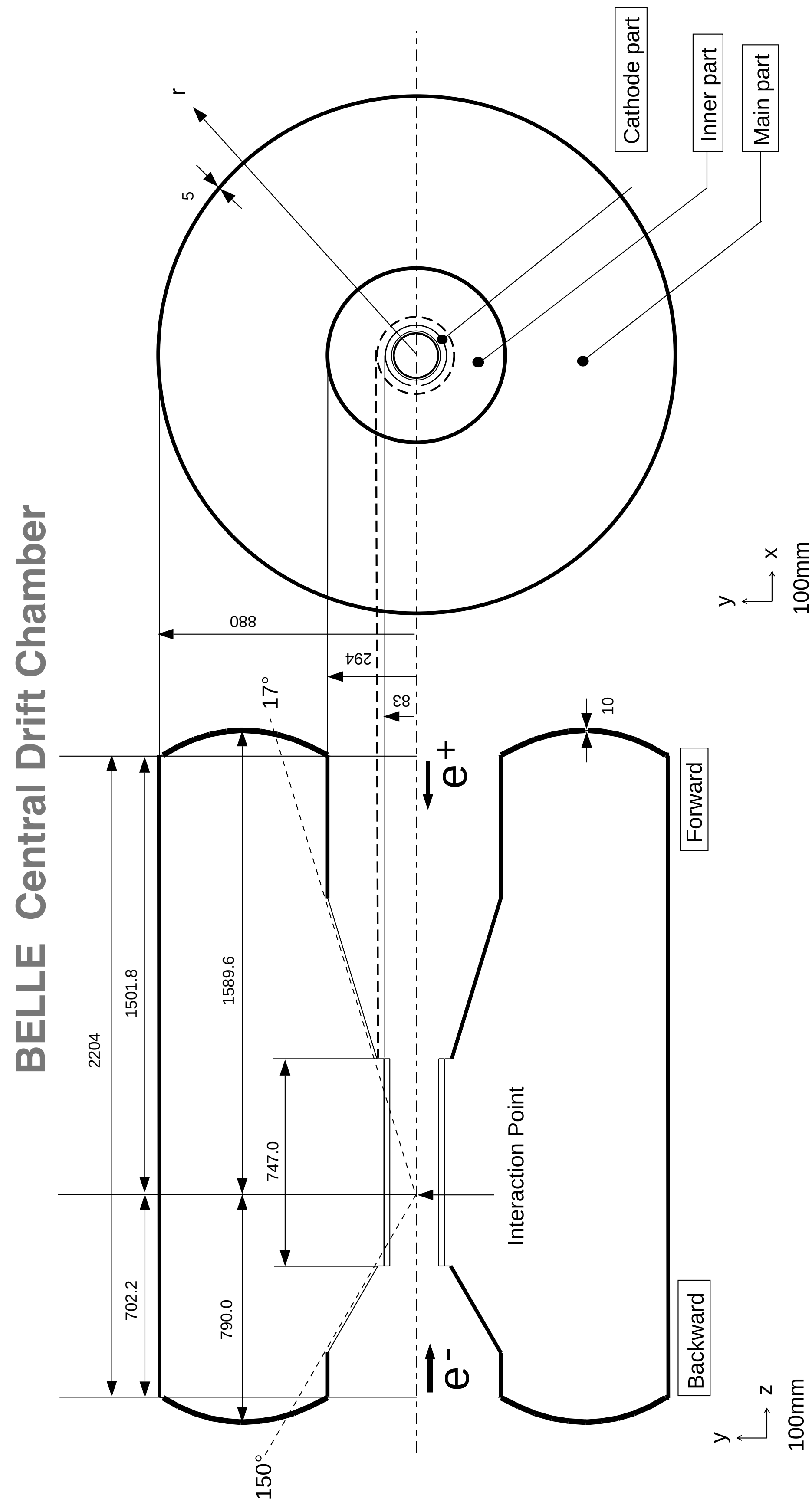

Figure 3.6: *The Central drift chamber*

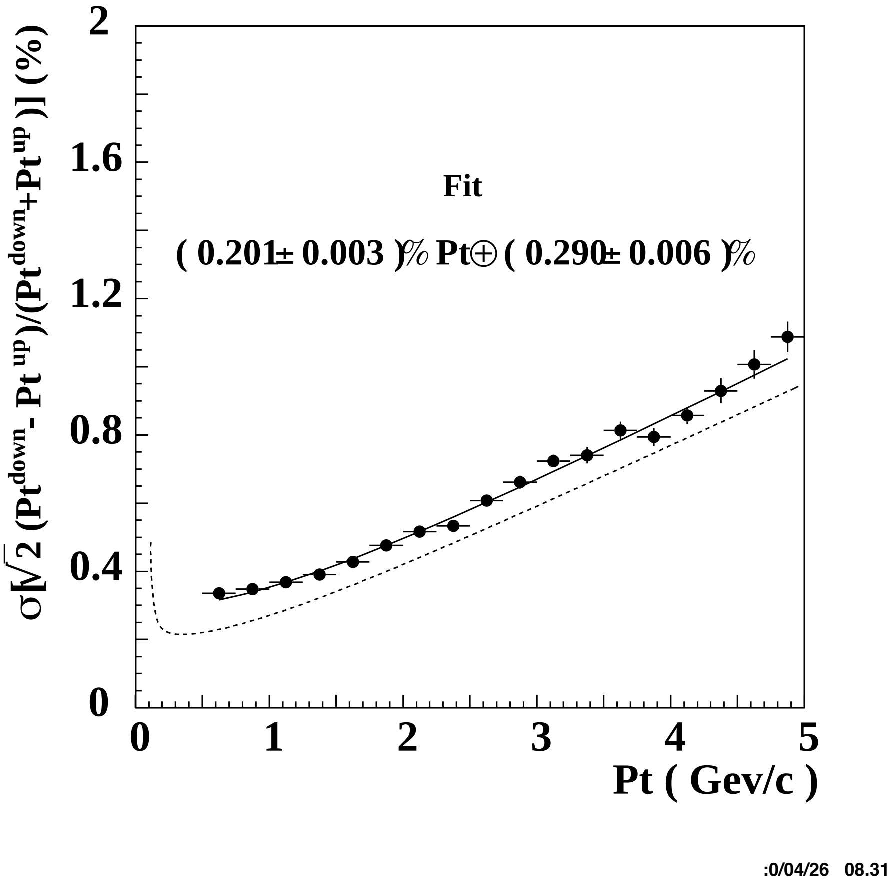

Figure 3.7: *The transverse momentum resolution σ_t/p_t of the CDC*

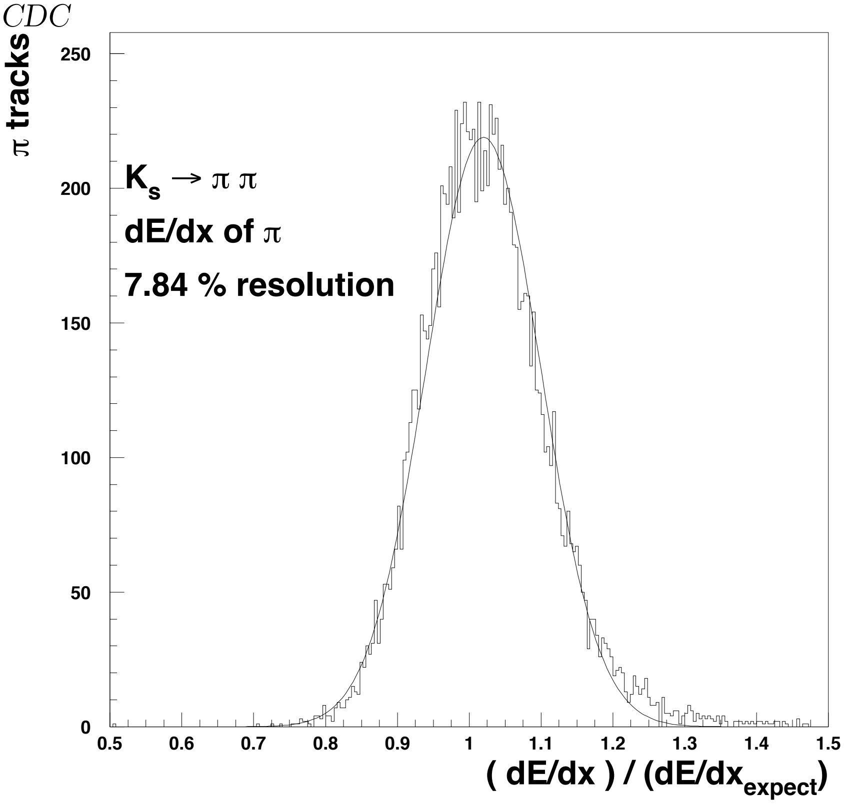

Figure 3.8: *Distribution of $\langle dE/dx\rangle / \langle dE/dx\rangle_{exp}$ for pions from K_S^0 decay*

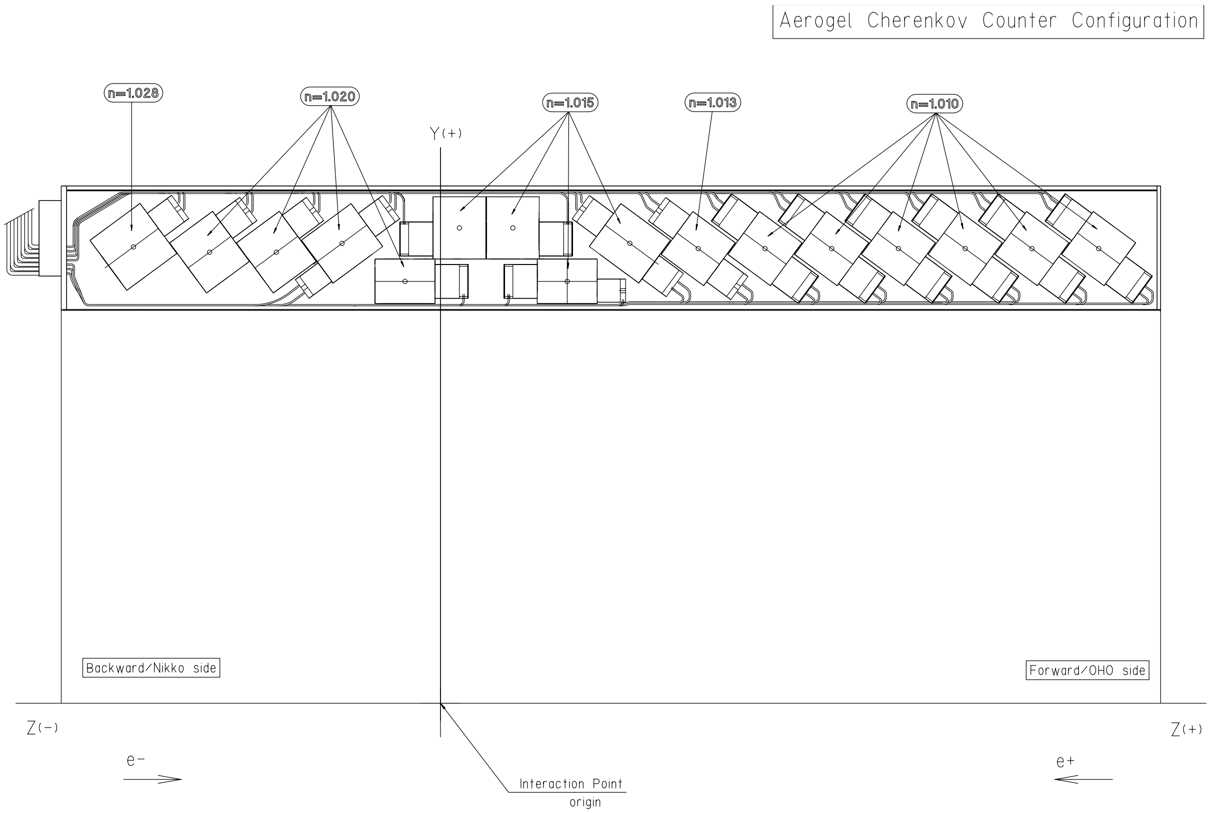

Figure 3.9: *Barrel aerogel Čerenkov counter*

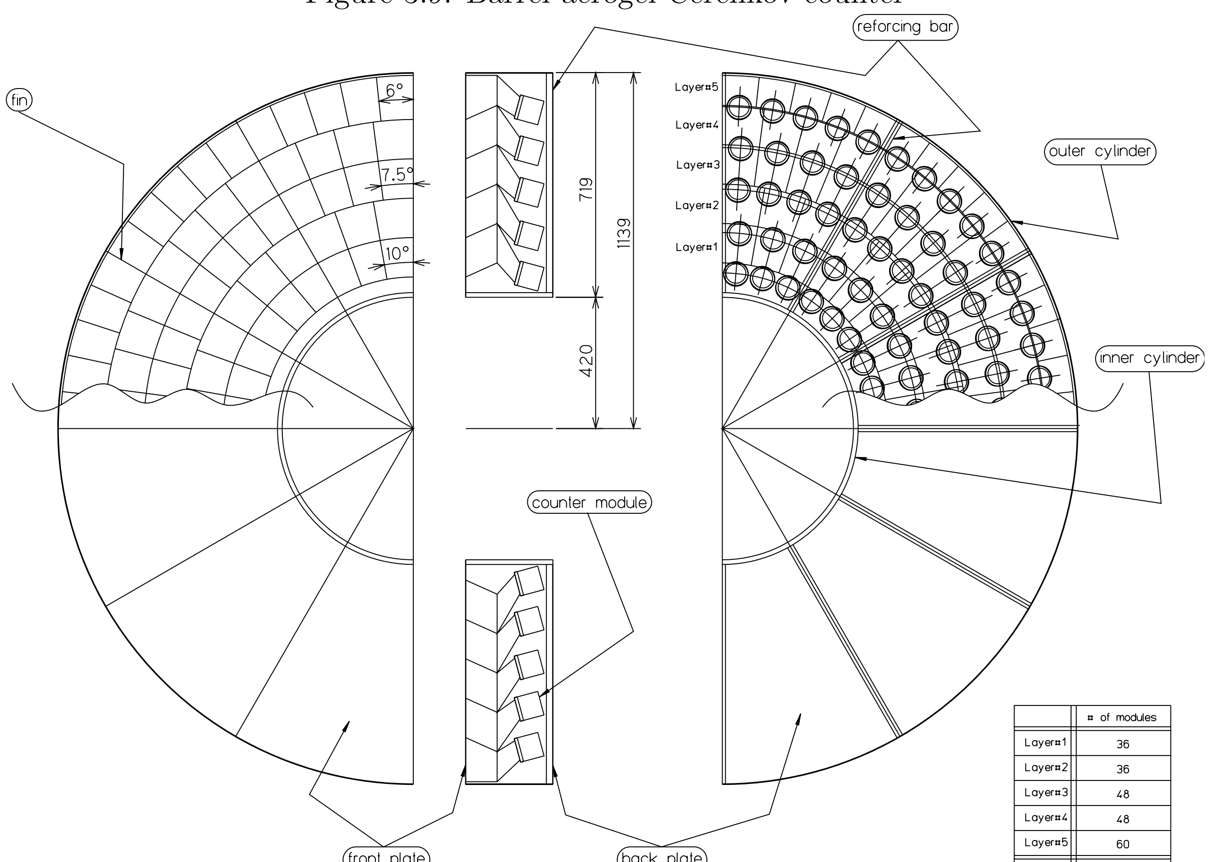

	# of modules
Layer#1	36
Layer#2	36
Layer#3	48
Layer#4	48
Layer#5	60
Total	228

Figure 3.10: *Endcap aerogel Čerenkov counter*

hits and 88% for both-end hits in μ-pair events. The configuration of TOF/TSC is shown in Figure 3.11. The time resolution for μ-pair events is shown in Figure 3.12.

3.2.5 Electromagnetic Calorimeter (ECL)

The ECL is used for detection of numerous photons, including those from π^0 decays, as well as for the electron identification. The ECL measures energy deposited by electromagnetic showers. Photons and electrons deposit most of their energies, but other kinds of particles deposit only a fraction of their energies. The matching of the energy measured by the ECL and the momentum measured by the CDC is used for the electron identification. Good energy resolution of the calorimeter results in the better hadron rejection.

Figure 3.13 shows an overall configuration of the calorimeter. The ECL consists of 8,736 CsI(Tl) crystals in total. All of the CsI(Tl) crystals are 30 cm long, and are assembled into a tower structure pointing near the interaction point. The barrel part has a 46-fold segmentation in θ and a 144-fold segmentation in ϕ. The forward (backward) endcap has a 13- (10-) fold segmentation in θ and the ϕ segmentation varies from 48 to 144 (from 64 to 144). The barrel part has 6,624 crystals and the forward (backward) endcap has 1,152 (960) crystals. Each crystal is read out by two 2 cm $\times$ 1 cm photodiodes. Barrel crystals are placed at $r = 125\,\mathrm{cm}$, while forward (backward) endcap crystals are at $z = +196\,\mathrm{cm}$ ($-102\,\mathrm{cm}$). The energy resolution is $\sigma_E/E = 0.066\%/E \oplus 0.81\%/E^{1/4} \oplus 1.34\%$ and the position resolution is $\sigma_{pos} = 0.27\,mm + 3.4\,mm/\sqrt{E} + 1.8\,mm/\sqrt[4]{E}$, where the unit of E is GeV. The performance of ECL is shown in Figure 3.14 and The position resolution is shown in Figure 3.15. The detail of ECL is described in [44].

3.2.6 Superconducting Magnet

Belle has a magnetic field of $B = 1.5T$ parallel to the beam pipe. Charged particles are forced to path on a helix trajectory whose curvature is related to the momentum of the particles.

The superconducting coil consists of a single layer of a niobium-titanium-copper alloy embedded in a high purity aluminum stabilizer. It is wound around the inner surface of an aluminum support cylinder with 3.4m in diameter and 4.4m in length. Indirect cooling is provided by liquid helium circulating through a tube on the inner surface of the aluminum cylinder.

3.2.7 The K_L/μ Detector (KLM)

The aim of the KLM is to measure the direction of K_Ls and to identify muons. A muon can be identified by comparing actual KLM hits to the expected track position extrapolated from the CDC. Since K_L is a neutral hadron, K_L rarely interacts in the inner sub-detectors and can be detected by the KLM. The KLM cannot measure K_L energy but can measure K_L direction, since deposited energy in KLM by K_L spreads widely. The measurement of K_L direction is enough for reconstruction of the $B \to J/\psi\, K_L$ decay to analyze CP

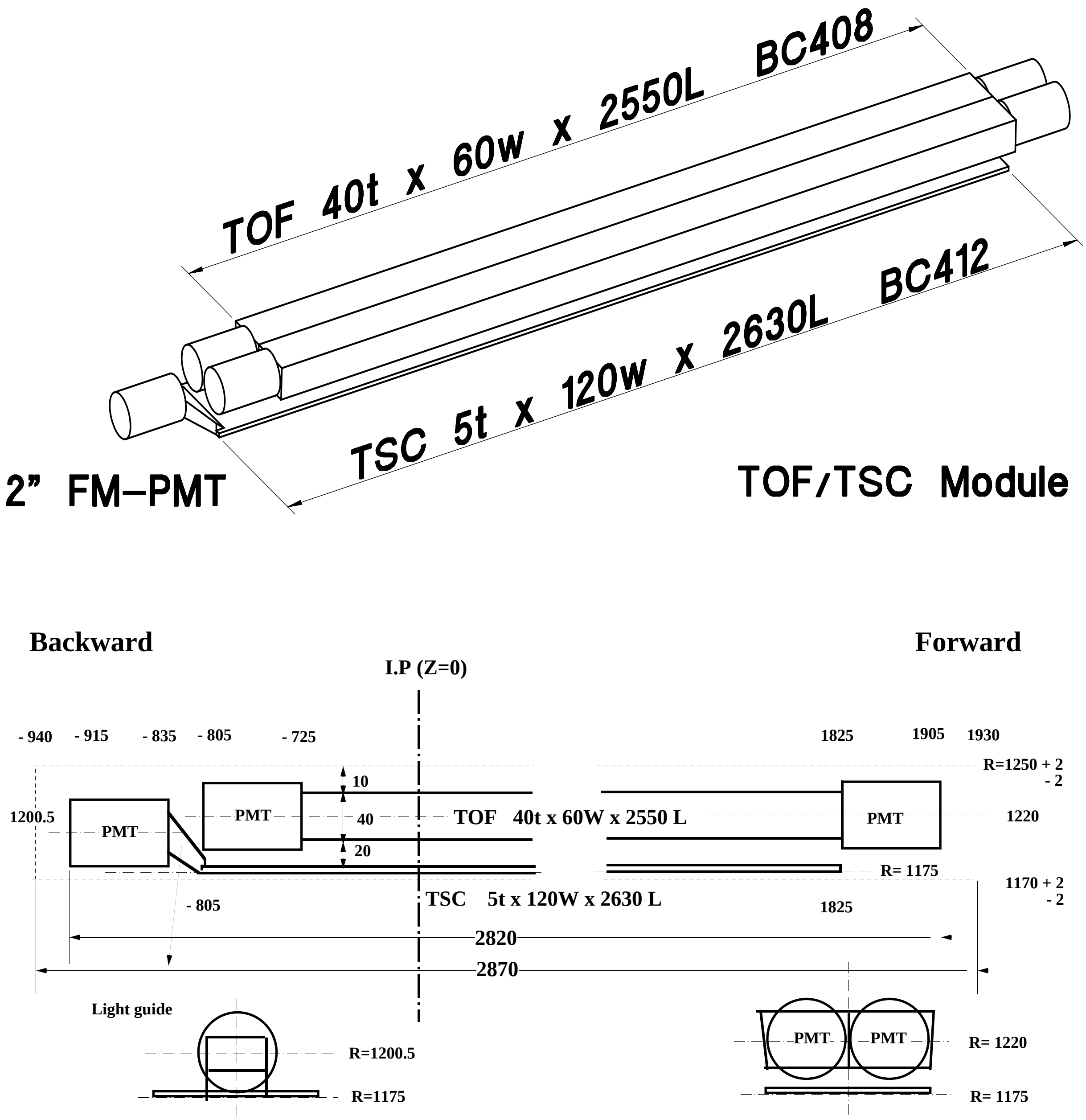

Figure 3.11: *Time of flight and trigger scintillation counters*

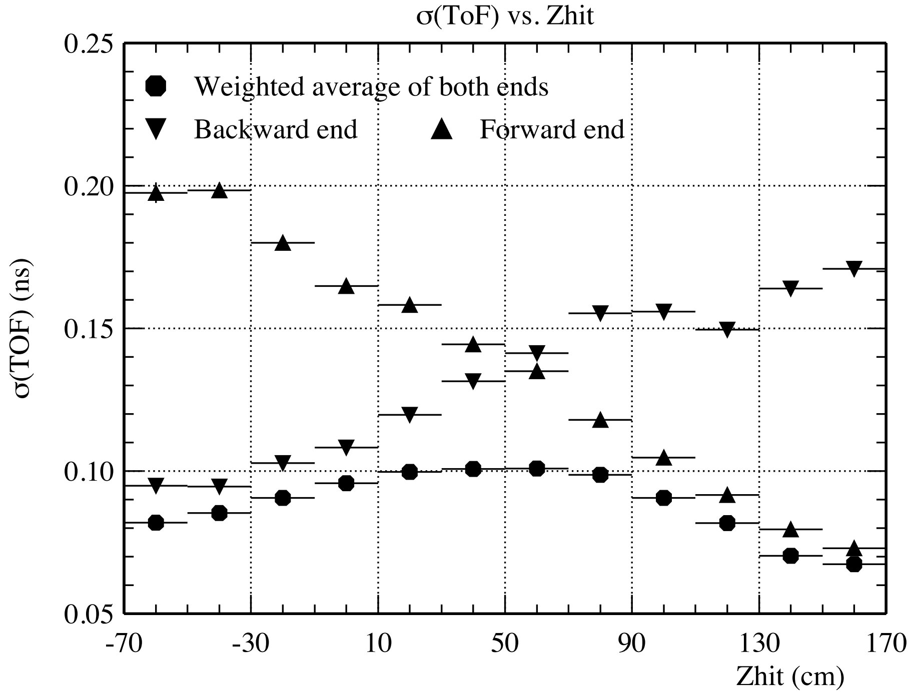

Figure 3.12: *Time resolution for μ-pair events for the TOF.*

violation, since $B \to J/\psi\, K_L$ is a two body decay and K_L momentum can be determined by using B mass constraint.

The KLM consists of 14 layers of 4.7 cm iron plates and Resistive Plate Counter (RPC) superlayers. One RPC superlayer contains two RPC planes and provides θ and ϕ information. It is the only sub-detector placed outside the coil. One additional RPC superlayer is placed in front of the first iron plate in the barrel part. An RPC is made of a 2 mm-thick glass electrode. The iron plate is an absorber material for KLM and also serves as a return path of the magnetic flux provided by solenoid magnet. Its polar angle coverage is from 20° to 155°. The configuration of barrel and endcap RPC are shown in Figure 3.16 and Figure 3.17, respectively.

Signals are read out by roughly 5 cm wide cathode strips in both θ and ϕ directions. The number of readout channels is 21,856 for the barrel part and 16,128 for the endcap part. The position resolution for K_L is $\Delta\phi = \Delta\theta = 30$ mrad and the time resolution is a few ns.

The details of the KLM are described in [44]

3.2.8 The Extreme Forward Calorimeter (EFC)

The EFC is used to measure the energy of photons and electrons scattered in the extreme forward direction, which cannot be detected by the ECL.

Since the EFC is exposed to the high irradiation (about 5 MRad per year) of photons

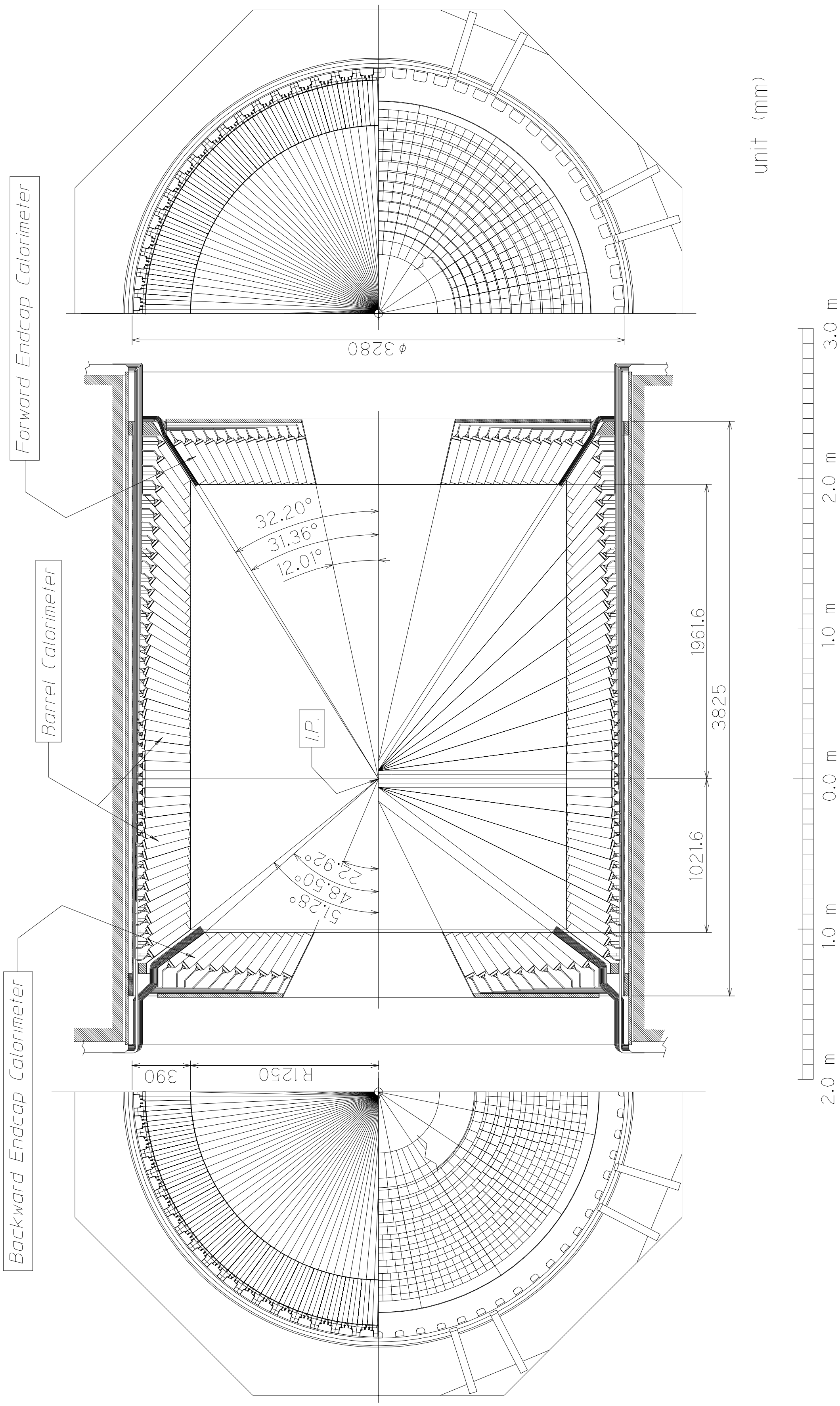

Figure 3.13: *Electromagnetic calorimeter*

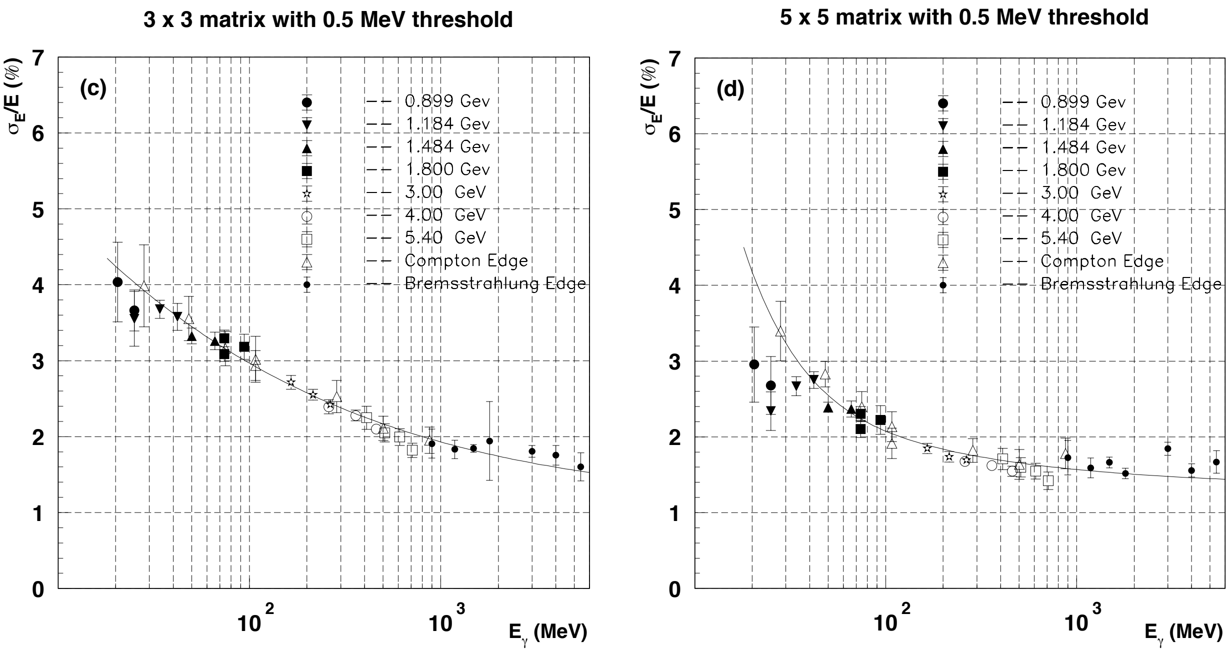

Figure 3.14: *Energy resolution as a function of the incident photon-energy for 3×3(left) and 5×5matrices with 0.5 MeV threshold.*

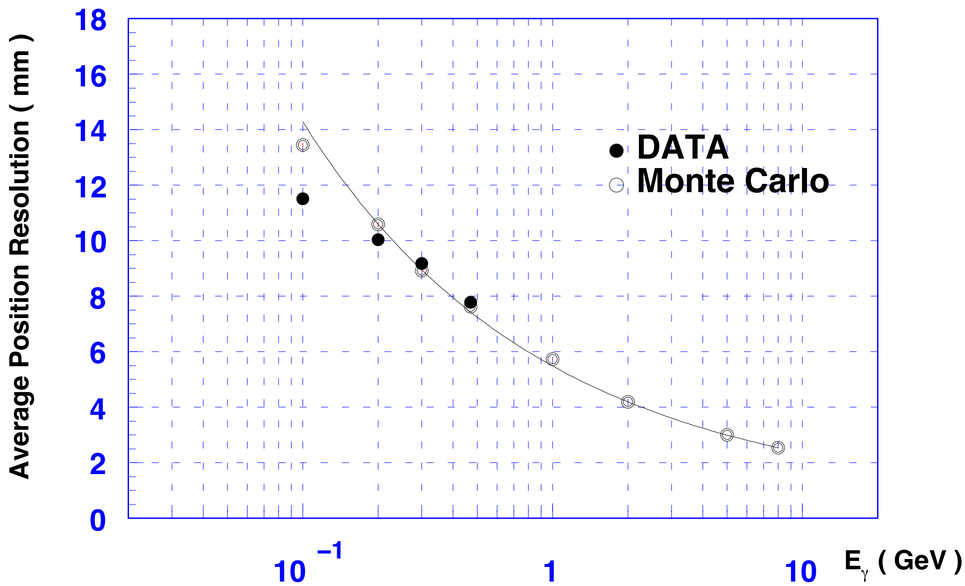

Figure 3.15: *Energy dependence of the average position resolution.*

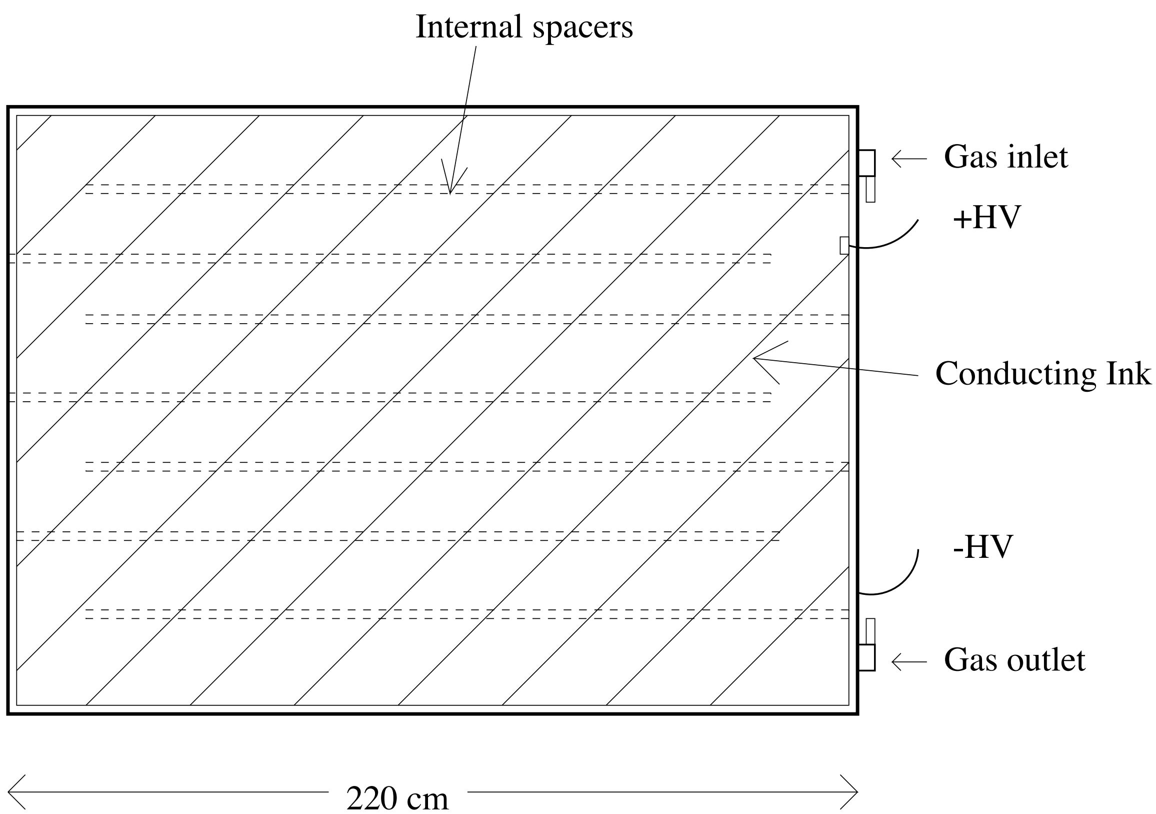

Figure 3.16: *Barrel RPC*

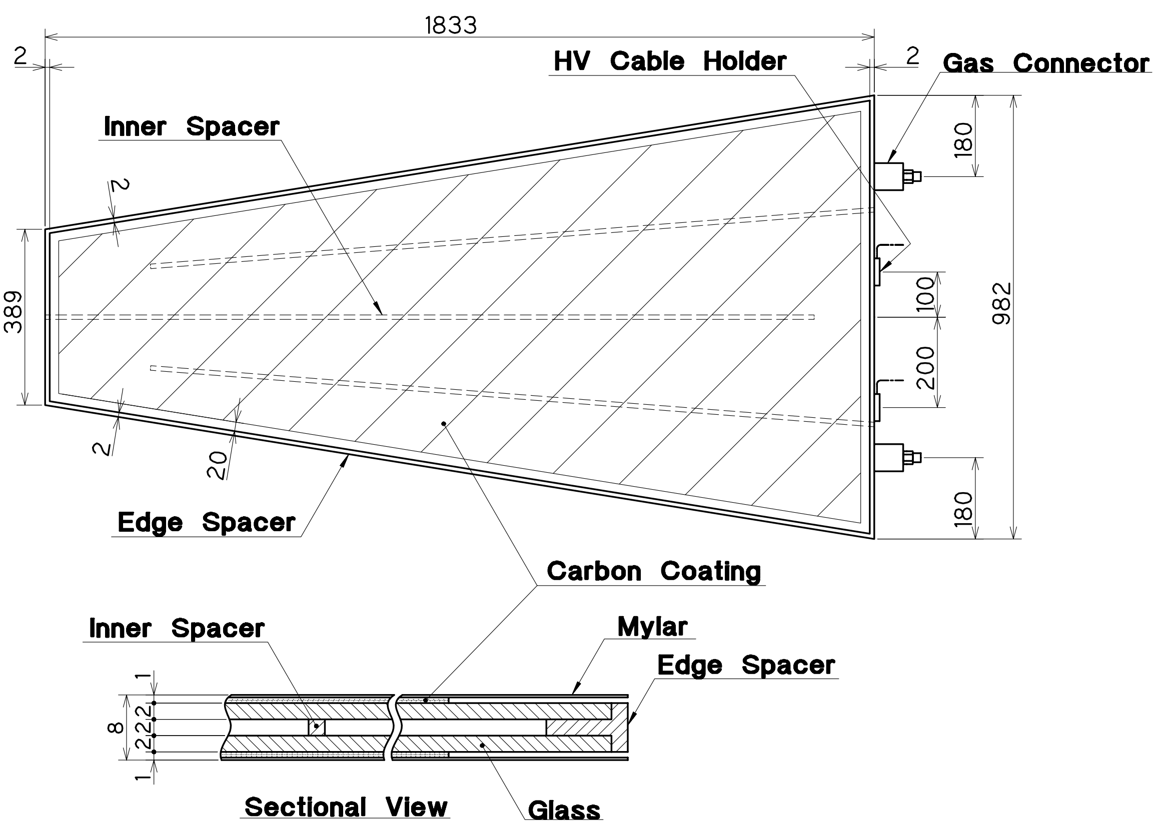

Figure 3.17: *Endcap RPC*

and electrons due to the synchrotron radiation and the spent electrons, BGO ($Bi_4Ge_3O_{12}$) crystals are used. Both forward and backward EFC consist of BGO crystals divided into 5 segments in θ and 32 in ϕ, respectively. Typical cross-section of a crystal is about $2\,\mathrm{cm} \times 2\,\mathrm{cm}$, with $12X_0$ for forward and $10.5X_0$ for backward, where X_0 is the radiation length. The EFC covers $6.4° < \theta < 12.4°$ and $162.2° < \theta < 173.4°$.

3.2.9 The Trigger/DAQ

The trigger signal is provided by several sub-detectors (see Figure 3.19). Trigger timing is determined by the TSC signal. There are two major types of triggers in the Belle system. One is provided by the tracking information from the CDC and the other is provided by the energy information from the calorimeter. The Global Decision Logic (GDL) combines the trigger signal from each sub-detector and makes a final decision to initiate a Belle-wide data acquisition within $2.2\,\mu$sec from beam crossing. The trigger rate was typically 200 Hz.

A schematic view of the Belle data acquisition system is shown in Figure 3.20. The data from the sub-detectors have to be digitized in $200\mu s$ in order to achieve the dead time less than 10% at 500Hz trigger rate. The signals from sub-detectors are converted to timing signals by the Q-to-T converters except for the KLM, which provides the time-multiplexed information on a single line, and for the SVD. All sub-detectors except the SVD use TDC readout system which is controlled by VME and FASTBUS. The data signals from the SVD are sent to flash ADC's (FADC) and the data are gathered in a memory module.

The read out data are then transfered to the Event Builder. The Event Builder combines the data from the sub-detectors to form full event records. The data are then shipped to each node of the Online Computer Farm. The Online Computer Farm formats the event data and sends them to the Mass Storage System at the Computer Center via optical fiber. The Online Computer Farm also sends the sampled events to the Data Quality Monitor (DQM) and the Event Display.

3.3 Software

In the section, we give a brief overview of the structure of the offline environment and describe Monte Carlo simulation program of Belle.

3.3.1 Offline computer system

Collected data by the Belle detector are analyzed by an offline computer system. Monte Carlo simulation is also an important task of the offline computer system. Required processing power of the offline computer system is about 30,000 MIPS. This computational power cannot be achieved by a single CPU. Therefore, parallel processing by multi-CPUs is necessary. The Symmetric Multi Processor (SMP) architecture machine was chosen as the parallel computer. The Belle offline computer system is illustrated in Figure 3.21. It

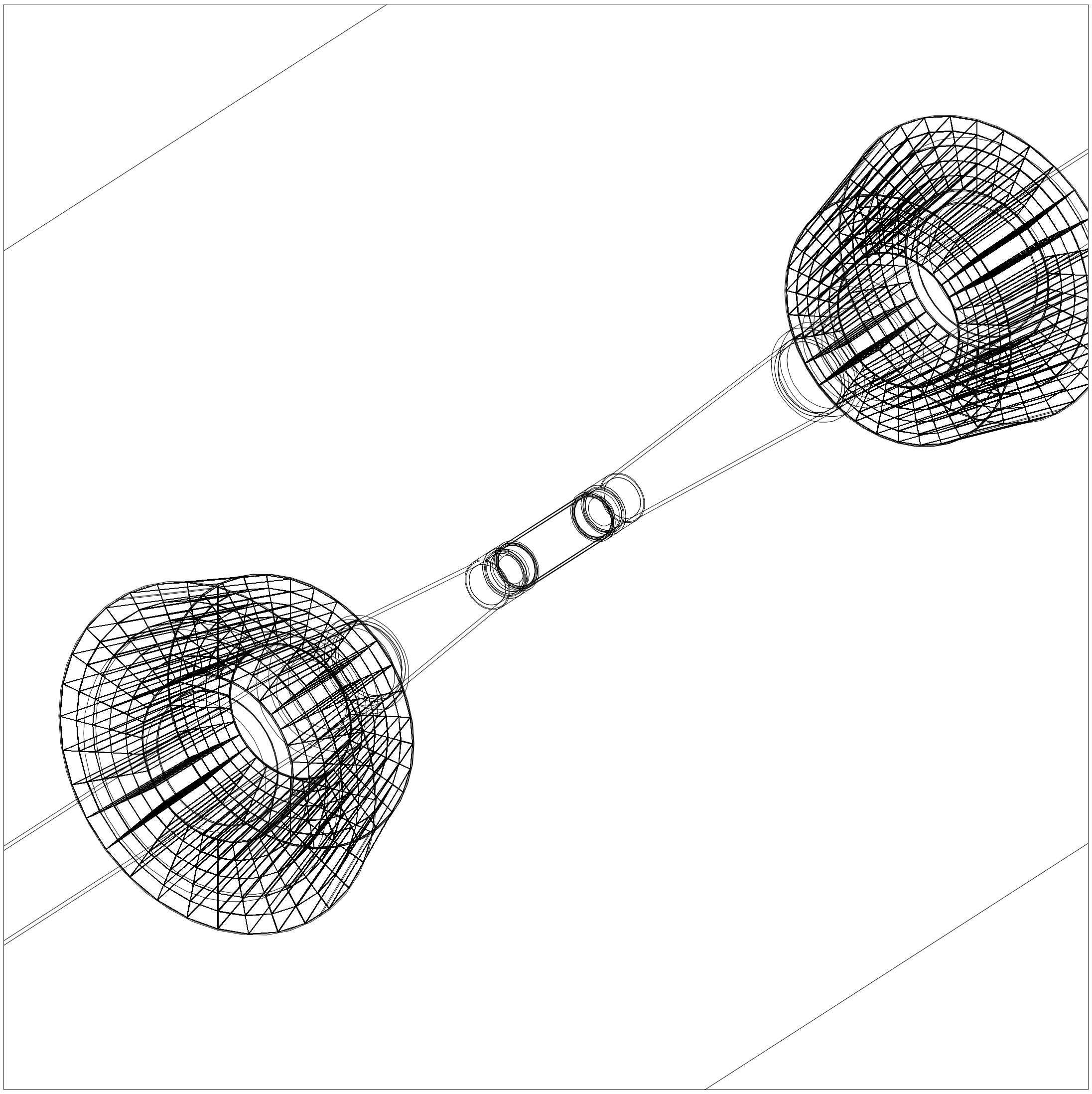

Figure 3.18: *Extreme forward calorimeter*

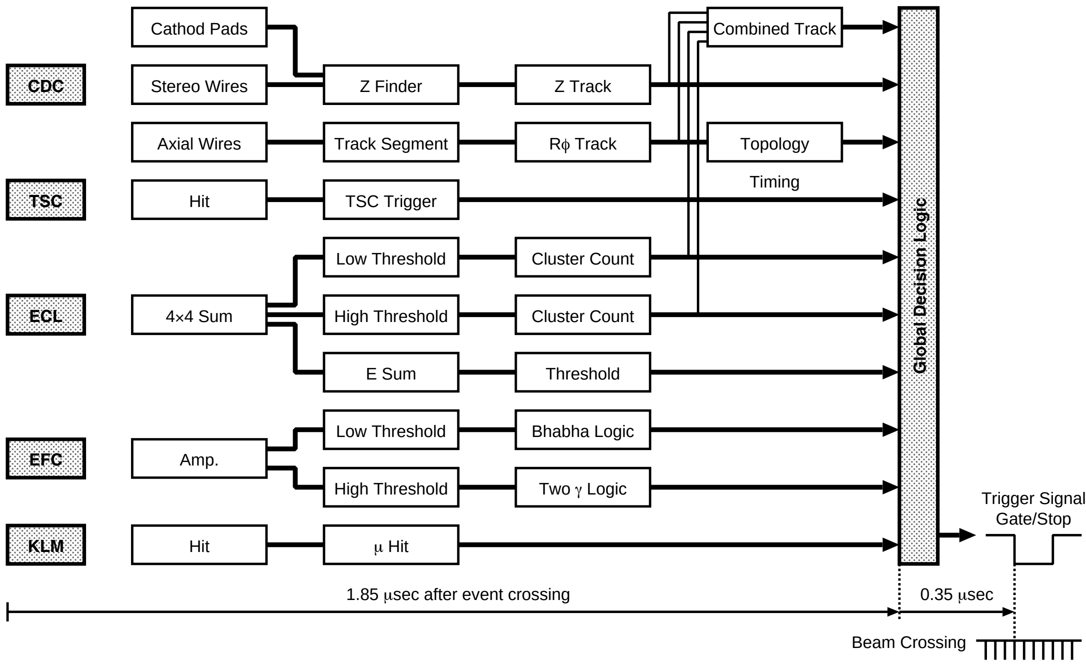

Figure 3.19: *Belle trigger system*

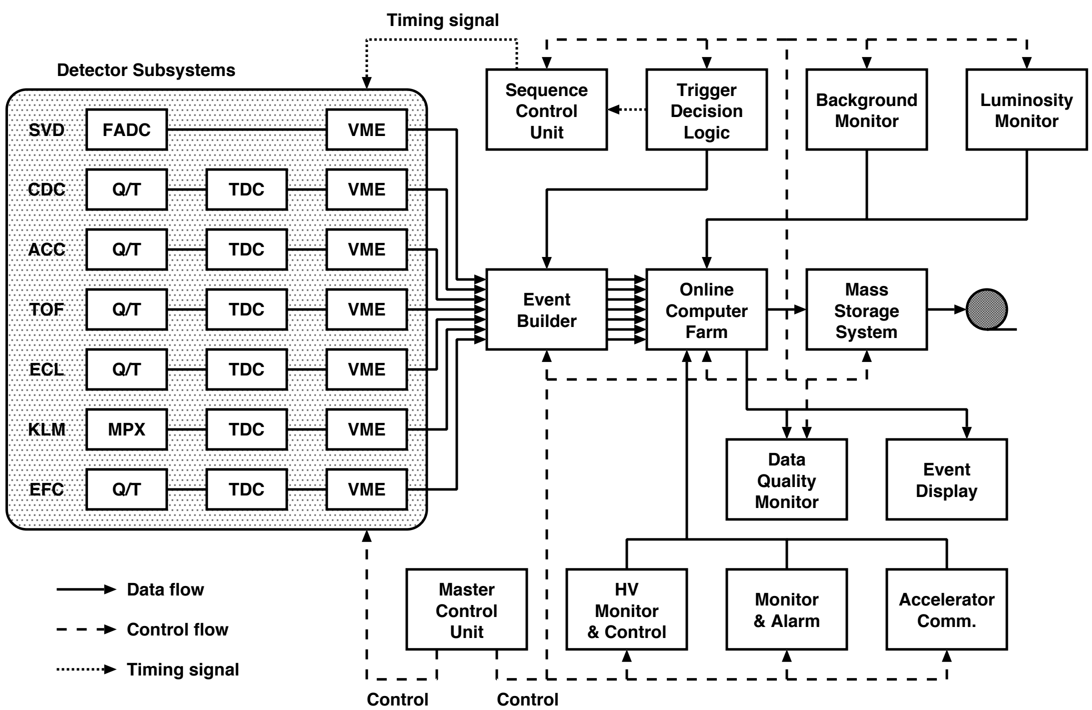

Figure 3.20: *Belle DAQ system*

Detector	Type	Configuration	Readout	Performance
Beam pipe	Beryllium double-wall	Cylindrical, r=2.0 cm 0.5mm Be/2.5mm He /0.5mm Be		Helium gas cooled
SVD	Double Sided Si Strip	300 μm-thick, 3 layers r = 3.0 - 5.8 cm Length = 22 - 34 cm	81.92 K	$19 + 50/p\beta \sin^{3/2}\theta \mu m$: r-ϕ $36 + 42/p\beta \sin^{5/2}\theta \mu m$: z $\sigma_{\Delta z} \sim 115$ μm
CDC	Small Cell Drift Chamber	Anode: 50 layers Cathode: 3 layers r = 8 - 88 cm -79$\leq z \leq$ 160 cm	A: 8.4 K C: 1.5 K	$\sigma_{r\phi} = 130$ μm $\sigma_z = 200 \sim 1,400 \mu$m $\sigma_{p_t}/p_t = (0.20 p_t \oplus 0.29)\%$ $\sigma_{dE/dx} = 7\%$
ACC	n : 1.01 $\sim$ 1.03 Silica Aerogel	$\sim$12x12x12 cm^3 blocks 960 barrel / 228 endcap FM-PMT readout	1,788	$\mu_{eff} \geq 6$ K/π 1.2<p<3.5GeV/c
TOF	Scintillator	128 ϕ segmentation r = 120 cm, 3 m-long	128$\times$2	σ_t = 100 ps K/π up to 1.2GeV/c
ECL	CsI	Towered structure $\sim$ 5.5x5.5x30 cm^3 crystals Barrel: r = 125 - 162 cm Endcap: z = -102 and +196 cm	6,624 1,152(f) 960(b)	σ_E/E= $0.066\%/E \oplus$ $0.81\%/E^{1/4} \oplus 1.34\%$ $\sigma_{pos}(mm)$= $0.27 + 3.4/\sqrt{E} + 1.8/\sqrt[4]{E}$
MAGNET	super conducting	inn.rad. = 170 cm		B = 1.5 T
KLM	Resistive Plate c.	14layers (5cm Fe+4cm gap) two RPCs in each gap θ and ϕ strips	θ:16 K ϕ:16 K	$\Delta\phi$=$\Delta\theta$=30mrad for K_L σ_t= a few ns
EFC	BGO	2x1.5x12 cm^3	θ:5 ϕ:32	σ_E/E= $(0.3 \sim 1)\%/\sqrt{E}$

Table 3.2: *Performance parameters of the Belle detector (p and p_t in* GeV/c, *E in GeV)*

consists of SMP servers, tape libraries and disk servers. These are nodes of the AP3000 and connected by the AP-Net to each other. The transfer speed of the AP-Net is 200 MB/s. The AP3000 is also connected to the ATM/FDDI LAN. There are other SMP servers (called workgroup servers) for sub-detector groups, user work stations and X-terminals, which are connected to the network. Furthermore, the SMP PC servers are used to generate Monte Carlo events. The total number of CPUs is more than 300.

In order to use the SMP servers efficiently, a framework for parallel data analyses (FPDA; Framework for Parallel Data Analysis) [45] has been developed to support parallel event processing. Based on the FPDA, BASF (Belle Analysis Framework) [46] has been developed for data analyses and Monte Carlo simulation. BASF is the main generic structure for the Belle analysis software and combines different "modules" of software to build an analysis program. A user typically provides an analysis code with a specific purpose as a module and makes use of existing external software that is necessary for the analysis. One does not need to worry about the interface between the different modules under the BASF framework. There is also a choice of more than one supported computer languages(Fortran, C and C++).

Event data are managed by Panther [47] which is a bank system based on the entity relationship model. Each user has access to a series of tables called MDST tables [48] that are converted into user-friendly form from tables of reconstruction information.

BASF provide a common analysis environment for Monte Carlo and data for users. Therefore one can analyze and compare real data to the simulation by using the same software.

3.3.2 Monte Carlo simulator

Event generator

The event generator simulates the physical process of the particle decay chains. The initial state is $\Upsilon(4S)$ or $q\bar{q}$(for continuum) and the final states consist of stable particles. The QQ98 generator was originally developed by the CLEO group [49] and has been modified for the use of the Belle analysis [50]. The QQ98 can handle both $\Upsilon(4S)$ decays and continuum process. The decay of $\Upsilon(4S)$ is performed by referring to the decay tables which contain decay modes and branching ratios mainly measured by CLEO. Users can control decays by changing the decay table. The continuum generation uses the LUND (JETSET 7.3) program [51], in which the subsequent hadronization process is based on the Lund string fragmentation model [52].

Detector simulator

The full detector simulator called GSIM, is based on GEANT [53]. GEANT is a library developed at CERN to simulate reactions between particles and matters. This simulator takes the data from the QQ98 as an input and traces the behavior of each particle in the detector, generating detector response which simulates the real detector output.

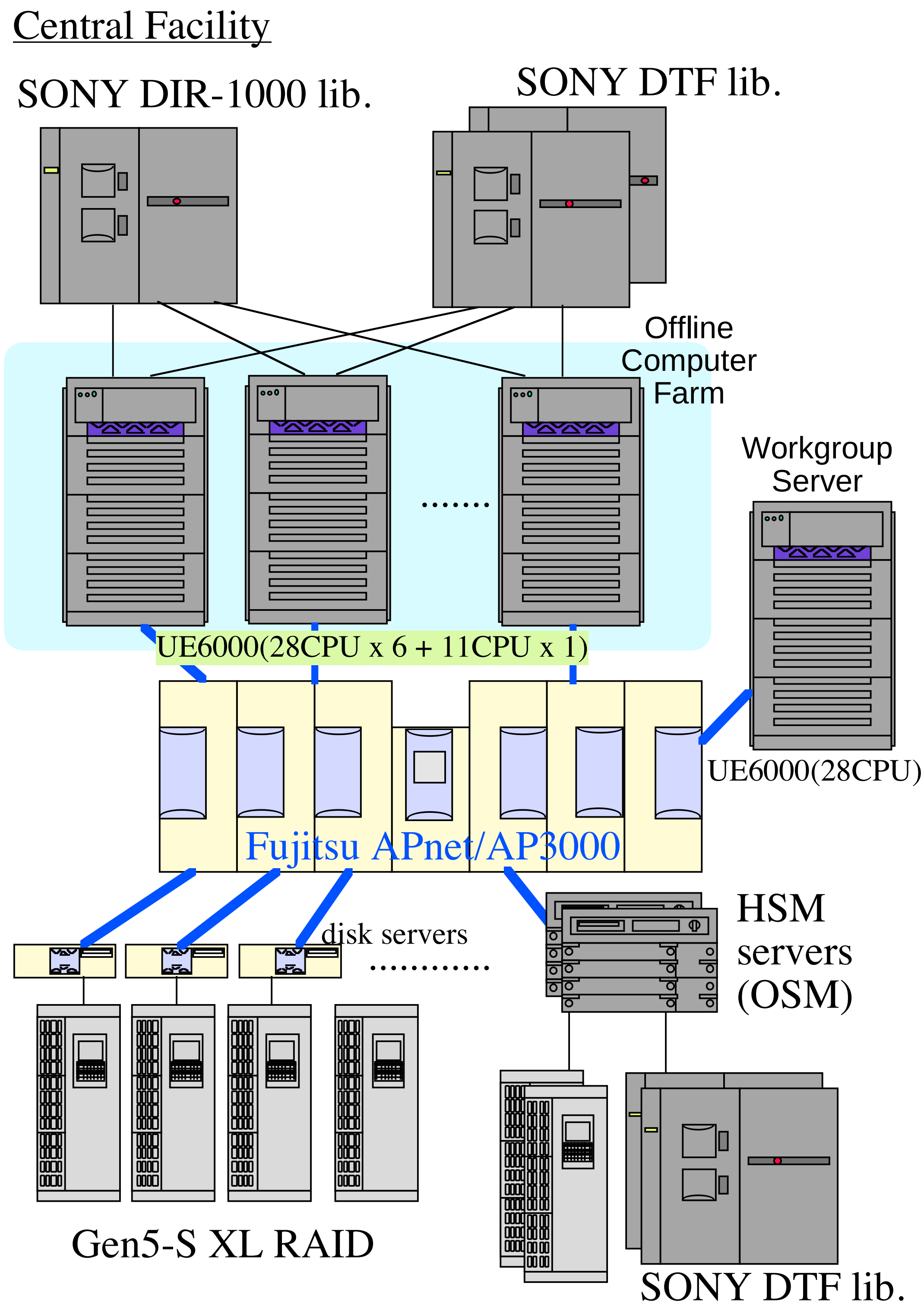

Figure 3.21: *Belle offline computer system*

Chapter 4

Selection of B^0 decays to CP eigenstates

In this section we describe the reconstruction of the B^0 decays to CP eigenstates: $J/\psi K_S$, $\psi(2S)K_S$, and $\chi_{c1}K_S$.

4.1 Event Sample

Data which we analyzed were taken in June 1999 - July 2000. Integrated luminosity is 6.8 fb^{-1} where 6.2 fb^{-1} was taken on the $\Upsilon(4S)$ resonance and 0.6 fb^{-1} off resonance, and $(6.3^{+0.16}_{-0.12}) \times 10^6$ $B\bar{B}$ pairs were created. Figure 4.1 shows the history of the daily luminosity as well as the integrated luminosity.

4.2 $B\bar{B}$ event selection

The hadronic events were selected by requiring all of the following:

- At least three "good" tracks come from the interaction point, where a "good" track was defined by (i) $|dr| < 2.0$cm and $|dz| < 4.0$cm at the closest approach to the beam axis, (ii) momentum projected onto the xy-plane (P_t) greater than 0.1GeV/c.
- More than one "good" cluster must be observed in the barrel region of the calorimeter, where a "good" cluster was defined in such a way that its energy deposit is greater than 0.1GeV.
- A sum of all cluster energies, after boosted back to the rest frame of $\Upsilon(4S)$ with an assumption of massless particle, should be between 10% and 80% of the center-of-mass energy.
- The total visible energy, which was computed as a sum of the "good" tracks assuming the mass of pion and the "good" clusters in the rest frame should exceed 20% of the center-of-mass energy.

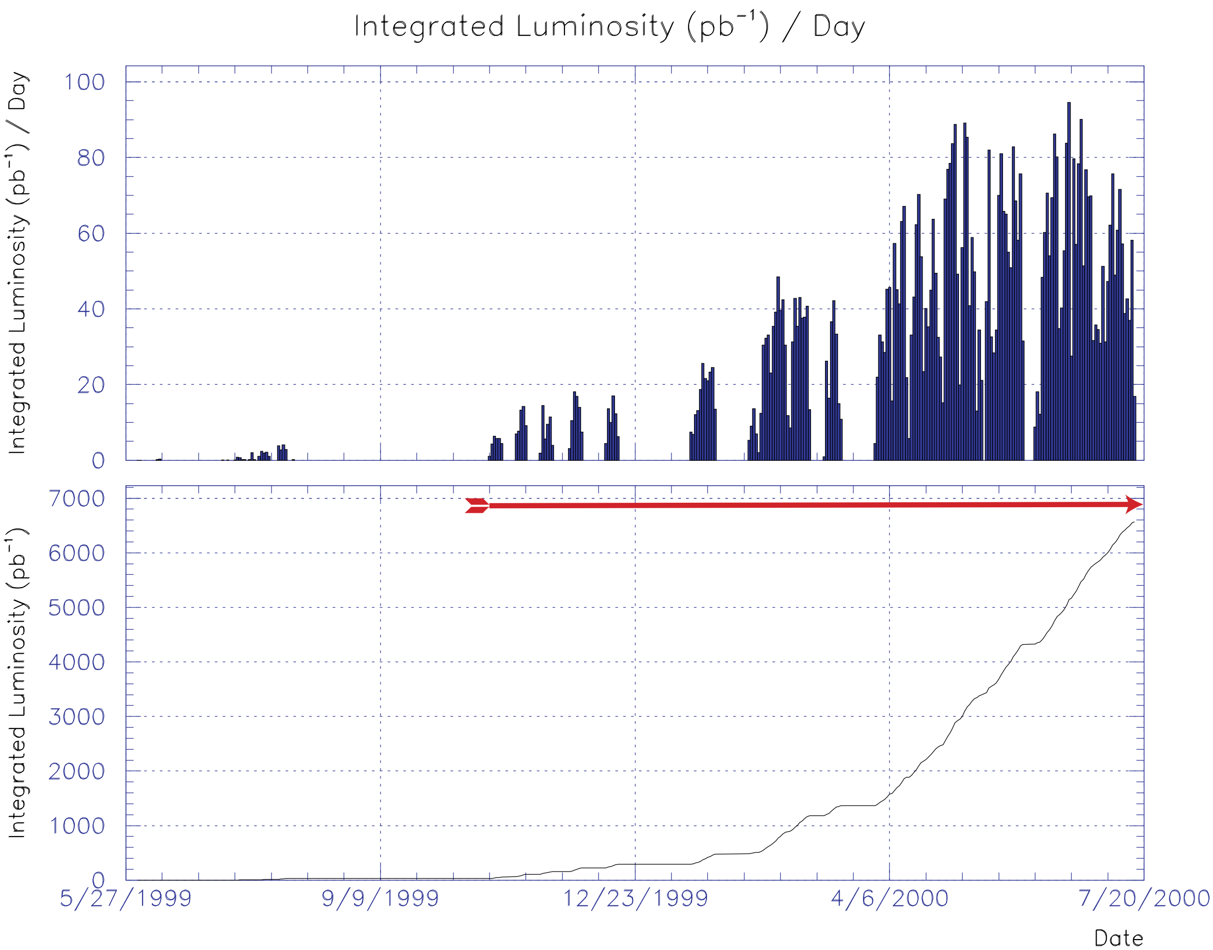

Figure 4.1: *Luminosity per day and integrated luminosity*

- The absolute value of the momentum balance in the z-component calculated in the rest frame should be less than 50% of the center-of-mass energy.

- The event vertex, which was reconstructed from the "good" tracks, must be within 1.5 cm and 3.5 cm from the interaction region in the radial and parallel directions to the beam axis, respectively.

From Monte Carlo simulations, this selection allows us to retain 92.5% of $B\overline{B}$ events. For J/ψ inclusive events, the efficiency was estimated to be 99.4%.

Events passing the hadronic event selection criteria and satisfying $H_2/H_0 \leq 0.5$, where H_2 and H_0 are the second and 0th Fox-Wolfram moments[1], are used in the subsequent analysis.

4.3 Particle identification

4.3.1 Electron identification

For electron ID we use a likelihood function, which returns the probability that the detected particle is an electron. A likelihood function is calculated from:

- the ratio of cluster energy and track momentum(E/p),

- the value of $\mathrm{d}E/\mathrm{d}x$ measured by the CDC,

- matching between the track and ECL cluster, and

- cluster shape parameter.

Optimization of the above parameters yields $\sim$ 90% ID efficiency for electrons and $\sim$ 0.5% misidentification probability for hadron tracks with $p > 1\mathrm{GeV}/c$. Performance of electron identification is shown in Figure 4.2.

We can choose an appropriate threshold value to identify electrons. For example, different thresholds are used for the reconstruction of electrons in $J/\psi \to e^+e^-$.

The details of the electron ID are described in [55].

---

[1]The k-th Fox-Wolfram moment is defined as:

$$H_k = \frac{1}{s}\sum_{i}^{N}\sum_{j}^{N}[|\vec{p_i}|\cdot|\vec{p_j}|P_k(\cos\phi_{ij})]$$

where N is the number of particles, s is the square of the center-of-mass energy, $P_k(\cos\phi_{ij})$ is the Legendre polynomial of order k and ϕ_{ij} is the angle between the vector momenta of the i-th and j-th particles. Then the Fox-Wolfram parameter R_2 is defined as H_2/H_0. R_2 is close to 1 for jetlike events such as continuum events and to 0 for spherical events like B decays. The detail is described in [54].

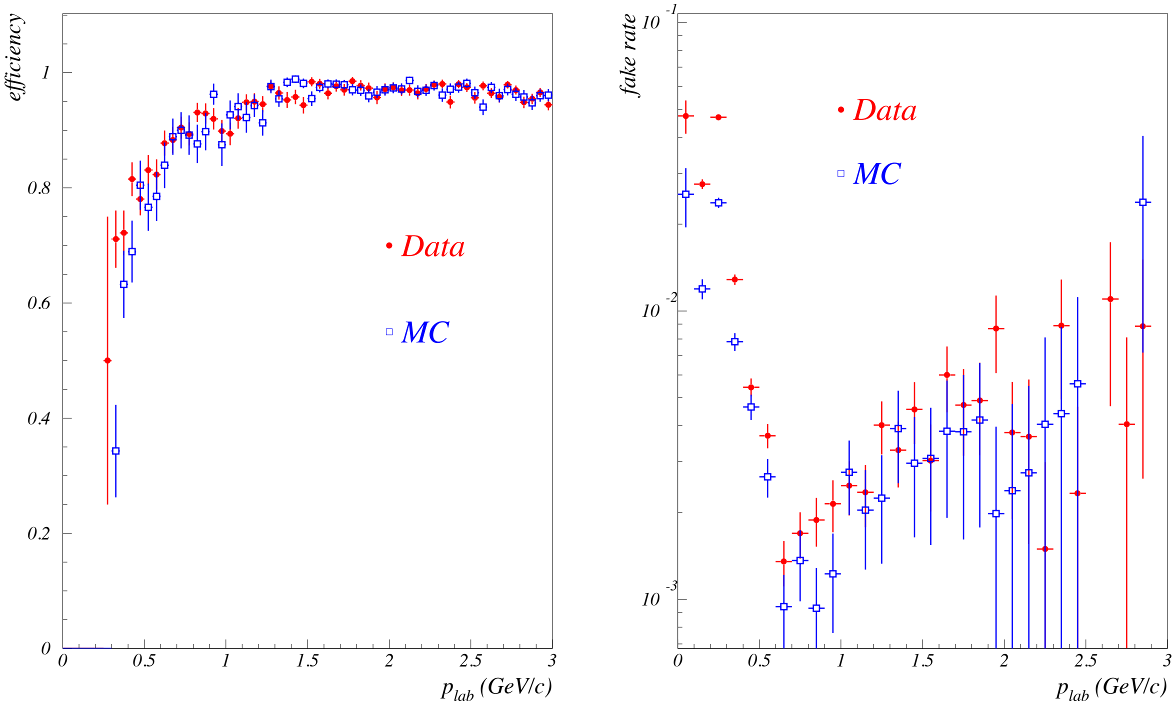

Figure 4.2: *The performance of electron identification. The left figure shows efficiency as a function of momentum in the lab. frame and the right figure shows the fake rate.*

4.3.2 Muon identification

For muon ID we also use a likelihood function. First a track which is found in the CDC is extrapolated to the KLM, then we find KLM hits and estimate expected penetration in the KLM layers. A likelihood function is calculated from the difference between the expected and the actual penetration and the distance between KLM hits and the extrapolated track. Figure 4.3 shows the performance of muon identification.

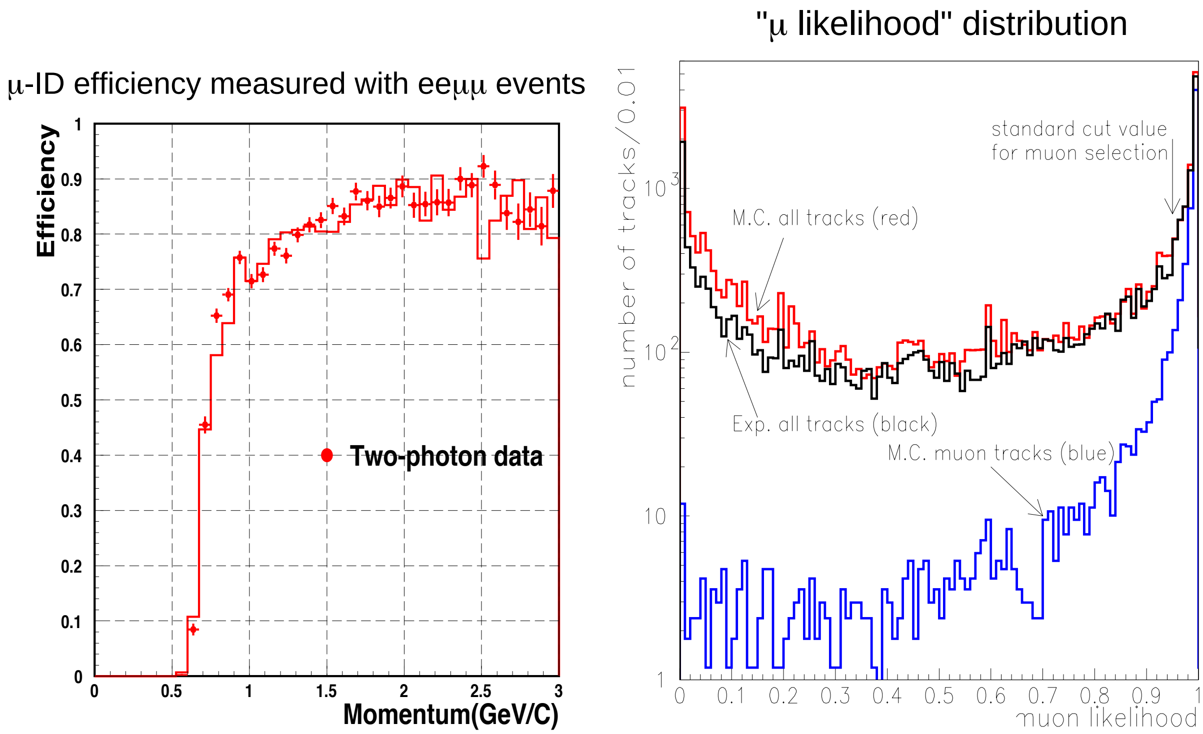

Figure 4.3: *The performance of muid identification. The left figure shows the efficiency as a function of momentum in the lab. frame and the right figure shows the distribution of the muon likelihood.*

The details of the muon ID are described in [56].

4.3.3 K/π separation

Kaon identification in Belle is based on three nearly-independent methods, dE/dx measurement by the CDC, the TOF measurement, and the measurement of the number of photoelectrons in the ACC. Each of these detector components yields good separation between particle species in a different momentum and angular region. First, we estimate probability that the charged particle is identified as kaon compared to pion for each detector. Then a net likelihood function is calculated as a product of outputs from the three detectors. Figure 4.4 shows the performance of K/π separation.

The details of K/π separation are described in [57].

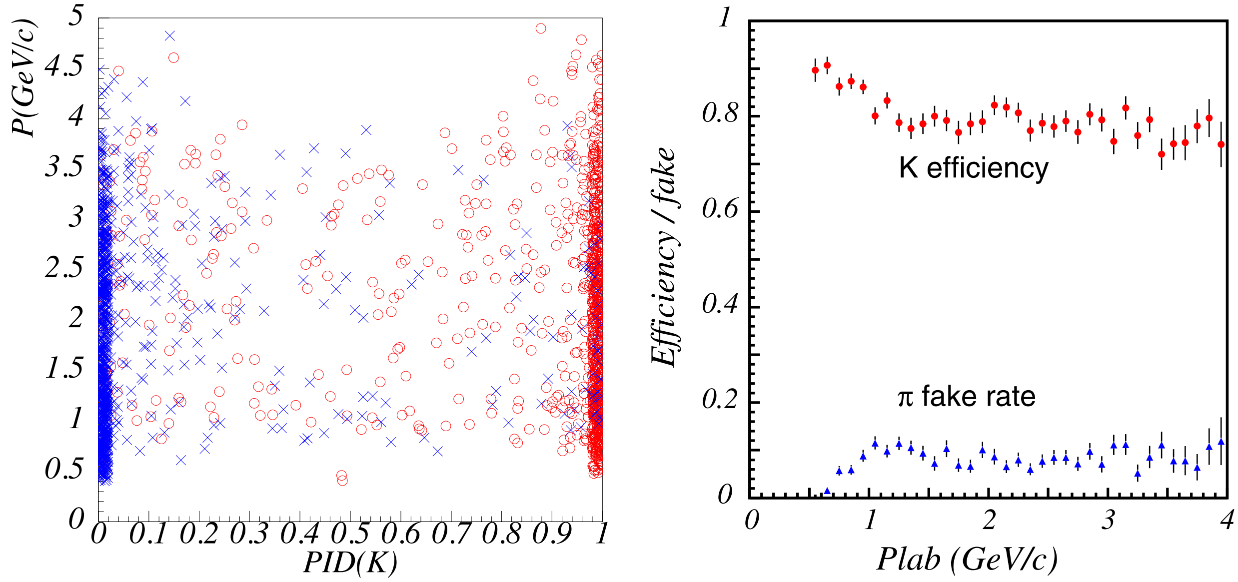

Figure 4.4: *Performance of K/π separation. The left figure is the scatter plot of kaon probability versus momentum. The open circles correspond to kaons and the cross points to pions. The right figure shows the efficiency and fake rate as a function of momentum in the lab. frame.*

4.4 $B^0 \to J/\psi K_S$ reconstruction

4.4.1 Reconstruction of J/ψ

The reconstruction of J/ψ is performed using dilepton decays, *i.e.* $J/\psi \to \mu^+\mu^-$ and e^+e^-. As shown in Table 4.1, the total branching fraction by summing these two decay modes is about 12%.

Table 4.1: *J/ψ branching ratios to decay modes of interest [19].*

Decay mode	BR	Used
$J/\psi \to e^+e^-$	$(5.93 \pm 0.10)\%$	∘
$\mu^+\mu^-$	$(5.88 \pm 0.10)\%$	∘
$2(\pi^+\pi^-)\pi^0$	$(3.37 \pm 0.26)\%$	–
$3(\pi^+\pi^-)\pi^0$	$(2.9 \pm 0.6)\%$	–
$\pi^+\pi^-\pi^0$	$(1.50 \pm 0.20)\%$	–
$2(\pi^+\pi^-)$	$(4.0 \pm 1.0) \times 10^{-3}$	–
$3(\pi^+\pi^-)$	$(4.0 \pm 2.0) \times 10^{-3}$	–

In order to remove tracks either poorly measured or from wrong interaction point, we require $|dz| < 5$cm for both the lepton tracks from J/ψ where dz represents the closest approach of the track to the origin in the z (beam) direction.

For $J/\psi \to \mu^+\mu^-$ candidates we use oppositely charged track pairs where at least one track is positively identified as a muon and the other is either positively identified as a muon or has a CsI energy deposit that is consistent with a minimum ionizing particle:

- (muon probability) > 0.1 for the tighter (*i.e.* positively identified) muon ID,
- (muon probability) > 0.1 or $0.1 <$ (CsI energy deposit) < 0.3(GeV) for the looser muon ID.

The invariant mass of J/ψ was calculated assuming the nominal muon mass ($M_\mu = 105.7\mathrm{MeV}/c^2$) for both tracks;

$$M^2_{\mu^+\mu^-} = \left(\sqrt{M^2_\mu + |\vec{P}_{\mu^+}|^2} + \sqrt{M^2_\mu + |\vec{P}_{\mu^-}|^2}\right)^2 - |\vec{P}_{\mu^+} + \vec{P}_{\mu^-}|^2.$$

If the invariant mass of the pair is in the range

$$-0.06\mathrm{GeV}/c^2 < M_{\mu^+\mu^-} - M_{J/\psi} < 0.036\mathrm{GeV}/c^2,$$

where $M_{J/\psi}$ is the mass of J/ψ ($3096.87\mathrm{MeV}/c^2$), it is identified as a $J/\psi \to \mu^+\mu^-$.

Candidate $J/\psi \to e^+e^-$ decays are oppositely charged track pairs where at least one track is identified as an electron with the tighter condition and the other track satisfies at least the dE/dx or the E/p electron identification requirement as follows:

- (electron probability) > 0.01 for the tighter electron ID,
- (e prob. with dE/dx) > 0.5 or (e prob. with E/p) > 0.5 for the looser electron ID.

In this channel, we partially correct for final state radiation or real bremsstrahlung in the inner parts of the detector by including the four-momentum of all the photons detected within 0.05 radians of the original electron direction in the e^+e^- invariant mass calculation. Invariant mass was calculated assuming the nominal electron mass ($M_e = 0.511\mathrm{MeV}/c^2$) for both tracks;

$$M^2_{e^+e^-} = \left(\sqrt{M^2_e + |\vec{P}_{e^+}|^2} + \sqrt{M^2_e + |\vec{P}_{e^-}|^2}\right)^2 - |\vec{P}_{e^+} + \vec{P}_{e^-}|^2,$$

where $\vec{P}_{e^+}$ and $\vec{P}_{e^-}$ are the momentum of positron and electron after the correction with bremsstrahlung gammas. Since the $J/\psi \to e^+e^-$ peak has a small radiative tail, we use an asymmetric invariant mass requirement,

$$-0.15\mathrm{GeV}/c^2 < M_{e^+e^-} - M_{J/\psi} < 0.036\mathrm{GeV}/c^2.$$

Events with a candidate $J/\psi \to \ell^+\ell^-$ are accepted if the J/ψ momentum in the $\Upsilon(4S)$ center-of-mass system (CMS) is below 2 GeV/c. The momentum cut value is based on an approximate monochromaticity of the B decay product in a two body decay and takes into account the B momentum spread in the $\Upsilon(4S)$ CMS. Figure 4.5 shows the invariant mass distributions for $J/\psi \to \mu^+\mu^-$ and $J/\psi \to e^+e^-$ after the selection. Mass

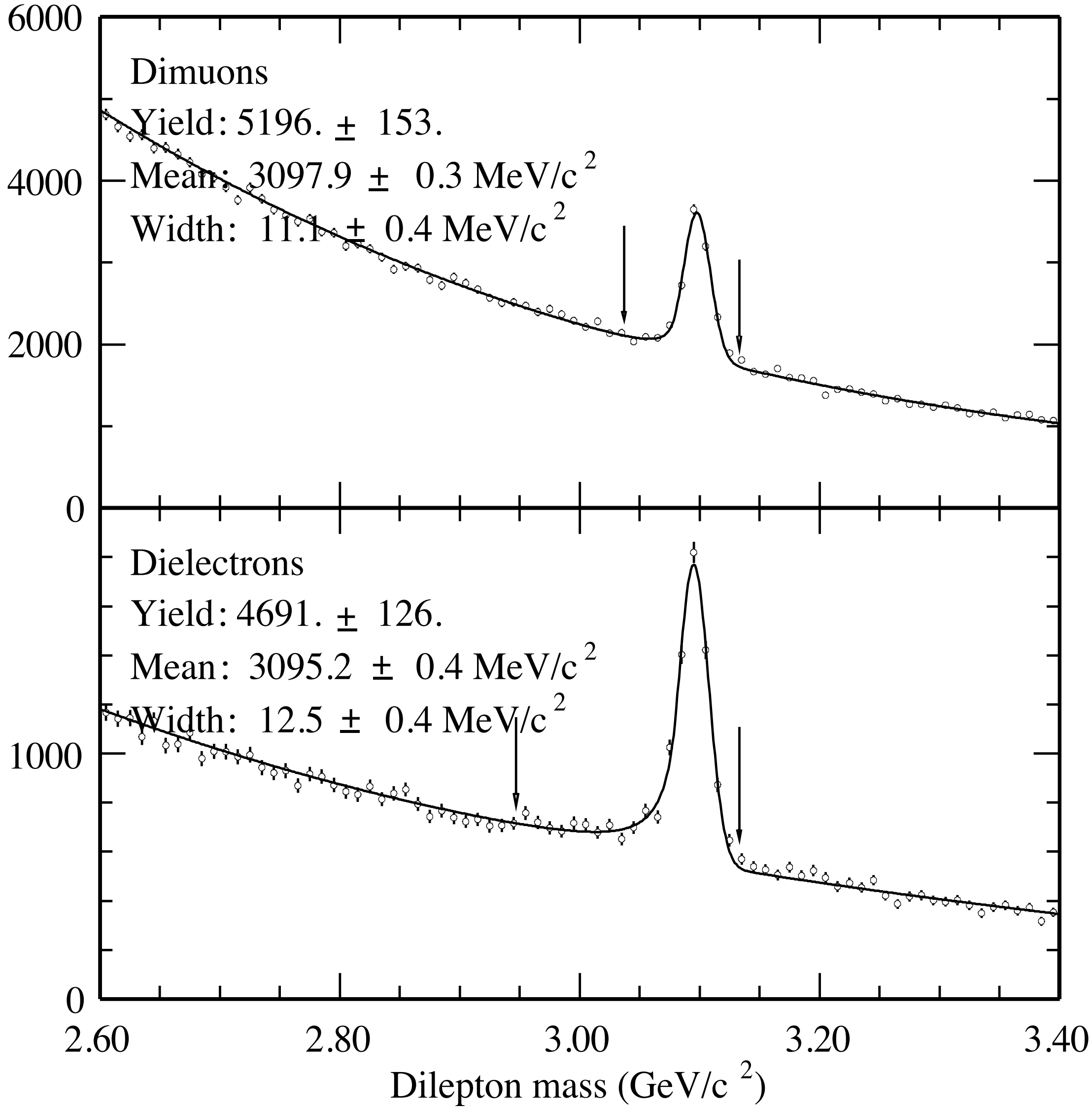

Figure 4.5: *The invariant mass distributions for $J/\psi \rightarrow \mu^+\mu^-$ (upper) and $J/\psi \rightarrow e^+e^-$ (lower).*

widths for $J/\psi \to \mu^+\mu^-$ and $J/\psi \to e^+e^-$ are 11.1 ± 0.4 MeV/c^2 and 12.5 ± 0.4MeV/c^2, respectively.

The detection efficiency of $J/\psi \to e^+e^-$ ($\mu^+\mu^-$) is estimated to be $55.0 \pm 0.2\%$ ($68.0 \pm 0.2\%$) using Monte Carlo simulation.

For the lepton tracks of the J/ψ candidates, a kinematical fit with a mass and vertex constraint is performed to improve the resolution for B reconstruction. The method of this kinematical fit is described in Section 4.7.1.

4.4.2 Reconstruction of $K_S \to \pi^+\pi^-$

K_S decays into two neutral or charged pions with branching fractions shown in Table 4.2. Since K_S has long decay length[2] compared to B^0's, we can obtain clean signals by

Table 4.2: *K_S branching ratios [19].*

Decay mode	BR	Used
$K_S \to \pi^+\pi^-$	$(68.61 \pm 0.28)\%$	○
$\pi^0\pi^0$	$(31.39 \pm 0.28)\%$	–

rejecting candidates which have short decay length.

For $K_S \to \pi^+\pi^-$ reconstruction, First, we reconstruct K_S vertex with oppositely charged track pairs. The vertex is reconstructed by the following procedure.

1. We define a temporary decay vertex of K_S as the crossing point of two tracks. The z position of the temporary decay vertex is defined as the middle point of two helices at the cross point in the r-ϕ plane.

2. Two tracks are interpolated to the temporary decay point taking into account the multiple scattering and energy loss.

3. Then the vertex is refitted with the recalculated helix parameters. If the fitting succeeds, the temporary decay vertex is replaced by the fitted one.

K_S candidates should satisfy the following conditions:

1. In case both pions have associated SVD hits, the closest distance between two pion tracks in the z coordinate is smaller than 1cm.

2. In case only one of the two pions has associated SVD hits, the closest distances of both pion tracks to the interaction point in the rϕ plane are larger than 250μm.

3. In case none of the two pions has associated SVD hits, the ϕ coordinate of the $\pi^+\pi^-$ vertex point and the ϕ direction of the $\pi^+\pi^-$ candidate's three momentum vector agrees within 0.1 radian.

[2] $\sim$ 20 cm in r-ϕ plane at Belle.

Invariant mass was calculated assigning the nominal pion mass ($M_\pi = 139.6\text{MeV}/c^2$) to both tracks:

$$M^2_{\pi^+\pi^-} = \left(\sqrt{M_\pi^2 + |\vec{P}_{\pi^+}|^2} + \sqrt{M_\pi^2 + |\vec{P}_{\pi^-}|^2}\right)^2 - |\vec{P}_{\pi^+} + \vec{P}_{\pi^-}|^2,$$

where $\vec{P}_{\pi^\pm}$ was calculated at the decay vertex of K_S. The invariant mass of the candidate $\pi^+\pi^-$ pair is required to be between 482 and 514 MeV/c^2 that corresponds to the region of $\pm 3\sigma$. Figure 4.6 is the invariant mass distribution for K_S. The mass resolution is 4.4MeV/c^2.

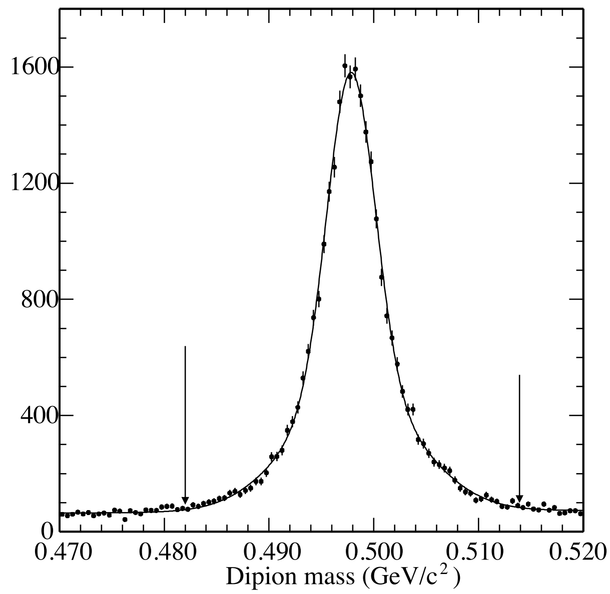

Figure 4.6: *Invariant mass distribution for K_S.*

For the pion tracks of the K_S candidates, a kinematical fit with a mass and vertex constraint is performed to improve the resolution for B reconstruction.

4.4.3 Reconstruction of B^0

For $B^0 \to J/\psi K_S$ reconstruction, we calculate the energy difference, ΔE, and the beam constrained mass, M_{bc}. The energy difference is defined as,

$$\Delta E = E_{J/\psi} + E_{K_S} - \frac{\sqrt{s}}{2},$$

where $E_{J/\psi}$ and E_{K_S} are measured J/ψ and K_S energies in the CMS and s is the center-of-mass energy in the electron-positron system. The beam constrained mass is defined as,

$$M_{bc} = \sqrt{\left(\frac{\sqrt{s}}{2}\right)^2 - p_B^2},$$

where p_B is the B candidate momentum in the CMS. The scatter plot of M_{bc} and ΔE is shown in Figure 4.7 together with projections onto each axis. B candidates are selected by requiring,

$$\begin{aligned} |M_{bc} - M_{B^0}| &< 3.5\sigma \ (0.01\mathrm{GeV}/c^2) \text{ and} \\ |\Delta E| &< 3.5\sigma \ (0.04\mathrm{GeV}). \end{aligned}$$

The M_{bc} and ΔE resolutions are 2.9MeV/c^2 and 11MeV/c^2, respectively.

As a result we obtain 70 $B^0 \to J/\psi K_S$ candidates. Efficiency of the $B^0 \to J/\psi K_S$ selection is 0.36 and the expected number of signal events are 83.1. The number of the $B^0 \to J/\psi K_S$ candidates are consistent with the Monte Carlo predictions within two sigmas.

A typical $B^0 \to J/\psi K_S$ event is displayed in Figure 4.8.

4.4.4 Estimation of background events

From Figure 4.7 we expect some background events in the signal box. The number of background events are estimated by the following two methods.

In the first method we calculate the expected number of background events by using Monte Carlo simulation. We have simulated 0.1 million inclusive J/ψ events where J/ψ is forced to decay into lepton pairs and 20 million continuum events. These MC data samples correspond to the integrated luminosity of 36.2 fb^{-1} and 6.67 fb^{-1}, respectively. $\Upsilon(4S)$ and continuum production cross sections which we assumed are 1.02 nb and 3.0 nb, respectively.

Since 10 and 3 events pass the $J/\psi K_S$ selection criteria, we expect 4.5±1.7 background events for the 6.2 fb^{-1} integrated luminosity, as shown in Table 4.3.

Inclusive J/ψ $36.2fb^{-1}$	Continuum $6.67fb^{-1}$	Inclusive J/ψ $6.2fb^{-1}$	Continuum $6.2fb^{-1}$	Total $6.2fb^{-1}$
10	3	1.72 ± 0.54	2.79 ± 1.61	4.51 ± 1.70

Table 4.3: *The estimation of background events by Monte Carlo simulation.*

In the second method we calculate the expected number of background events using the number of observed events in the sideband and the ratio of the number of MC events in the signal box to the number of MC events in the sideband. Using the M_{bc} sideband and ΔE sideband defined as,

$$\begin{aligned} M_{bc} \text{ sideband} &: -0.08\mathrm{GeV}/c^2 < M_{bc} - M_{B^0} < -0.02\mathrm{GeV}/c^2, \\ \Delta E \text{ sideband} &: 0.1\mathrm{GeV} < |\Delta E| < 0.25\mathrm{GeV}, \end{aligned}$$

we obtain 3.4 ± 2.2 and 3.7 ± 1.6 events, respectively. The average of them is 3.5 ± 1.4 and in good agreement with the first method's result. We use the results of the second method in the CP fitting. The systematic error of the number of background is estimated by the difference of two methods, then we obtain 3.5 ± 1.7.

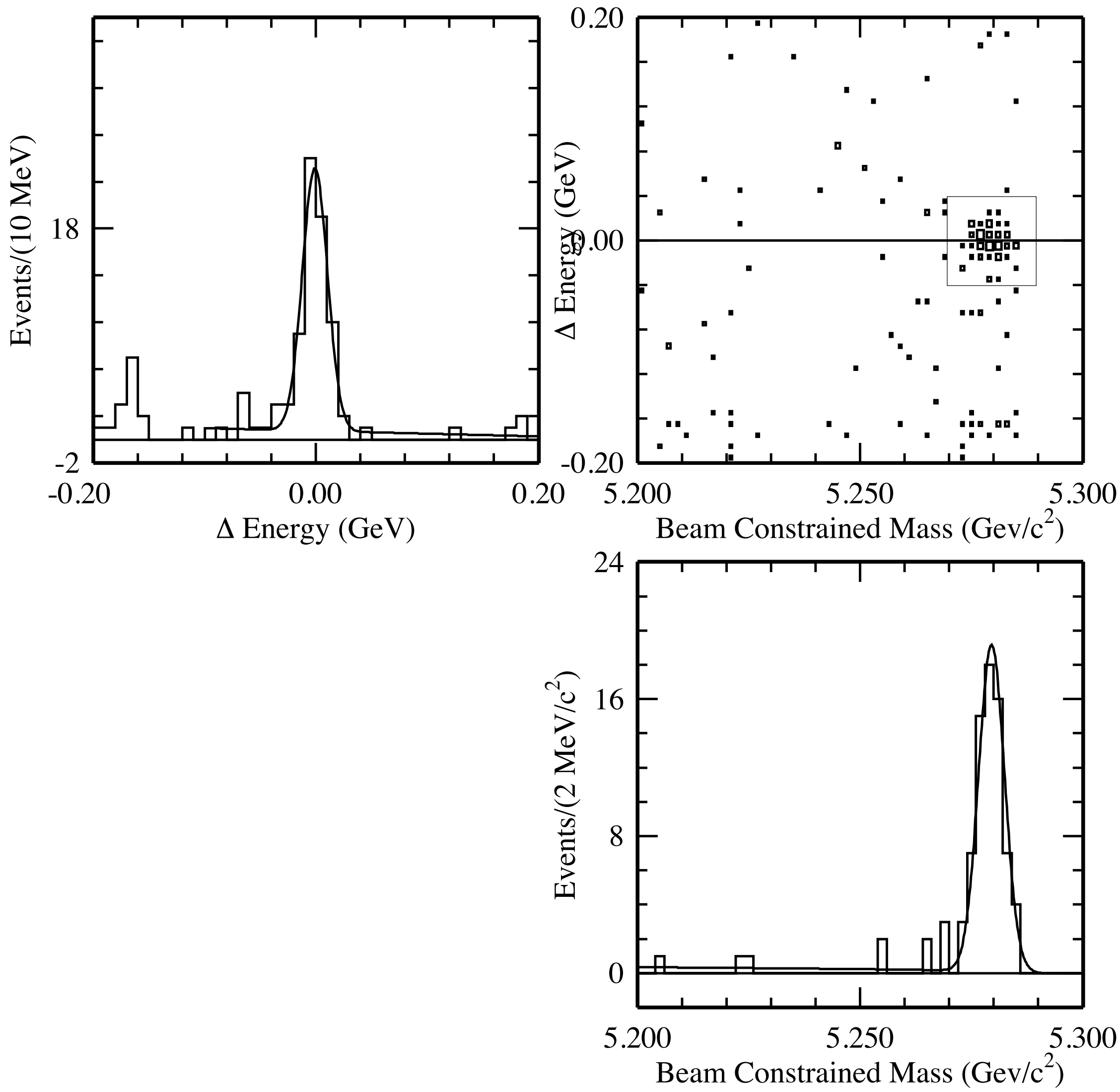

Figure 4.7: *The scatter plot of ΔE versus M_{bc} for the 6.2 fb^{-1} data. The box represents the signal region. The upper left figure is the projection to ΔE with $|M_{bc} - M_{B^0}|$ <0.01 GeV/c^2. The lower right figure is the projection to M_{bc} with $|\Delta E|$ <0.04 GeV.*

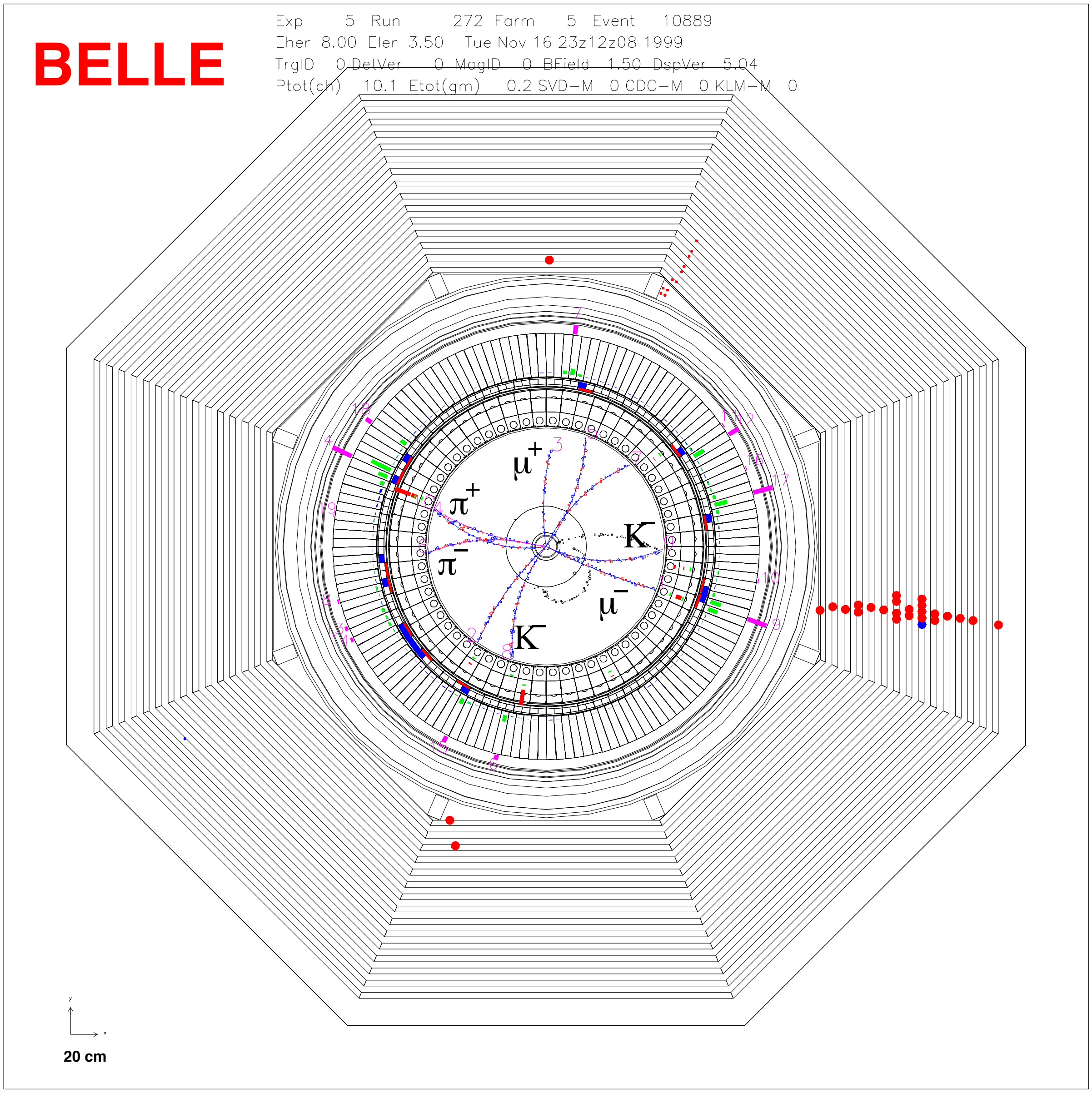

Figure 4.8: *Event display of $B^0 \to J/\psi K_S$ $J/\psi \to \mu^+\mu^-$ decay mode. We see that the other B^0 meson is $\bar{B}^0$ by the sum of charged kaon.*

4.5 Reconstruction of other CP eigenstates

In addition to $J/\psi K_S$, B^0 decays into the following CP eigenstates can be reconstructed with good signal-to-background ratios:

1. $B^0 \to \psi(2S)K_S$, $\psi(2S) \to \ell^+\ell^-$
2. $B^0 \to \psi(2S)K_S$, $\psi(2S) \to J/\psi\pi^+\pi^-$
3. $B^0 \to \chi_{c1}K_S$, $\chi_{c1} \to J/\psi\gamma$

They are also used to extract $\sin 2\phi_1$. Branching fractions of these decay modes are listed in Table 4.4.

Decay mode	BR	Reference
$\psi(2S)K^0$	$(5.0 \pm 1.1 \pm 0.6) \times 10^{-4}$	[58]
$\chi_{c1}\bar{K}^0$	$(3.9^{+1.9}_{-1.3} \pm 0.4) \times 10^{-4}$	[59]
$\psi(2S) \to e^+e^-$	$(0.88 \pm 0.13)\%$	[19]
$\psi(2S) \to \mu^+\mu^-$	$(1.03 \pm 0.35)\%$	[19]
$\psi(2S) \to J/\psi\pi^+\pi^-$	$(31.0 \pm 2.8)\%$	[19]
$\chi_{c1} \to J/\psi\gamma$	$(27.3 \pm 1.6)\%$	[19]

Table 4.4: Branching ratios related to reconstruction of other CP eigenstates.

In these reconstructions, J/ψ is reconstructed in $\ell^+\ell^-$ modes, and K_S is reconstructed in $\pi^+\pi^-$ mode. The selection of J/ψ and K_S is identical to the method mentioned in the previous section.

4.5.1 Reconstruction of $\psi(2S) \to \ell^+\ell^-$

In the reconstruction of the decay $\psi(2S) \to \ell^+\ell^-$, we require that both leptons be positively identified. Then the invariant mass of the di-lepton, $M_{\ell^+\ell^-}$, is required to be

$$-150\text{MeV}/c^2 < M_{e^+e^-} - M_{\psi(2S)} < 36\text{MeV}/c^2,$$
$$-60\text{MeV}/c^2 < M_{\mu^+\mu^-} - M_{\psi(2S)} < 36\text{MeV}/c^2,$$

respectively, where $M_{\psi(2S)}$ is the mass of $\psi(2S)$ (3685.96MeV/c^2). The average mass resolution is approximately 14 MeV/c^2. Figure 4.9 shows the $M_{\ell^+\ell^-}$ distribution.

4.5.2 Reconstruction of $\psi(2S) \to J/\psi\pi^+\pi^-$

In the reconstruction of $B^0 \to \psi(2S)K_S$ with the subsequent decay of $\psi(2S) \to J/\psi\pi^+\pi^-$, first of all $\pi^+\pi^-$ pairs with the invariant masses greater than 400 MeV/c^2 are selected. This requirement is based on the result of the Mark III experiment[60] and is essential to have a good signal-to-background ratio. For J/ψ reconstruction, the requirement is

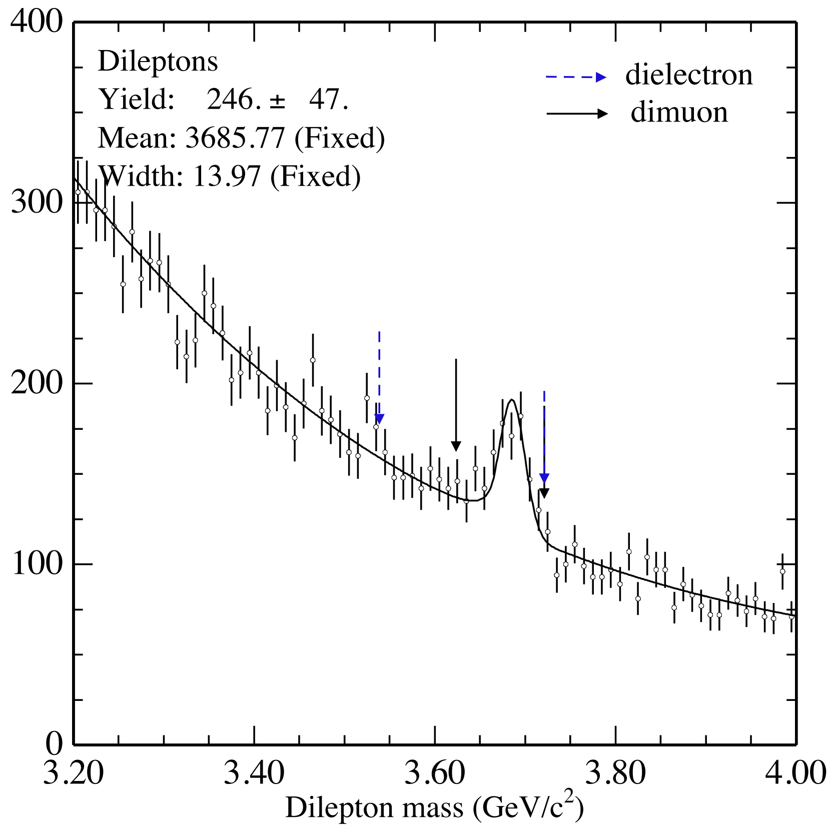

Figure 4.9: *The invariant mass distribution for* $\psi(2S) \rightarrow \ell^+\ell^-$.

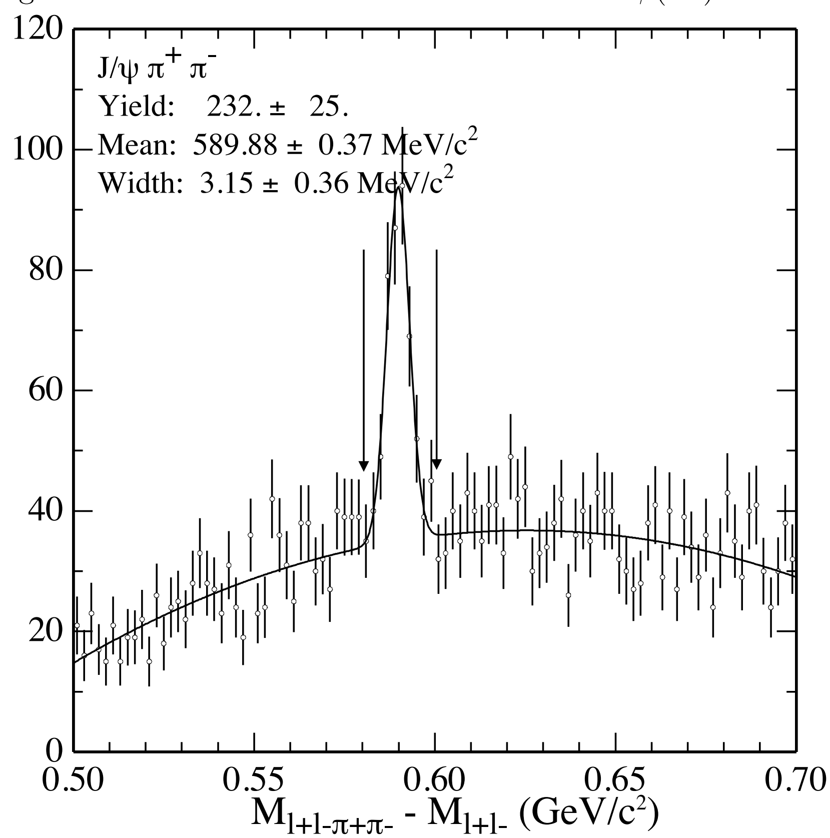

Figure 4.10: *The mass difference distribution for* $\psi(2S) \rightarrow J/\psi\pi^+\pi^-$.

similar to that for $B^0 \to J/\psi K_S$ reconstruction except that both tracks are required to be positively identified as leptons. Then the $\psi(2S) \to J/\psi\pi^+\pi^-$ candidates are selected using the mass difference, $M_{\ell^+\ell^-\pi^+\pi^-} - M_{\ell^+\ell^-}$, required to be

$$0.58\mathrm{GeV}/c^2 < M_{\ell^+\ell^-\pi^+\pi^-} - M_{\ell^+\ell^-} < 0.60\mathrm{GeV}/c^2.$$

This range corresponds to $\pm 3\sigma$ of the detector resolution (3.2MeV/c^2). Figure 4.10 shows the mass difference distribution.

4.5.3 Reconstruction of $\chi_{c1} \to J/\psi\gamma$

The $\chi_{c1} \to J/\psi\gamma$ candidates are also selected by the mass difference $M_{\ell^+\ell^-\gamma} - M_{\ell^+\ell^-}$. Since most of γ's in $B\bar{B}$ events are decay products of π^0's, γ's which form π^0 candidates with any other γ are removed, if the pair of the γ's satisfy;

- the total energy is greater than 60 MeV,
- χ^2 of π^0 mass fit is less than 10., and
- the invariant mass is within -28 to +17 MeV/c^2 from the π^0 mass.

Selection criteria for J/ψ are similar to that for $\psi(2S) \to J/\psi\pi^+\pi^-$. If the J/ψ candidate and γ which pass through the requirement above are satisfied with,

$$0.385\mathrm{GeV}/c^2 < M_{\ell^+\ell^-\gamma} - M_{\ell^+\ell^-} < 0.4305\mathrm{GeV}/c^2,$$

we take it as an χ_{c1} candidate. Figure 4.11 shows the mass difference distribution. The mass difference resolution is 7.0MeV/c^2.

4.5.4 Reconstruction of K_S for $\psi(2S)K_S$ and $\chi_{c1}K_S$

The K_S candidates are selected using cuts described in the previous section, except for $\chi_{c1}K_S$ mode, where the following tighter selection cuts are applied to reduce the background; (a) the flight length in the r-ϕ plane should be greater than 1 mm, (b) the closest approach to the J/ψ vertex in the radial direction for each $\pi^\pm$ track should be greater than 0.2mm, (c) a mis-match in the z-direction at the K_S vertex point for two $\pi^\pm$ tracks should be less than 2.5cm, and (d) the angle difference in the r-ϕ plane between the K_S momentum vector and the direction of K_S vertex point from J/ψ vertex should be less than 0.2 radian.

4.5.5 B^0 reconstruction

In order to reconstruct the B^0 for each mode, the beam energy constrained mass (M_{bc}) and the energy difference (ΔE) are used. The resolution of the beam energy constrained mass is similar to that of $B^0 \to J/\psi K_S$ described in the previous section, since the resolution is dominated by the beam energy spread of the KEKB. The selection cut applied to M_{bc} distributions is identical to the one for $B^0 \to J/\psi K_S$ described before.

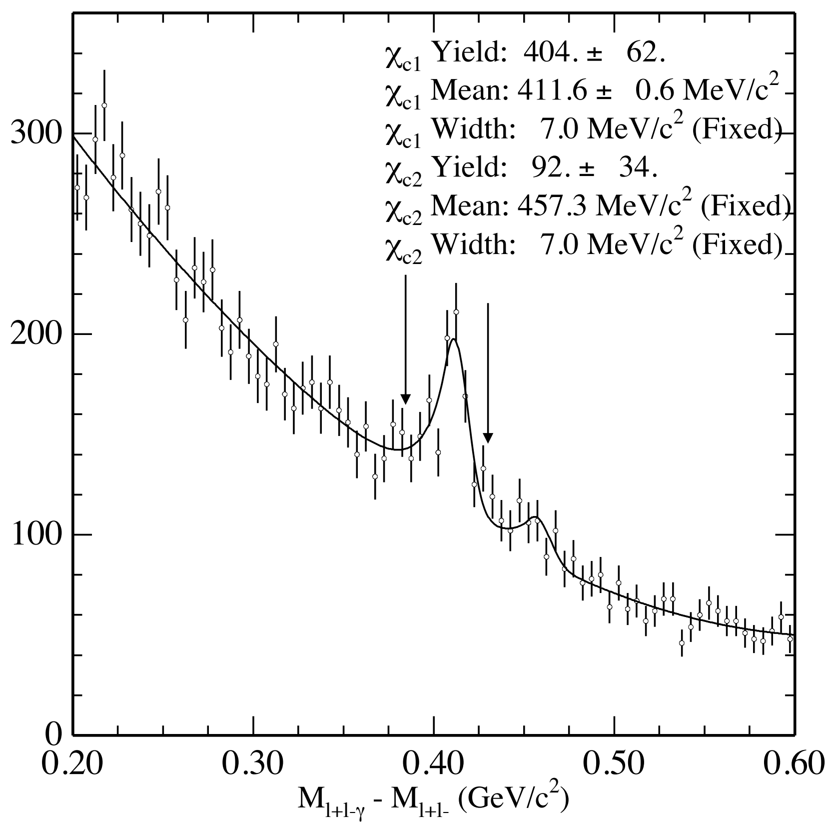

Figure 4.11: *The mass difference distribution for* $\chi_{c1} \rightarrow J/\psi\gamma$.

The ΔE distribution, on the other hand, is different for each mode. The optimized cut for each mode is applied, as listed in Table 4.5, to keep high efficiency and to suppress the background.

Figure 4.12 and Figure 4.13 shows the scatter plot for $\psi(2S)K_S$ and $\chi_{c1}K_S$.

Table 4.5: *Signal range for ΔE*

Decay mode	Lower limit (MeV)	Upper limit (MeV)
$B^0 \to \psi(2S)K_S, \psi(2S) \to \ell^+\ell^-$	-40	40
$B^0 \to \psi(2S)K_S, \psi(2S) \to J/\psi\pi^+\pi^-$	-40	40
$B^0 \to \chi_{c1}K_S$	-40	30

The efficiency and the number of observed events are listed in Table 4.6. The background events mainly come from the combinatorial events with the real J/ψ. Also listed are the numbers of expected signal and background events using Monte Carlo simulation in Table 4.6.

As seen in the table, the number of observed events is consistent with the Monte Carlo expectation.

Table 4.6: *The number of signal candidates, expected background, detection efficiency, and expected signal events.*

Decay mode	signal candidates	Expected background	Efficiency (%)	Expected signal events
$B^0 \to \psi(2S)K_S, \psi(2S) \to \ell^+\ell^-$	5	0.2	33.0	6.8±2.1
$B^0 \to \psi(2S)K_S, \psi(2S) \to J/\psi\pi^+\pi^-$	8	0.6	13.0	5.5±1.7
$B^0 \to \chi_{c1}K_S$	5	0.75	13.2	3.5±1.4

4.6 Flavor Tagging

To measure CP asymmetry, the flavor of the other B meson has to be determined. We developed the "Hamlet" package[61] for flavor tagging. We used this in this thesis.

We required $|dr| < 3$cm and $|dz| < 4$cm in all the tracks used for flavor tagging. We used four different methods to tag B flavor which are described in the following.

4.6.1 Method with high-momentum lepton

To find a high-momentum lepton coming from the semileptonic decay of B_{tag}, tracks identified as lepton were required to satisfy $p^*_\ell > 1.1\text{GeV}/c$, where p^*_ℓ is the lepton momentum at the $\Upsilon(4S)$ rest frame. The relations between the flavor of B_{tag} and the lepton are as

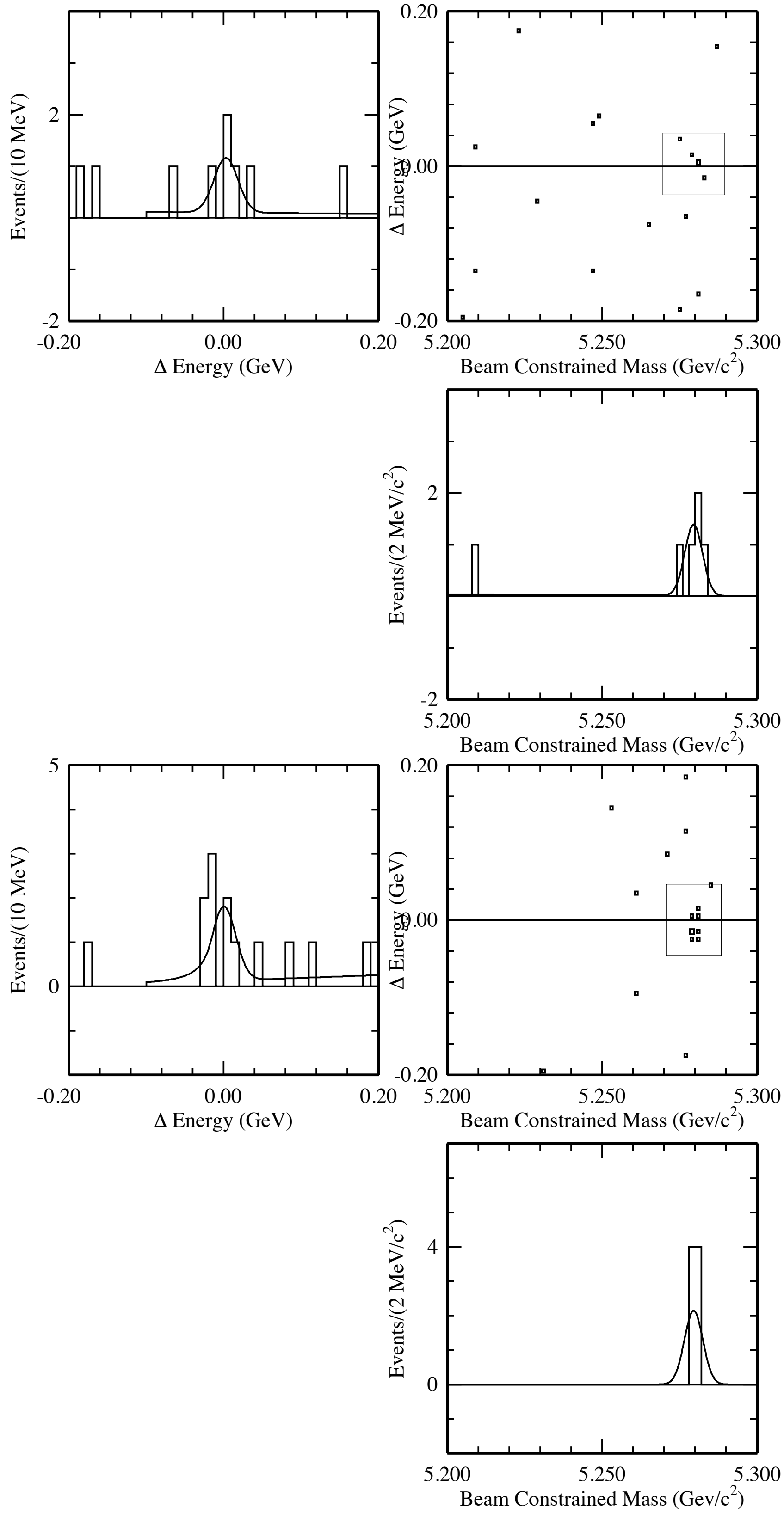

Figure 4.12: *The scatter plots of ΔE versus M_{bc} and projections for $\psi(2S)K_S$. Top figures are for $\psi(2S)K_S$ ($\psi(2S) \to \ell^+\ell^-$), bottom figures for $\psi(2S)K_S$ ($\psi(2S) \to J/\psi\pi^+\pi^-$).*

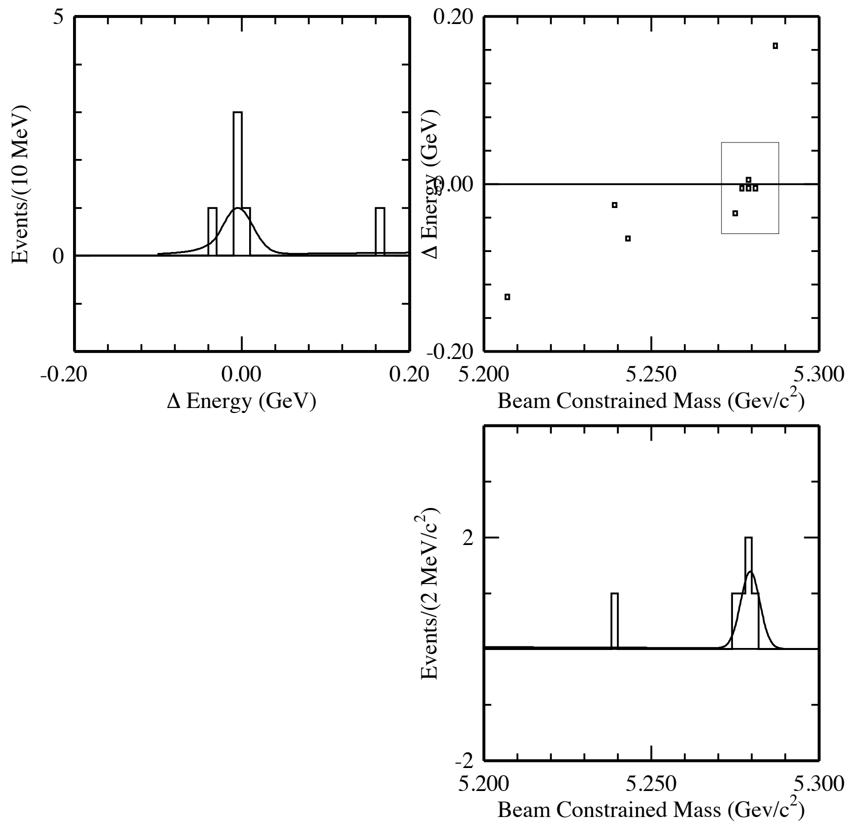

Figure 4.13: *The scatter plots of ΔE versus M_{bc} and projections for $\chi_{c1} K_S$.*

follows,

$$B_{tag} = B^0 \text{ for } \ell^+ \text{ and } B_{tag} = \overline{B^0} \text{ for } \ell^-.$$

In order to find leptons, electron is examined first. If the flavor is not determined by the electron, then muons are examined. No B flavor is assigned when two or more high-momentum electrons or muons are found.

We require the probability greater than 0.5 for electrons and 0.8 for muons, where the probabilities are described previously (Section 4.3).

This method is called "high p^*_ℓ" method in this thesis.

4.6.2 Method with charged kaon

We find charged kaons and count their total charge (Q_K). The relations,

$$B_{tag} = B^0 \text{ for } Q_K > 0 \text{ and } B_{tag} = \overline{B^0} \text{ for } Q_K < 0$$

are used.

For charged kaons, we require that the likelihood ratio is greater than 0.9 between kaons and pions, less than 0.6 between electrons and kaons, and less than 0.7 between protons and kaons.

This method is called "$K^\pm$" method in this thesis.

4.6.3 Method with medium-momentum lepton

A small lepton momentum implies a higher momentum of the accompanying neutrino. The missing momentum in the $\Upsilon(4S)$ rest frame (p^*_{miss}) is a good approximation of the neutrino momentum. Therefore we use the p^*_ℓ and p^*_{miss} when we find an identified lepton in the CMS momentum range of $0.6 \leq p^*_\ell < 1.1\text{GeV}/c$. To reconstruct p^*_{miss}, first we calculated the missing momentum in the laboratory system using all the reconstructed particles except for any K_L:

$$\vec{p}_{miss} \;=\; \vec{p}_{beam} - \vec{p}_{B_{CP}} - \sum \vec{p}_{charged} - \sum \vec{p}_\gamma,$$

where for $\vec{p}_{B_{CP}}$ we used an approximation that $\vec{p}_{B_{CP}}$ was at rest in the center of mass system. Then a Lorentz transformation is applied to obtain p^*_{miss}. If $p^*_\ell + p^*_{miss} \geq 2.0\text{GeV}/c$, we assume the B^0_{tag} decays semileptonically and assign the flavor based on the charge of the lepton as defined in Section 4.6.1.

This method is called "medium p^*_ℓ" method in this thesis.

4.6.4 Method with slow pions

If we find a low momentum ($p^* < 200\text{MeV}/c$) charged track consistent with being π from the $D^* \to D\pi$ decay, we assign that

$$B_{tag} = B^0 \text{ for } \pi^- \text{ and } B_{tag} = \overline{B^0} \text{ for } \pi^+.$$

This method is called "slow $\pi^\pm$" method in this thesis.

4.6.5 Combined tagging

We applied them in an ascending order of the wrong tagging fraction. The order is as follows: tag with high momentum leptons → tag with charged kaons → tag with medium momentum leptons → tag with slow pions.

4.6.6 Estimation of wrong tagging fraction

The efficiency and wrong tagging fraction is obtained using exclusively reconstructed $B \to D^*\ell\nu$ events from the same data sample, where $D^{*-} \to \bar{D}^0\pi^-$ and $\bar{D}^0 \to K^+\pi^-$ are used. Event selection and vertex reconstruction of $B \to D^*\ell\nu$ are described in Appendix A. Here, we define

- Tagging efficiency: $\epsilon_{tag} = N_{tag}/N_{rec}$, where N_{rec} and N_{tag} are the number of reconstructed and tagged events, respectively.
- Wrong tagging fraction: w_{tag} = (number of wrongly tagged events)/(total number of tagged events)
- Effective tagging efficiency: $\epsilon_{eff} = \epsilon(1 - 2w_{tag})^2$

Monte Carlo expectation for the $B^0 \to J/\psi K_S$ decay is shown in Table 4.7.

Table 4.7: *Tagging efficiencies (ϵ_{tag}), wrong tagging fractions (w_{tag}), and effective tagging efficiencies (ϵ_{eff}) obtained with Monte Carlo simulation.*

	mode	ϵ_{tag} (MC)	w_{tag} (MC)	ϵ_{eff} (MC)
B^0	high p^*_ℓ	0.123	0.088	0.084
	$K^\pm$	0.275	0.161	0.127
	medium p^*_ℓ	0.029	0.292	0.005
	slow $\pi^\pm$	0.070	0.341	0.007

Taking into account the wrong tagging fraction, the time evolution of the neutral B-meson pair with the opposite flavor (OF) and same flavor (SF) is given by

$$\begin{aligned}\mathcal{P}_{OF}(\Delta t) &\propto 1 + (1 - 2w_{tag})\cos(\Delta m \Delta t),\\ \mathcal{P}_{SF}(\Delta t) &\propto 1 - (1 - 2w_{tag})\cos(\Delta m \Delta t).\end{aligned}$$

The wrong tagging fraction determines the oscillation amplitude of the OF-SF asymmetry,

$$A_{mix} = \frac{OF - SF}{OF + SF} = (1 - 2w_{tag})\cos(\Delta m_d \Delta t).$$

We fit the time evolution of the OF and SF events and obtain the wrong tagging fraction.

We apply the flavor tagging mentioned above to the tagging-side, treating the tracks used by the reconstruction of $B \to D^*\ell\nu$ decay as the CP-side tracks. We also used the same method to obtain a tagging-side vertex reconstruction, which is described in detail later.

We obtain the wrong tagging fraction by fitting the Δz distribution of the SF and OF events. Figure 4.14 shows the OF-SF asymmetry as a function of Δt for tagged $D^{*\mp}\ell^{\pm}\nu$ events with fit curves.

We have estimated systematic errors of w_{tag}'s due to uncertainty in the resolution function, backgrounds, and the Monte Carlo parameters used in the fit. The results are summarized in Table 4.8. These give total effective tagging efficiency of $0.185^{+0.035}_{-0.034}$ which is consistent with the Monte Carlo simulation.

Table 4.8: *Summary of the tagging efficiencies (ϵ_{tag}), wrong tagging fractions (w_{tag}), and effective tagging efficiencies (ϵ_{eff}) for the data.*

mode	ϵ_{tag} (data)	w_{tag} (data)	ϵ_{eff} (data)
high p^*_ℓ	$0.126 \pm 0.004(stat.)$	$0.081^{+0.059}_{-0.052}(stat.+syst.)$	$0.088^{+0.015}_{-0.014}(stat.)$
$K^{\pm}$	0.273 ± 0.008	$0.212^{+0.051}_{-0.049}$	$0.090^{+0.028}_{-0.027}$
medium p^*_ℓ	0.036 ± 0.013	$0.415^{+0.109}_{-0.105}$	0.001 ± 0.008
slow $\pi^{\pm}$	0.075 ± 0.003	$0.362^{+0.079}_{-0.077}$	0.006 ± 0.012
total	0.510 ± 0.016	-	$0.185^{+0.035}_{-0.034}$

4.7 Vertex reconstruction

The proper time difference, Δt, is given by $\Delta t \simeq \Delta z/c\beta\gamma$, where $\beta\gamma$ is the Lorentz boost factor due to the asymmetric beam energy ($\beta\gamma = 0.425$ at KEKB) and Δz is the distance between the decay vertices of the two B mesons along the boost axis. The difference between B^0 and $\bar{B}^0$, or positive and negative time scale, reflects the CP asymmetry. When the finite time resolution is included, the difference between the positive and negative time scale is diluted. The errors of measured vertex point reduce the sensitivity of the CP violation measurement. The penalty for resolution of $\Delta t/\tau_B = 0.5$ (as compared to perfect vertex resolution) corresponds to about 30% increase in the required luminosity which is tolerable. As the mean decay length of B meson at Belle is about 200μm, the Δz resolution of $\sim 100\mu$m needs to be achieved. Thus precise measurement of proper time difference is one of the key issues in the study of mixing-induced CP violation in B decays.

4.7.1 Vertex reconstruction of B_{CP}

The vertices for the CP-side are reconstructed using leptons from J/ψ and the constraint coming from the interaction point profile (IP profile) smeared with finite B flight length in the r-ϕ plane (See Figure 4.15). We use leptons only if there are sufficient numbers of SVD hits associated with the Kalman filtering technique; *i.e.* with both z and r-ϕ hits

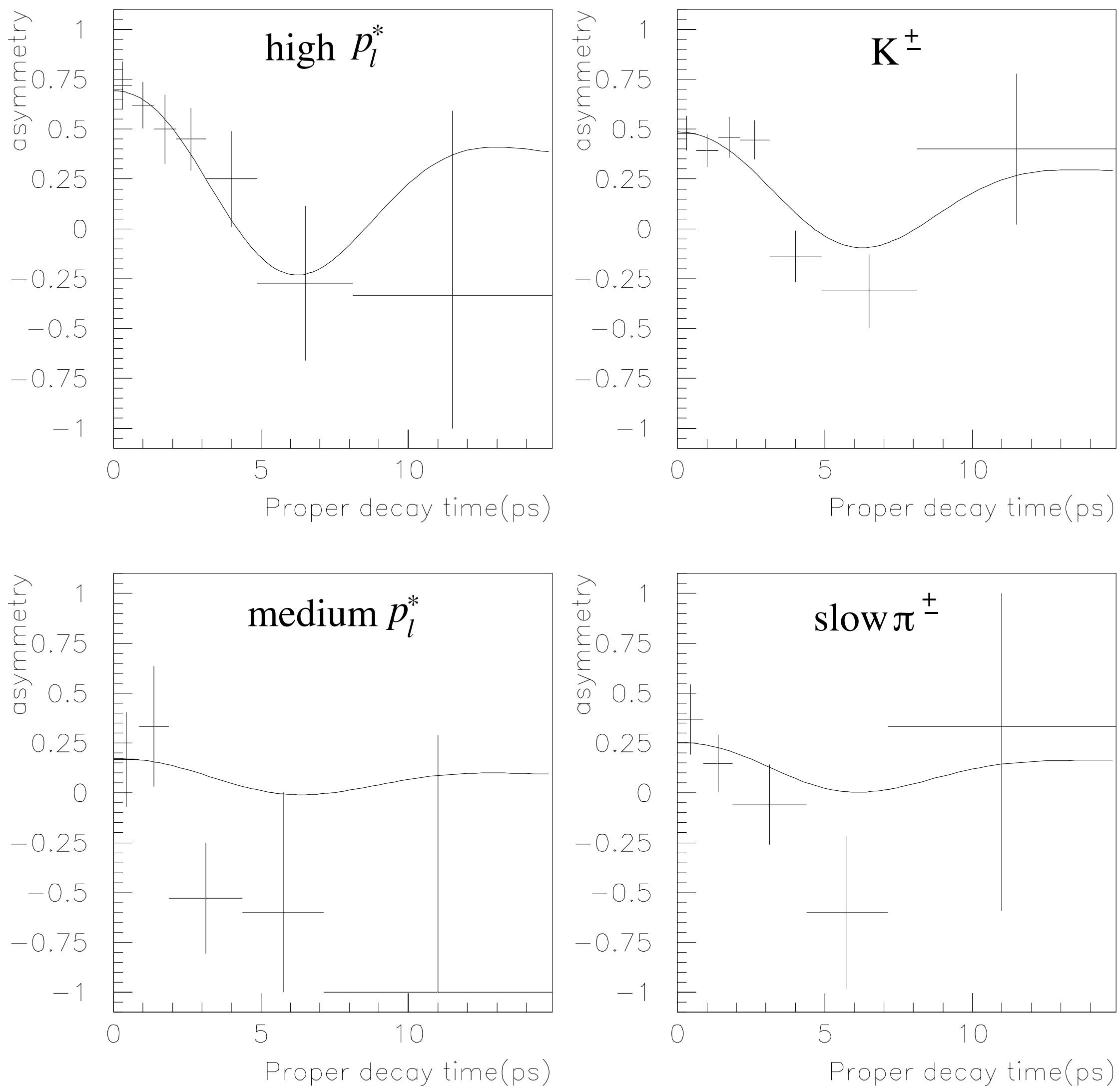

Figure 4.14: *Asymmetry as a function of proper decay time difference for* $D^{*\mp}\ell^\pm\nu$.

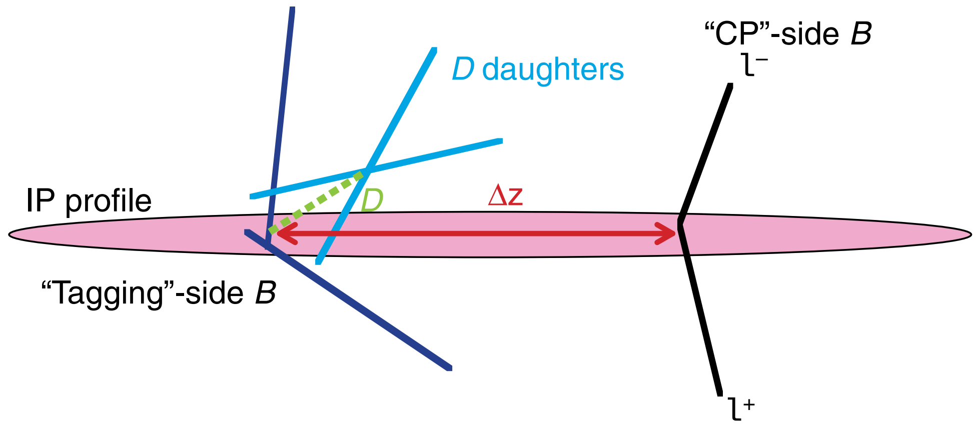

Figure 4.15: *Vertex reconstruction*

in at least one layer and with two or more z hits in total. The IP profile is calculated offline for every accelerator fill using hadronic events. The typical size of the IP profile is 100μm in x, 5μm in y and 3000μm in z. Because of the flat nature of the beam profile, the size in y is determined from the average luminosity, the beam current and the width of the measured vertex distribution in the x-coordinate. The efficiency of the vertex reconstruction is estimated to be 96% with $B^{\pm} \to J/\psi K^{\pm}$ and $B^0 \to J/\psi K^*(\to K^{\pm}\pi^{\mp})$ events. This is consistent with the expectation from SVD acceptance and cluster matching efficiency. The resolution estimated with MC is typically 40μm and small enough to meet the requirement of the Δz resolution of $\sim$ 100μm.

The mass constrained fit for J/ψ is performed after vertex reconstruction of J/ψ[3] (*i.e.* B_{CP} vertex).

4.7.2 Vertex reconstruction of B_{tag}

The algorithm for tagging-side vertex reconstruction was carefully chosen to minimize the effect of long-lived particles, secondary vertices from charmed hadrons and a small fraction of poorly-reconstructed tracks. Among charged tracks remaining after the B_{CP} reconstruction, we use tracks with SVD hits (the same condition as that for the CP-side) with impact parameter (from the IP center) less than 1mm in the r-ϕ plane, and less than 2mm (from the B_{CP} vertex) in z. Tracks are also removed if they form a K_S candidate satisfying the K_S selection criteria and $|M_{K_S} - M_{\pi^+\pi^-}| < 15\text{MeV}/c^2$. Then remaining tracks and the IP constraint are used to reconstruct the tagging-side vertex. If the reduced χ^2 of the vertex is less than 20, we take this vertex. Otherwise we remove the track that gives the largest contribution to the χ^2 of the vertex and do the vertex reconstruction again. In case such a track is a lepton used to tag the flavor of the event, however, we keep the lepton and remove the track with the second worst χ^2. This trimming procedure is continued until we obtain sufficiently small χ^2/ndf of the vertex. If the number of

[3]If the mass constrained fit and vertex fit were performed simultaneously, z position of J/ψ vertex would be biased because we did not take into account all the bremsstrahlung gammas from the leptons.

remaining tracks becomes one, we impose a tighter requirement to ensure the quality of the vertex made with one track and the IP constraint; *i.e.* χ^2/ndf less than 6 and the momentum of the track greater than 0.6GeV/c. The reconstruction efficiency was measured to be 96% with $B^\pm \to J/\psi K^\pm$ and $B^0 \to J/\psi K^*(\to K^\pm\pi^\mp)$ events.

4.7.3 Δz resolution

The overall Δz resolution was measured with $B \to D^* l\nu$ sample. The proper time distribution was fit with the unbinned maximum likelihood method where the B meson lifetime was fixed to be the world average to extract the resolution. Although the "CP-side" is replaced by $D^* l\nu$ which has a different vertex topology, the resolution is expected to be quite similar to that of J/ψ; the difference is about 10% and thus negligible in Δz resolution that is dominated by the tagging-side vertex resolution. Fig.4.16 shows the proper time distribution with the result of the fit. The resolution was estimated to be

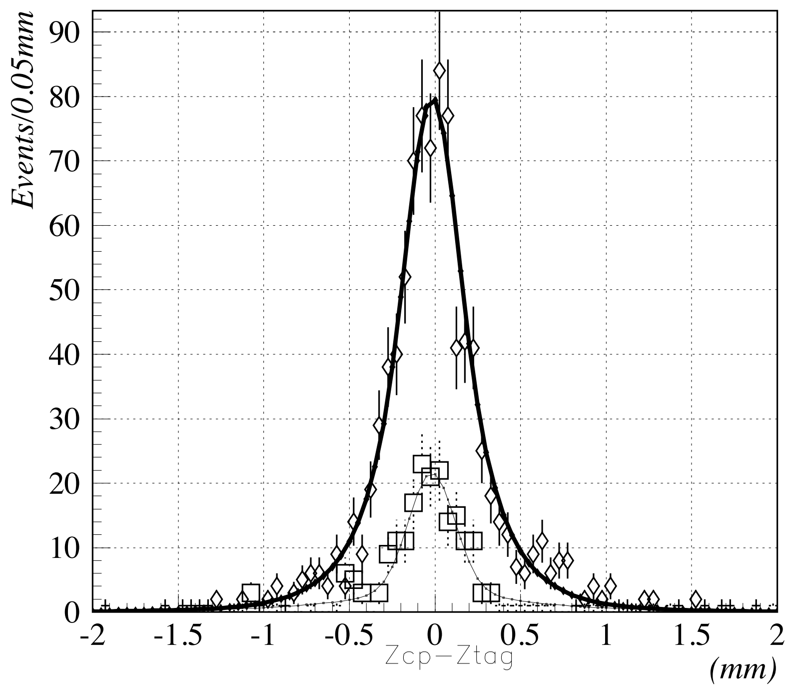

Figure 4.16: *Residual of Δz distribution in $B \to D^*\ell\nu$ sample. The fit is made with two Gaussian functions. Data shown with diamonds are for signal events. Blank squares are for data in the background control sample.*

$\sigma_{sig} = (115^{+24}_{-26})\mu$m with the mean shift of $\mu_{sig} = (-20 \pm 13)\mu$m. We also separated lepton-tagged and kaon-tagged events and checked the resolution function individually. The results are $(\sigma_{sig}, \mu_{sig}) = (120 \pm 50[\mu\text{m}], 10 \pm 33[\mu\text{m}])$ for events tagged with leptons and $(\sigma_{sig}, \mu_{sig}) = (120 \pm 30[\mu\text{m}], -30 \pm 16[\mu\text{m}])$ for events tagged with kaons. These results are consistent with Monte Carlo simulation.

4.8 Summary

We reconstructed $B^0 \to J/\psi K_S^0$, $B^0 \to \psi(2S)K_S^0, \psi(2S) \to \ell^+\ell^-$, $B^0 \to \psi(2S)K_s^0, \psi(2S) \to J/\psi\pi^+\pi^-$, and $B^0 \to \chi_{c1}K_S^0$ decay modes. The numbers of signal (background) events are, 70(3.4), 5(0.2), 8(0.6), and 5(0.75). We performed flavor tagging and vertex reconstruction for these events. The result is summarized in Table 4.9. In Chapter 5, $\sin 2\phi_1$ was extracted using these 50 events.

Decay mode	signal events	Flavor tagging					Background fraction
		high p_ℓ^*	$K^\pm$	med. p_ℓ^*	slow $\pi^\pm$	total	
$B^0 \to J/\psi K_S^0$	70	10	19	2	9	40	0.050±0.025
$B^0 \to \psi(2s)(\ell^+\ell^-)K_S^0$	5	0	0	0	2	2	0.04
$B^0 \to \psi(2s)(J/\psi\pi^+\pi^-)K_S^0$	8	1	2	0	1	4	0.075
$B^0 \to \chi_{c1}K_S^0$	5	0	3	1	0	4	0.15
total	88	11	24	3	12	50	-

Table 4.9: *Summary of reconstructed $B \to$ charmonium $+ K_S$ events*

Chapter 5

Measurement of $\sin 2\phi_1$

In this chapter, we extract the parameter $\sin 2\phi_1$ using 50 $B \to$ charmonium$+ K_S$ sample selected in the previous chapter.

In Section 5.1, we will explain proper time distribution taking detector effects into account. Before we gave the fitting result, we performed systematic check using decay modes with null intrinsic asymmetry. We will show these results in Section 5.2. Then, we extract $\sin 2\phi_1$ in Section 5.3 and we estimate systematic errors in Section 5.4.

5.1 Method to extract $\sin 2\phi_1$

The parameter of CP asymmetry, $\sin 2\phi_1$, is obtained with unbinned maximum likelihood method. The probability density function (PDF) is made from the proper time distribution.

The proper time distribution of B decays is

$$\frac{1}{2\tau_B} e^{-\frac{|\Delta t|}{\tau_B}} (1 \pm (1 - 2w_{tag}) \sin 2\phi_1 \cdot \sin \Delta m \Delta t), \tag{5.1}$$

where Δt is the proper time, $\Delta t = \Delta z / c\beta\gamma$, τ_B is the lifetime of B^0, and Δm is the mass difference between two mass eigenstates of B^0, defined as the equation (2.8). Since the proper time is measured as the distance of decay vertices of two B mesons, the finite resolution of vertex reconstruction degrades observed CP asymmetry. The asymmetry is also diluted by wrong B-flavor tagging mainly due to imperfection of the detector response. Under the condition of finite Δt resolution and imperfect flavor tagging, PDF is defined as

$$\begin{aligned} F &= (1 - f_{bg}(\Delta E, M_{bc})) \int_{-\infty}^{\infty} g_s(\Delta t - \Delta t') \left\{ \frac{1}{2\tau_B} e^{-\frac{|\Delta t'|}{\tau_B}} (1 \pm (1 - 2w_{tag}) \sin 2\phi_1 \cdot \sin \Delta m \Delta t') \right\} d\Delta t' \\ &\quad + f_{bg}(\Delta E, M_{bc}) F_{bg}(\Delta t), \end{aligned} \tag{5.2}$$

where $f_{bg}(\Delta E, M_{bc})$ is the background fraction, g_s is the resolution function of signal events, w_{tag} is the wrong tagging fraction in flavor tagging of B, and F_{bg} is the proper time distribution of background events.

5.1.1 Resolution function

Resolution of Δt is parameterized as a sum of two Gaussian distributions,

$$\begin{aligned} g_s(\Delta t - \Delta t') &= p_{main} G(\Delta t - \Delta t'; \mu_{main}, \sigma_{main}) + && (5.3)\\ & (1 - p_{main}) G(\Delta t - \Delta t'; \mu_{tail}, \sigma_{tail}) && (5.4)\\ G(t; \mu, \sigma) &= \frac{1}{\sqrt{2}\sigma} \exp\left(-\frac{(t-\mu)^2}{2\sigma^2}\right). && (5.5) \end{aligned}$$

Widths of two Gaussian functions (σ_{main}, σ_{tail}) are calculated event-by-event from the B_{CP} and B_{tag} vertex errors,

$$\begin{aligned} \sigma_{main} &= S_{main}\, \sigma_{vertex}, \\ \sigma_{tail} &= S_{tail}\, \sigma_{vertex}, \\ \sigma_{vertex} &= \sqrt{\sigma_{CP}^2 + \sigma_{tag}^2}, \end{aligned}$$

where $\sigma_{CP}, \sigma_{tag}$ are z component of the B_{CP} and B_{tag} vertex errors, respectively. Errors of vertex reconstruction are not enough to explain resolution of Δt because tracks were missreconstructed for several reasons (the error of the B_{tag} vertex did not correctly estimated by tracks from long lived particles, and so on). Therefore we derive scaling factor S_{main}, S_{tail} to correct that effect.

Those parameters of two Gaussian functions are determined using $B \to D^*\ell\nu$ events. The reconstruction of $B \to D^*\ell\nu$ sample is described in Appendix A. Data sample is the same as that used to estimate the wrong tagging fraction of flavor tagging. We assumed that the resolution function for $B \to D^*\ell\nu$ is similar to that for $B \to \text{charmonium} + K_S$. This difference is estimated using MC, and included in systematic error.

5.1.2 Background estimation

Proper time distribution for background was defined as the follows,

$$\begin{aligned} F_{bg}(\Delta t) &= \int_{-\infty}^{\infty} g_{bg}(\Delta t - \Delta t') \left[(1 - f_{prompt}) \frac{1}{2\tau_{bg}} e^{-\frac{|\Delta t'|}{\tau_{bg}}} + f_{prompt}\delta(\Delta t')\right] d\Delta t' && (5.6)\\ g_{bg}(t) &= G(t; \mu^{bg}, \sigma^{bg}) && (5.7)\\ \sigma^{bg} &= S^{bg} \sigma_{vertex}, \end{aligned}$$

where f_{prompt} is the fraction of the prompt background from the continuum events.

Parameters of this background shape are determined from the sideband region of $B^\pm \to J/\psi K^\pm$ and $B^0 \to J/\psi K_S$. The sideband region was defined as

$$\begin{aligned} (-0.1 < \Delta E < 0.4) \cap (5.13 < M_{bc} < 5.29) \cap \overline{(\text{signal region})}, \text{ for } J/\psi K^\pm && (5.8)\\ (-0.04 < \Delta E < 0.4) \cap (5.13 < M_{bc} < 5.29) \cap \overline{(\text{signal region})}, \text{ for } J/\psi K_S. && (5.9) \end{aligned}$$

The number of remaining events is 232 ($J/\psi K_S$: 54 events, $J/\psi K^\pm$: 178 events). Results from fitting using these events are shown in Table 5.1 and in Figure 5.1.

Table 5.1: *Parameters of background shape function*

τ_{bg}	$1.843^{+0.286}_{-0.224}(ps)$
μ^{bg}	$3.00^{+9.94}_{-10.12}(\mu m)$
S^{bg}	$0.836^{+0.153}_{-0.151}$
f_{prompt}	$0.431^{+0.110}_{-0.115}$

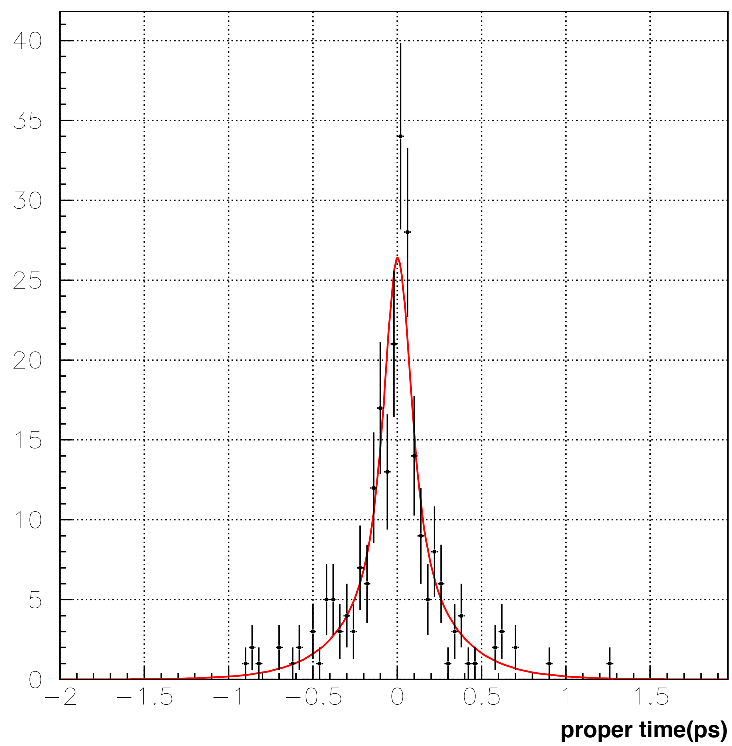

Figure 5.1: *Fitting result of the background shape using the sideband of $J/\psi K^{\pm}$ and $J/\psi K_S$.*

5.1.3 Background fraction f_{bg}

Background fraction, f_{bg}, is calculated based on ΔE and M_{bc} for each event.

Parameters of f_{bg} is derived from the data and the MC:

$$f_{bg}(\Delta E, M_{bc}) = \frac{F_{BG}(\Delta E, M_{bc})}{F_{BG}(\Delta E, M_{bc}) + F_{SIG}(\Delta E, M_{bc})},$$

where $F_{SIG}(\Delta E, M_{bc})$ is the signal probability as the function of ΔE and M_{bc}, and $F_{BG}(\Delta E, M_{bc})$ is the background probability.

In calculation of background fraction for $B^0 \to J/\psi K_S$, distributions of ΔE and M_{bc} for signal are fit with single Gaussian. For the background, distributions of ΔE and M_{bc} are fit with the flat function and the ARGUS background function[62].

$$\begin{aligned} F_{SIG}(\Delta E, M_{bc}) &= a \cdot G(\Delta E; \mu_{\Delta E}, \sigma_{\Delta E}) \cdot G(M_{bc}; \mu_{M_{bc}}, \sigma_{M_{bc}}), \\ F_{BG}(\Delta E, M_{bc}) &= b \cdot M_{bc}\sqrt{1-(2M_{bc}/\sqrt{s})^2}\,\exp(1-(2M_{bc}/\sqrt{s})^2), \end{aligned}$$

where a and b are normalization factors determined such that the integration in the signal box is consistent to the value listed in Table 4.9. The value $\sigma_{M_{bc}}$ was determined from MC data, $\mu_{\Delta E}$ and $\sigma_{\Delta E}$ were determined from real data, and $\mu_{M_{bc}}$ was fixed to the nominal B mass ($(5.2794 \pm 0.0005)\mathrm{GeV}/c^2$). Figures 5.2 show fit result from MC and real data.

ΔE and M_{bc} distributions for $B^0 \to \psi(2S)K_S(\psi(2S) \to \ell^+\ell^-)$ are quite similar to those for $B^0 \to J/\psi K_S$ because of the almost identical event topology. Therefore $\sigma_{M_{bc}}$, $\mu_{M_{bc}}$, and $\sigma_{\Delta E}$ were determined from the fit result with $B^0 \to J/\psi K_S$. However a and b are determined from the integrated background fraction of the $B^0 \to \psi(2S)K_S$ decay.

For $B^0 \to \psi(2S)K_S(\psi(2S) \to J/\psi\pi^+\pi^-)$ and $B^0 \to \chi_{c1}K_S$, calculation procedure is the same as that for $B^0 \to J/\psi K_S$ except the difference of the ΔE function. Since it is hard to reconstruct π from $\psi(2S)$ and γ from χ_{c1}, ΔE distributions for these decay modes are not expressed with the Gaussian function. Therefore ΔE distributions are fit with the Crystal Ball function[63]:

$$(\text{Crystal Ball function}) = \begin{cases} \frac{1}{\mathrm{A}}\exp\left(-\frac{(\Delta E-\mu_{\Delta E})^2}{2\sigma_{\Delta E}^2}\right) & \text{for } \Delta E > \mu_{\Delta E} - \alpha\sigma_{\Delta E} \\ \frac{1}{\mathrm{A}}\frac{\exp\left(-\alpha^2/2\right)}{\left[1-\frac{(\Delta E-\mu_{\Delta E})\alpha}{\sigma_{\Delta E}\alpha}-\frac{\alpha^2}{n}\right]^n} & \text{for } \Delta E < \mu_{\Delta E} - \alpha\sigma_{\Delta E}. \end{cases}$$

All parameters were determined from MC because the number of events for these modes are too small to estimate the parameters. The fit results from MC and real data are shown in Appendix B.

5.1.4 Likelihood function

An unbinned maximum likelihood method is used to extract $\sin 2\phi_1$. The likelihood function is defined as

$$L = \prod_i F_{CP}(\Delta t_i; \sin 2\phi_1),$$

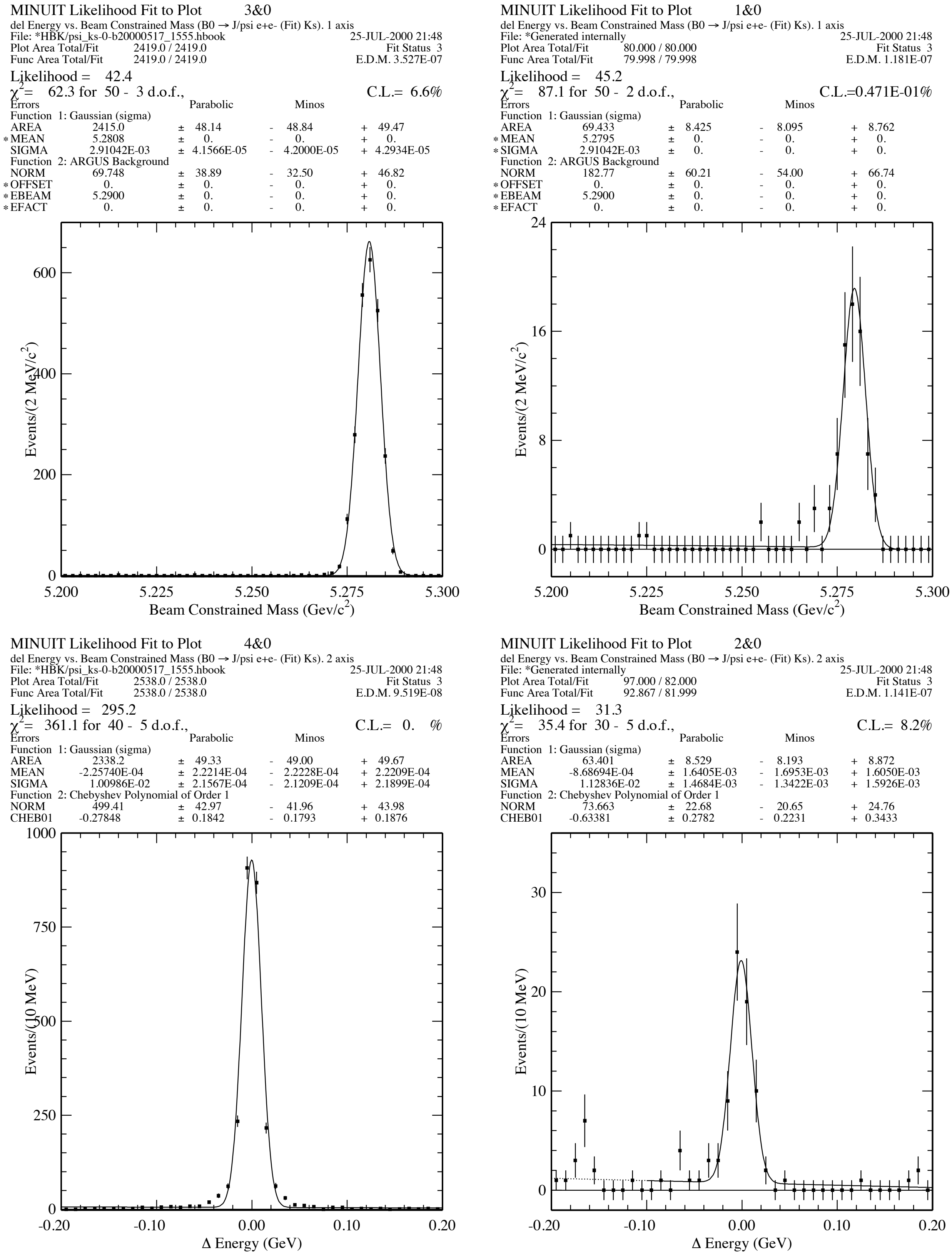

Figure 5.2: *Result from fitting ΔE and M_{bc} distributions for $B^0 \to J/\psi K_S$. Top-left figure shows M_{bc} distribution from MC and Top-right figure shows M_{bc} distribution from real data. Bottom-left figure shows ΔE distribution from MC and bottom-right figure shows ΔE distribution from real data.*

where F_{CP} is the PDF for $B \to \text{charmonium} + K_S$ events.

Since it is difficult to estimate systematic errors from resolution function, we estimated $\sin 2\phi_1$ and parameters of the resolution function simultaneously. Then the likelihood function is modified;

$$L = \prod_i F_{CP}(\Delta t_i; \sin 2\phi_1) \times \prod_j F_{noCP}(\Delta t_j; 0.). \tag{5.10}$$

where F_{noCP} is the PDF for $B \to D^* \ell \nu$ with null intrinsic asymmetry.

This extraction method is called "CP-fit" hereafter.

5.2 Validating checks

5.2.1 Tests on control samples

A control sample of $B^\pm \to J/\psi K^\pm$ and $B^0 \to J/\psi K^{*0}$ was analyzed in order to verify the proper time reconstruction, tagging algorithm and likelihood fitting procedures.

Reconstruction of $B^\pm \to J/\psi K^\pm$ and $B^0 \to J/\psi K^{*0}$

Reconstruction of J/ψ is the same as that of $B \to \text{charmonium} + K_S$. The criteria were described in Section 4.4.1. Charged kaons are identified by requiring that the likelihood ratio of kaon to pion is greater than 0.4.

The K^{*0} candidates are reconstructed by looking at the decay mode $K^{*0} \to K^+\pi^-$ and its charge conjugate. K^{*0} is identified if the difference of the invariant mass of an kaon-pion pair is within 75MeV/c^2 of the nominal K^{*0} mass.

Figure 5.3 shows the scatter plot of M_{bc} and ΔE together with the projections onto each axis. B candidates are selected by requiring $|M_{bc} - M_{B^0}| < 0.01$GeV/c^2 and $|\Delta E| <$ 0.04GeV. For the remaining candidates, we performed vertex reconstruction with the same methods as $B \to \text{charmonium} + K_S$. The numbers of $J/\psi K^\pm$ and $J/\psi K^{*0}$ candidates are 275 and 99, and background fractions are 0.012 and 0.047, respectively.

Measurement of lifetime

We measured lifetime of B^0 and $B^\pm$ with these control samples to demonstrate the validity of the resolution function. Likelihood function is the same as the equation (5.10) except that no CP asymmetry was introduced and treated the lifetime as a free parameter. Results are $\tau_{B^\pm} = 1.86^{+0.15}_{-0.14}(ps)$ and $\tau_{B^0} = 1.54^{+0.22}_{-0.20}(ps)$ for $B^\pm \to J/\psi K^\pm$ and $B^0 \to J/\psi K^{*0}$, respectively. These are consistent with the PDG values. Figure 5.4 shows the fit results.

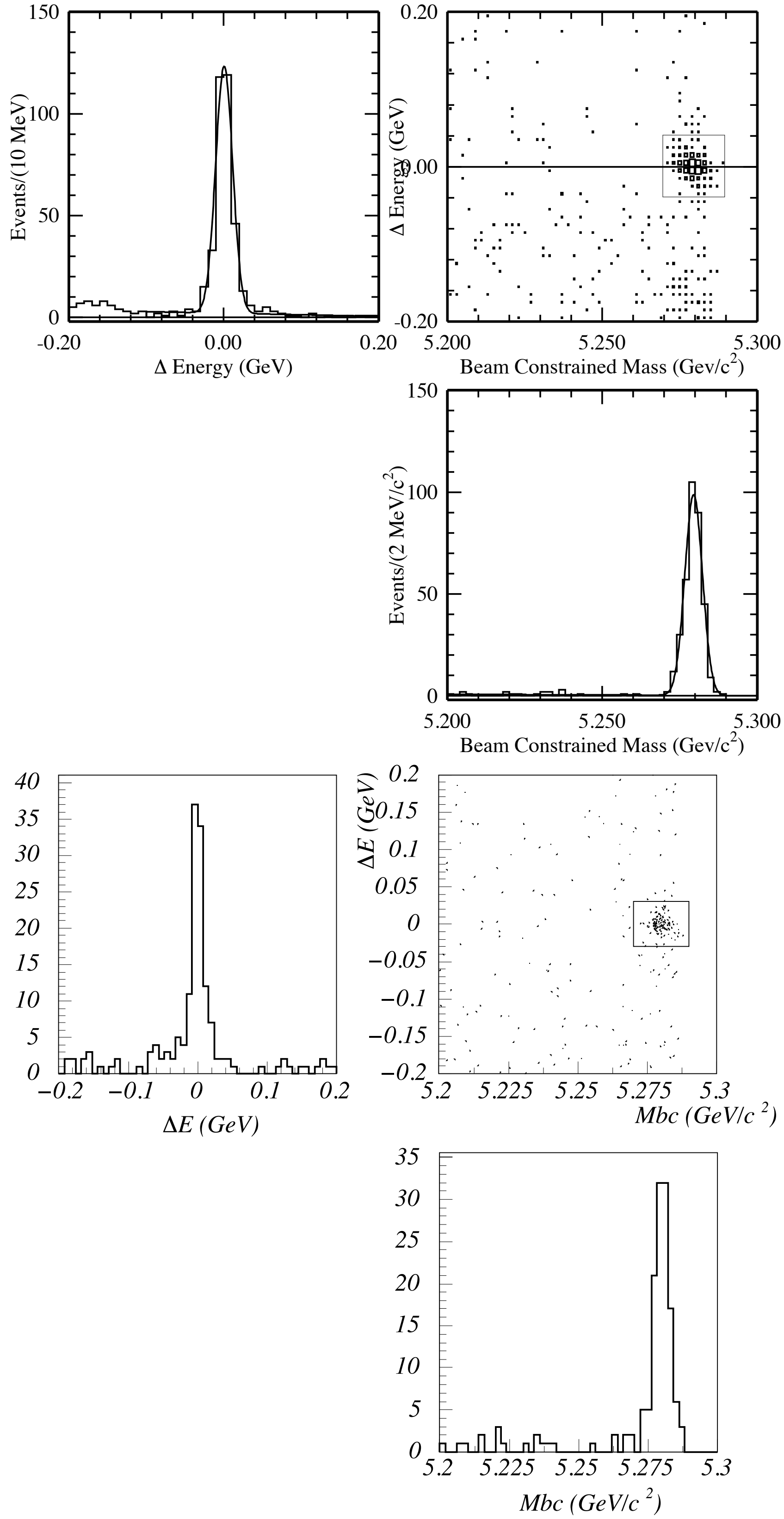

Figure 5.3: *The scatter plots of* ΔE *versus* M_{bc} *for* $B^{\pm} \rightarrow J/\psi K^{\pm}$ *and* $B^0 \rightarrow J/\psi K^{*0}$. *The upper figure shows the scatter plot for* $B^{\pm} \rightarrow J/\psi K^{\pm}$ *and lower figure shows that for* $B^0 \rightarrow J/\psi K^{*0}$.

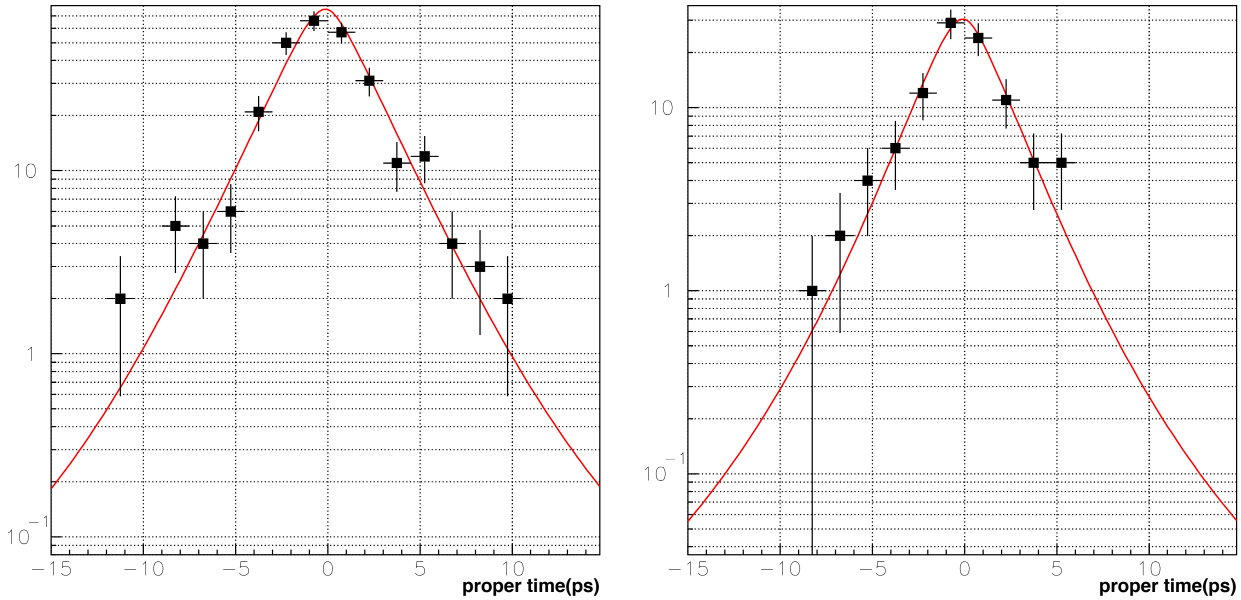

Figure 5.4: *Lifetime fit results. Left figure shows fitting result for $B^\pm \to J/\psi K^\pm$ and right figure shows that for $B^0 \to J/\psi K^{*0}$.*

CP-fit for control-sample

We also performed CP-fit to 139 $J/\psi K^\pm$ events and 53 $J/\psi K^{*0}$ events which remained after the flavor tagging. Results of the fit are as follows,

$$\begin{aligned}\text{(asymmetry parameter)} = \quad & 0.27^{+0.27}_{-0.28} \qquad (J/\psi K^\pm) \\ & -0.03^{+0.50}_{-0.48} \qquad (J/\psi K^{*0}).\end{aligned}$$

These results are also shown in Figure 5.5 and 5.6.

Thus each asymmetry parameter of $B^\pm \to J/\psi K^\pm$ and $B^0 \to J/\psi K^{*0}$ is consistent with zero, indicating that we do not have considerable bias in the CP-fit.

5.2.2 Ensemble test

As a check of the fitting procedure, about 900 sets of toy Monte Carlo data samples, each containing 50 $B \to$ charmonium $+ K_S$ and 2071 $B \to D^*\ell\nu$ events, were generated based on the PDF described in the previous sections. Figure 5.7 shows the distribution of the pull $(\frac{sin2\phi_1 - 0.5}{\sigma})$, and the errors of $\sin 2\phi_1$. From these figures, we conclude that the fit procedure provides the correct and unbiased error estimation.

5.3 Fitting result

We used the likelihood function already defined as Equation 5.10. The best value for $\sin 2\phi_1$ is found by scanning over $\sin 2\phi_1$ to minimize the $\ln(L)$.

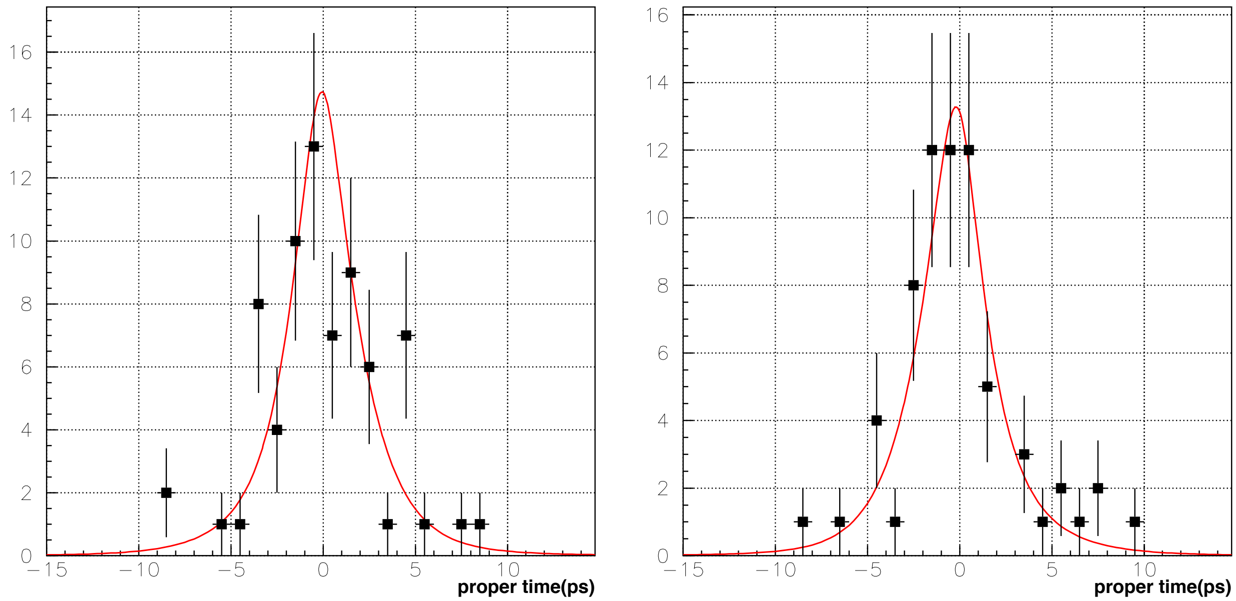

Figure 5.5: Δt distribution for $B^{\pm} \to J/\psi K^{\pm}$. Left figure shows distribution for $B_{tag} = B^{-}$ and right figure shows that for $B_{tag} = B^{+}$.

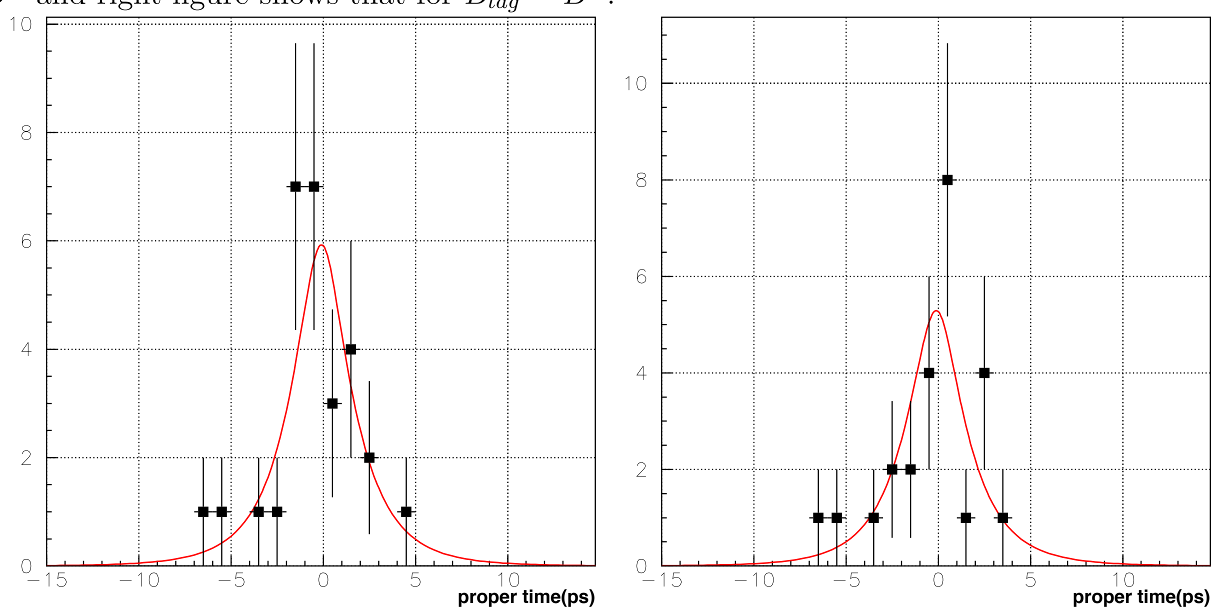

Figure 5.6: Δt distribution for $B^0 \to J/\psi K^{*0}$. Left figure shows distribution for $B_{tag} = B^0$ and right figure shows that for $B_{tag} = \bar{B}^0$.

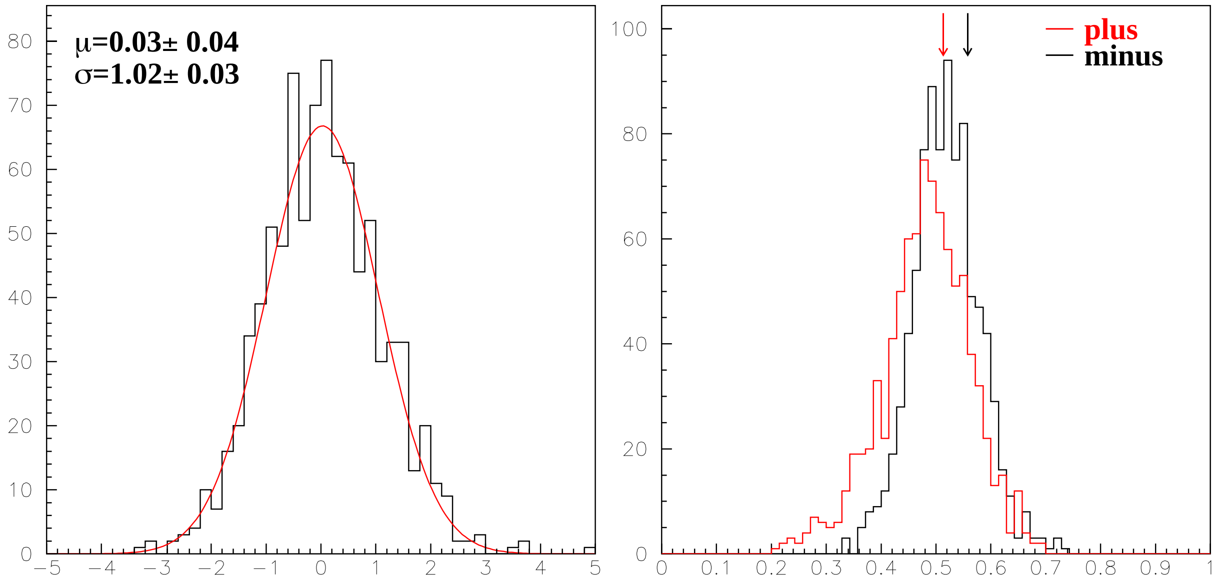

Figure 5.7: *Result of toy Monte Carlo experiments generated for* $\sin 2\phi_1$*=0.5. Left figure shows* $(\frac{sin2\phi_1 - 0.5}{\sigma})$ *distribution and right figure shows distributions for the errors of the positive and negative sides. Two arrows written in the right figure are errors of the fit using real data.*

By using 50 charmonium + K_S events and 2071 $D^*\ell\nu$ events, we obtain

$$\sin 2\phi_1 \quad = \quad 0.58^{+0.51}_{-0.56}(fit),$$

and the other parameters which we simultaneously obtain the CP-fit is shown in Table 5.2. The average shape of the resolution function of signal was drawn by summing event-by-event resolution functions over 275 $J/\psi K^{\pm}$ events in the real data (Figure 5.8). The resolution of this resolution function is 111μm when we perform the fit with Gaussian function. When the sum of two Gaussian functions were used, the sigma of main Gaussian function is 98μm, the sigma of minor that is 371μm, and the fraction of main part is 0.85.

Figure 5.9 shows proper time distributions of $B \to$ charmonium + K_S, Figure 5.10 shows the log-likelihood value as a function of $\sin 2\phi_1$, and Figure 5.11 shows the corrected time evolution of asymmetry.

We also performed the CP-fit with 40 $J/\psi K_S$ samples;

$$\sin 2\phi_1 \quad = \quad 0.22^{+0.59}_{-0.60}(fit)\ (J/\psi K_S)$$

Fit results are shown in Figure 5.12.

signal shape	μ_{main}	$(-15.4 \pm 9.4)\ \mu m$
	S_{main}	1.10 ± 0.11
	f_{main}	$0.948^{+0.020}_{-0.030}$
	μ_{tail}	$(15.5^{+216.4}_{-165.6})\ \mu m$
	σ_{tail}	$6.86^{+1.61}_{-1.47}$
background shape (successful in flavor tagging)	τ_{bg}	$(1.69^{+0.36}_{-0.25})\ ps$
	μ_{bg}	$(-23.0^{+18.7}_{-18.6})\ \mu m$
	S_{bg}	$1.45^{+0.33}_{-0.41}$
	f_{prompt}	$0.225^{+0.264}_{-0.225}$
background shape (failed in flavor tagging)	τ_{bg}	$(2.03^{+0.71}_{-0.41})\ ps$
	μ_{bg}	$(-113.6^{+14.8}_{-14.7})\ \mu m$
	S_{bg}	$1.22^{+0.20}_{-0.19}$
	f_{prompt}	$0.576^{+0.160}_{-0.179}$

Table 5.2: *Parameters of resolution functions for signal and background obtained the CP-fit for $B \to charmonium + K_S$.*

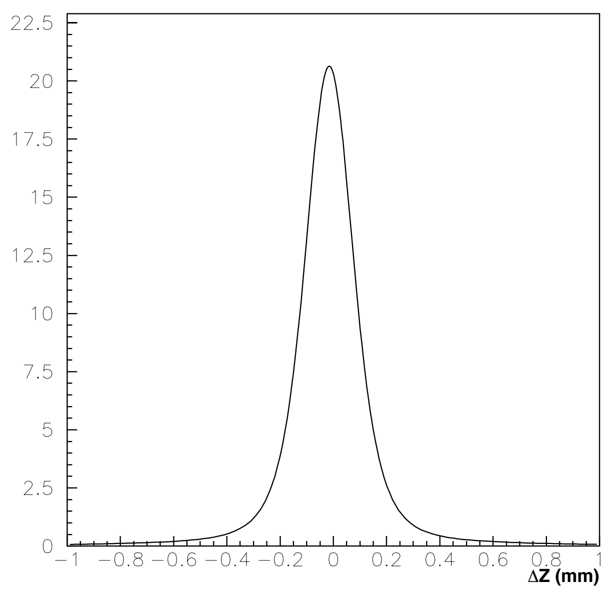

Figure 5.8: *The resolution function of $J/\psi K^{\pm}$ using the real data.*

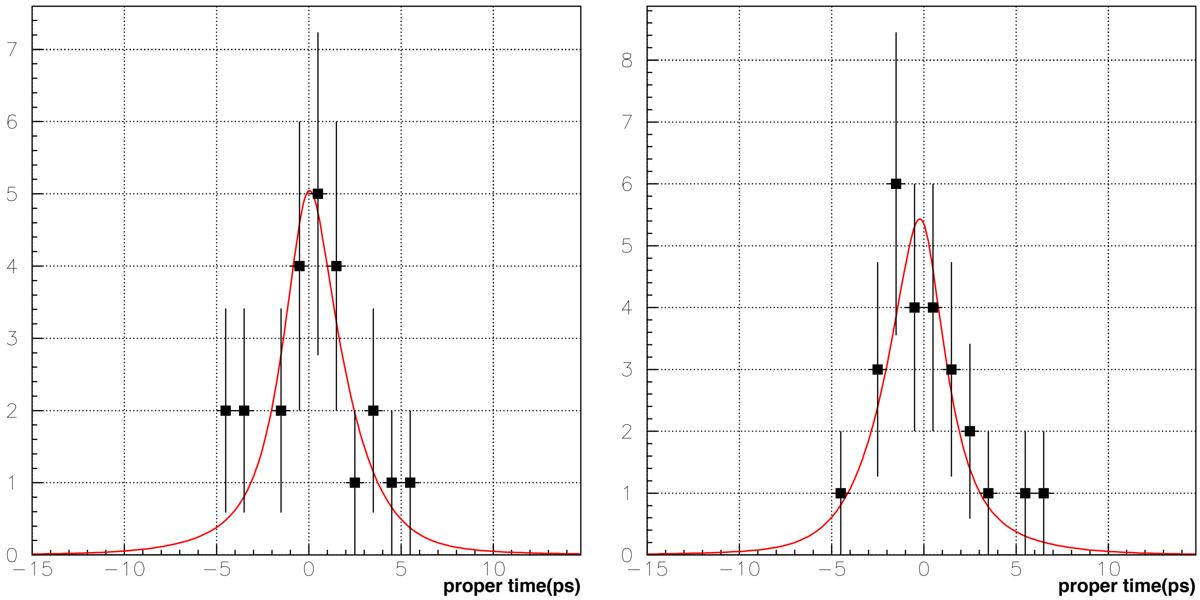

Figure 5.9: *Δt distribution for $B \to$ charmonium$+ K_S$. Left figure shows distribution for $B_{tag} = B^0$ and right figure shows that for $B_{tag} = \bar{B}^0$*

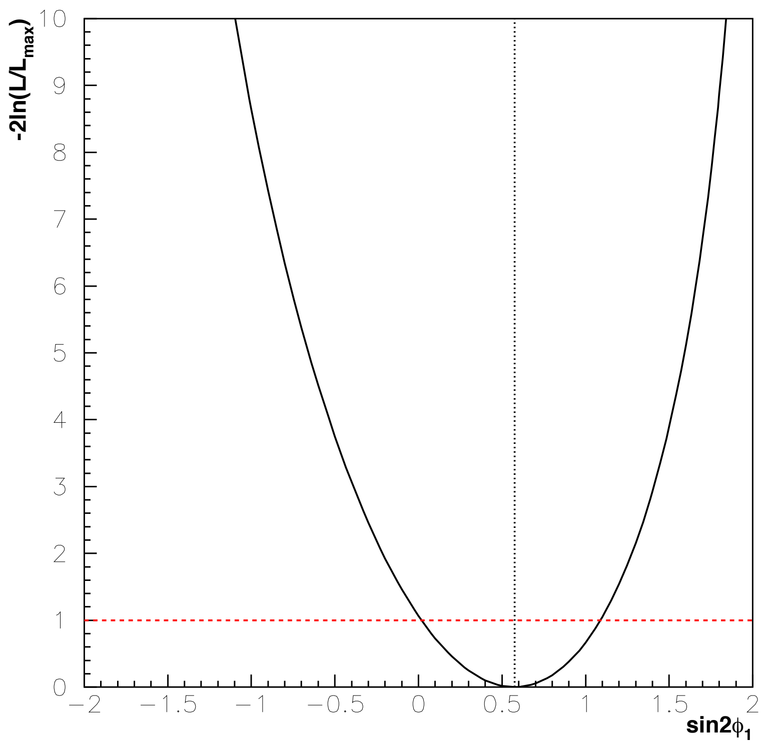

Figure 5.10: *Log-likelihood as a function of* $\sin 2\phi_1$.

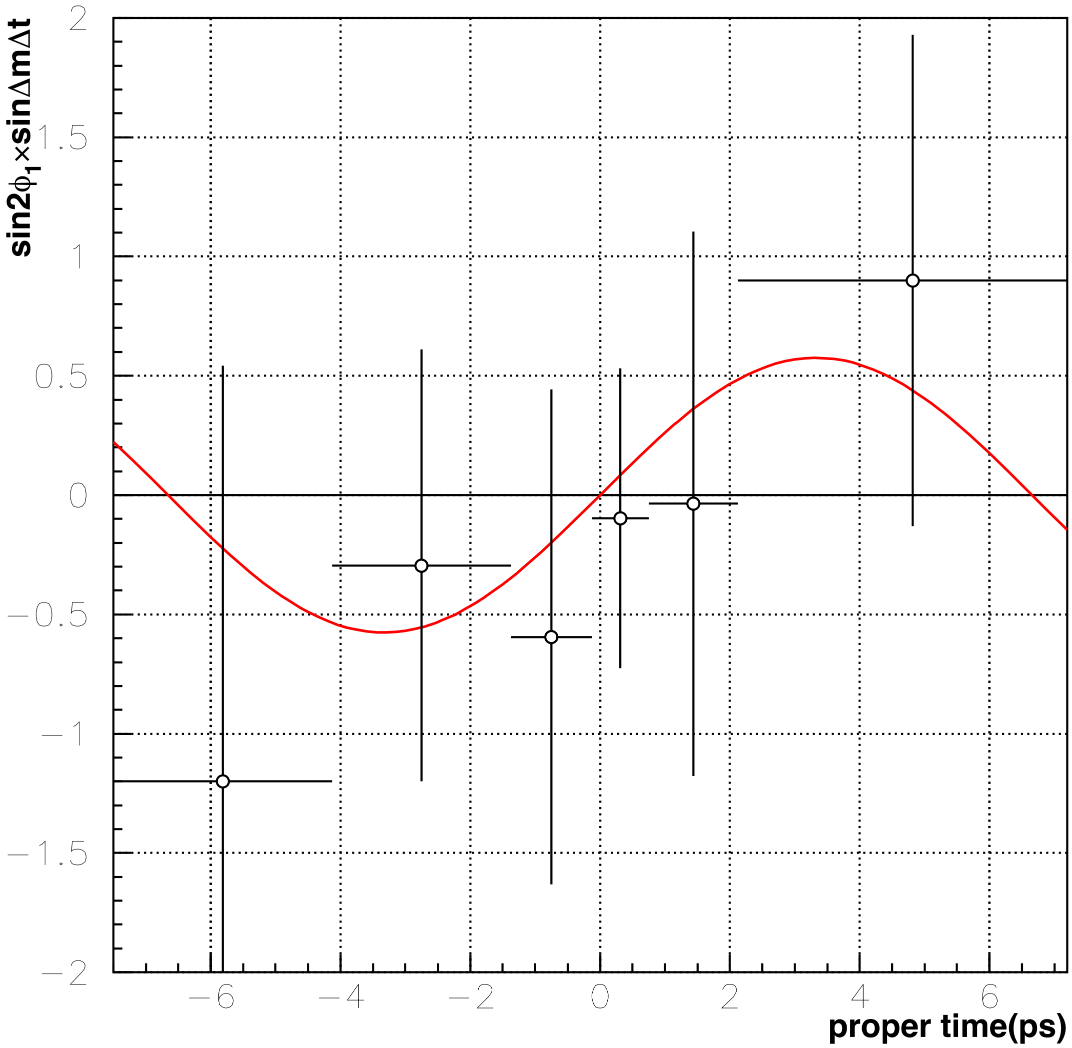

Figure 5.11: *Reconstructed asymmetry versus proper time, after correction for the average dilution in each bin.*

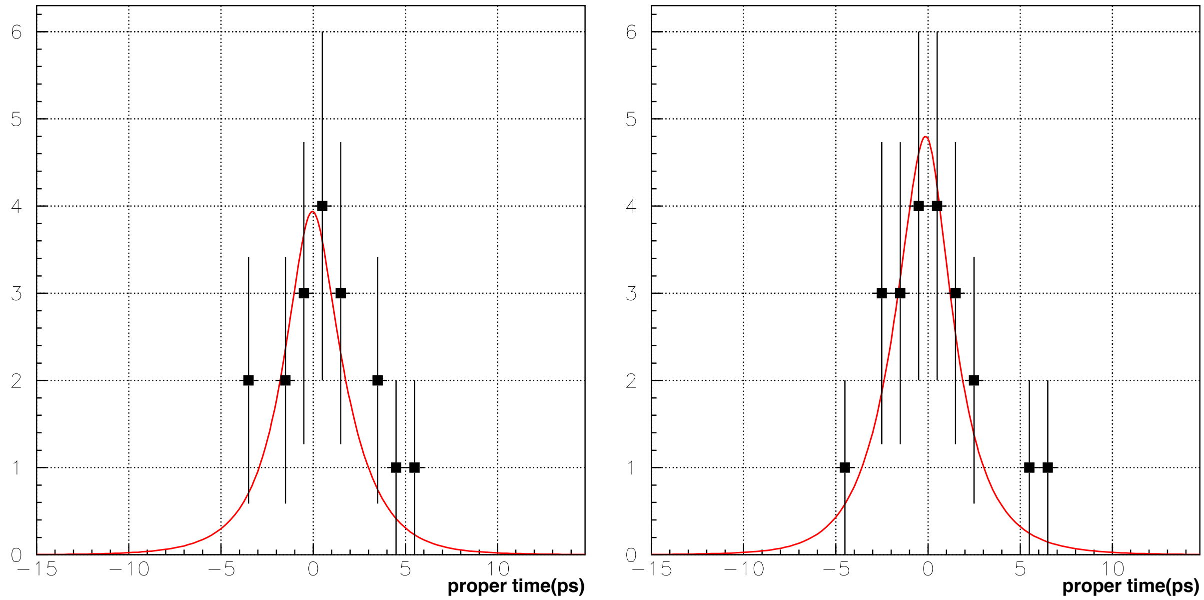

Figure 5.12: Δt *distribution for* $B^0 \to J/\psi K_S$. *Left figure shows distribution for* $B_{tag} = B^0$ *and right figure shows that for* $B_{tag} = \bar{B}^0$

5.4 Systematic errors

5.4.1 Physics parameters

The world average value of the B meson lifetime is [19]

$$\tau_B = (1.548 \pm 0.032) \times 10^{-12} sec. \tag{5.11}$$

We estimated the systematic error from B lifetime by varying the lifetime of B meson within the error shown above.

The effect of B^0-$\bar{B}^0$mixing parameter, Δm, was also estimated with the same method. The world average value is

$$\Delta m = (0.472 \pm 0.017) \times 10^{12}\ \hbar s^{-1}. \tag{5.12}$$

5.4.2 Wrong tagging fraction of flavor tagging w_{tag}

The error for each flavor tagging method is listed in Table 4.8. These errors were studied by varying wrong tagging fraction individually for each method, and we added them in quadrature.

5.4.3 Resolution function of signal

In the proper-time fitting procedure, we assumed that the resolution function of charmonium+ K_S is the same as that of $D^*\ell\nu$. We checked the validity of this assumption using Monte

Carlo simulation. From generator information, we can obtain the difference between two B decay points perfectly. A residual of Δt, $\delta(\Delta t)$, is defined as the follows:

$$\delta(\Delta t) \equiv (\Delta t \text{ from reconstruction}) - (\Delta t \text{ from generator information}).$$

Since $\delta(\Delta t)$ expresses the uncertainty of reconstruction of Δt, parameters in the resolution function (5.4) are able to be given by fitting with $\delta(\Delta t)$ and event-by-event errors. The method is described as follows:

- For easier comparison, parameters of the resolution function except S_{main} are obtained from $J/\psi K_S$ MC and are fixed.
- The residual of Δt is fitted in the function defined as (5.4) for each $D^*\ell\nu$ decay mode.

The result from Monte Carlo indicates these shapes are slightly different, We defined "the rescale factor" as follows,

$$\begin{aligned} S_{main}(\text{successful in flavor tagging}) &= 1.017 \times S_{main}(J/\psi K_S), \\ S_{main}(\text{failed in flavor tagging}) &= 1.009 \times S_{main}(J/\psi K_S), \end{aligned}$$

and performed the CP-fit. The values of rescaling factors for each mode are given by the MC results. The difference of $\sin 2\phi_1$ between fit with and without rescaling factor is -0.003. We decided that this difference is too small to introduce to CP-fit. Therefore this difference is included as a systematic error by $+0.000, -0.003$. A systematic error for μ_{main} was estimated with the same method as that for S_{main} and we obtain $+0.003, -0.000$.

The resolution function includes the uncertainty of background fractions of $D^*\ell\nu$ which was listed in Table A.2. The systematic errors for this uncertainty were studied varying the background fractions of $D^*\ell\nu$, and we obtain $+0.004, -0.003$.

Since $\sin 2\phi_1$ and signal shape are fitted simultaneously, the systematic error except that effect was included in the error of the CP-fitting.

5.4.4 Resolution function of background

Errors of resolution function of background are shown in Table 5.1. We varied these parameters within the errors independently, and added them in quadrature.

5.4.5 Background fraction in PDF, $f_{bg}(\Delta t, M_{bc})$

Background fraction of PDF, f_{bg}, is calculated with distribution functions of ΔE, M_{bc} and the integrated background fractions as we described in Section 5.1.3. The distribution functions of ΔE and beam constrained mass are defined from real data and MC[1].

[1] $\mu_{\Delta E}, \sigma_{M_{\Delta E}}$ for $J/\psi K_S$ and $\psi(2S)K_S(\psi(2S) \to \ell^+\ell^-)$ were estimated based on the real data and the other parameters were obtained from the MC data.

To estimate systematic errors associated with the choice of parameterization, we varied the parameters obtained from the MC data by $\pm 2\sigma$ and the parameters obtained from the real data by $\pm 1\sigma$, and CP-fit was repeated. A wider range of the uncertainty was conservatively chosen for parameters obtained from the MC data, taking into account the possible difference between the MC and real data.

We estimated systematic errors for the integrated background fractions, written in Table 4.9, varying these parameters by $\pm 1\sigma$ for $B^0 \to J/\psi K_S$ decay mode and by $\pm 1\times$(integrated background fraction) for the other decay modes. After the above calculation for each decay mode, we added them in quadrature.

5.4.6 B flight length

The IP constrained fit includes the uncertainty of the B decay point due to B flight length in the r-ϕ plane. The uncertainty is estimated to be $\sim 20\mu m$ assuming a Gaussian function. The uncertainty was varied by $\pm 10\mu m$ and we repeated the analysis to estimate the error.

5.4.7 IP drift during an accelerator fill

We know that IP could move up to about $\pm 2mm$ along the Z axis during a run. Since we fixed the IP position in each accelerator fill, the IP constrained fit includes the uncertainty of the IP drift. We estimated systematic errors varying the Z position of IP by $\pm 2mm$ and repeating the analysis.

5.4.8 Asymmetry parameter of background

We assume that proper time distribution of background has no asymmetry, although some small asymmetry should be allowed in reality. Therefore we estimate systematic errors for this effect varying asymmetry parameter of background by ± 0.3 ($\sim$ asymmetry for $J/\psi K^{\pm}$).

5.4.9 Vertex reconstruction using one track and the IP for tagging-side

We use the IP constraint for vertex reconstruction of B_{CP} and B_{tag}. In case that there is only 1 track available and $\sigma_{tag} > 200\mu m$, reconstructed vertex is pulled to the IP position. We studied this effect using the MC. Then we found that the size of this dependency is about $\pm 100\mu m$. Therefore we estimate systematic errors for this effect varying Δz of the B_{tag} vertex reconstructed using 1 track and the IP by $\pm 100\mu m$ and repeating the analysis.

5.4.10 Summary

Table 5.3 lists systematic errors described above. The largest error is due to uncertainty in the wrong tagging fraction of flavor tagging.

Adding all the systematic errors in quadrature, we finally obtain

$$\sin 2\phi_1 = 0.58^{+0.51}_{-0.56}(stat.)^{+0.10}_{-0.09}(syst.).$$

source	error	
lifetime	+0.012	-0.012
Δm	+0.012	-0.012
wrong tagging fraction	+0.089	-0.082
resolution function of signal	+0.005	-0.005
resolution function of background	+0.002	-0.002
signal fraction	+0.010	-0.010
B flight length	+0.017	-0.011
IP drift	+0.011	-0.014
asymmetry of background	+0.008	-0.007
vertex reconstruction for B_{tag}	+0.033	-0.032
total	+0.100	-0.092

Table 5.3: *List of systematic errors*

5.5 Discussion

The result obtained in the previous sectio is consistent with the region allowed by the other experimental data and the Standard Model. explained in Chapter 2. We have calculated the statistical significance of whether this result supports $\sin 2\phi_1 > 0$ and hence provides indication for CP violation in the B system. Using the Feldman-Cousins method[2], the interval of $0. < \sin 2\phi_1 < 0.92$ corresponds to 69.0% confidence level, while we find that the probability of $\sin 2\phi_1 > 0.$ is 80.4% using the Bayesian method, where we have assumed that a prior distribution is flat in the physically allowed region. Finally, if the true value of $\sin 2\phi_1$ is zero, the probability of obtaining $\sin 2\phi_1 > 0.58$ is 16.1% assuming the Gaussian uncertainty and simply integrating the Gaussian distribution from 0.58 to infinity.

The uncertainly of $\sin 2\phi_1$ is dominated by the statistical contribution. The Belle experiment is expected to accumulate data with an integrated luminosity of about $30 fb^{-1}$ by 2001 summer. By this time, the statistical error will become about 0.25.

The systematic term of the uncertainty of $\sin 2\phi_1$ does not dominate the overall uncertainty of $\sin 2\phi_1$. The main part of the systematic errors is due to the uncertainty of the wrong tagging fraction of the flavor tagging and due to Z dependence in vertex reconstruction of B_{tag} using one track and the IP. As shown in Appendix A, the uncertainty of the wrong tagging fraction is mainly due to the statistical errors of the fraction of opposite-flavor events in all the background. For the B_{tag} vertex, this uncertainty can

[2] The details of the Feldman-Cousins method and Baysian method are described in Appendix C.

be decreased by tightening selection criteria for tracks if necessary. Therefore we will expect that systematic errors will not dominate the uncertainty of $\sin 2\phi_1$ in 2001 summer. With a few years of running, the statistical error will be reduced to be less than 0.1. As we verified that the systematic error is small and the dominant part of the systematic error will be also reduced with the larger statistics, this thesis clearly demonstrates the capability of precision measurement of $\sin 2\phi_1$ at Belle.

Chapter 6

Conclusion

This thesis has described a study of the time-dependent CP asymmetry using the Belle detector. A sample of B mesons obtained with the KEKB asymmetric electron-positron collider operating at the $\Upsilon(4S)$ resonance is used. The analyzed data were taken in June 1999 - July 2000, corresponding to integrated limunosity of 6.2 fb^{-1} on the $\Upsilon(4S)$ resonance and to 6.3×10^6 $B\bar{B}$ pairs.

The neutral B meson is fully reconstructed via its decay into a CP eigenstate: $J/\psi K_S$, $\psi(2S)K_S$, and $\chi_{c1}K_S$. Resolutions of ΔE and beam constrained mass for $J/\psi K_S$ are 11 MeV and 2.9 MeV/c^2, respectively. Background fractions in the signal region are 0.050 ± 0.025 for $J/\psi K_S$, 0.04 for $\psi(2S)K_S$ ($\psi(2S) \to \ell^+\ell^-$), 0.075 for $\psi(2S)K_S$ ($\psi(2S) \to J/\psi\pi^+\pi^-$), and 0.15 for $\chi_{c1}K_S$.

The flavor of the accompanying B meson is identified mainly from the charge of high-momentum leptons or kaons among its decay products. The performance of the flavor tagging was estimated using $B \to D^*\ell\nu$ sample, obtaining the tagging efficiency of 0.510 ± 0.016 and the effective tagging efficiency of $0.19^{+0.04}_{-0.03}$.

Remaining signal candidates of $J/\psi K_S$, $\psi(2S)K_S$ ($\psi(2S) \to \ell^+\ell^-$), $\psi(2S)K_S$ ($\psi(2S) \to J/\psi\pi^+\pi^-$), and $\chi_{c1}K_S$ were 40, 2, 4, and 4 events, respectively.

The time resolution function was measured with sample of fully reconstructed semileptonic neutral B decays. Vertex resolution is estimated to be (115^{+24}_{-26}) μm, which is sufficient for the measurement of time-dependent CP asymmetry.

The time interval between the two decays is determined from the distance between the decay vertices. A maximum likelihood fitting method is used to extract $\sin 2\phi_1$ from the asymmetry in the time interval distribution of 50 $B \to$ charmonium $+ K_S$ events. We obtain

$$\sin 2\phi_1 = 0.58^{+0.51}_{-0.56}(stat.)^{+0.10}_{-0.09}(syst.),$$

whereas the region allowed by the other experimental data and the Standard Model is $0.50 < \sin 2\phi_1 < 0.85$. Therefore our result is consistent with this allowed region.

The uncertainly of $\sin 2\phi_1$ is dominated by the statistical contribution. The Belle experiment is expected to accumulate data with an integrated luminosity of about $30 fb^{-1}$ by 2001 summer. By this time, the statistical error will become about 0.25. We have verified that the systematic error is small and its dominant part will be also reduced with the larger statistics. Thus this thesis clearly demonstrates the capability of precision measurement of $\sin 2\phi_1$ at Belle.

Appendix A

Extraction of wrong tagging fraction

We used $B \to D^*\ell\nu$ decay mode to estimate wrong tagging fraction of flavor tagging, w_{tag} as denoted in Section 4.6. We used the decay chain of $B \to D^*\ell\nu$ $D^{*-} \to \bar{D}^0\pi^-$ $D^0 \to K^-\pi^+$ for this study.

In this appendix, we explain estimation of w_{tag} in detail.

A.1 Reconstruction of $B \to D^*\ell\nu$

We analyzed the data taken in January 2000 -July 2000. The data corresponds to an integrated luminosity of 5.4 fb^{-1} on the $\Upsilon(4S)$ resonance. Hadron event selection is similar to that for $B \to \mathrm{charmonium} + K_S$ event selection which is described in Section 4.1 except that H_2/H_0 cut is not used.

A.1.1 Requirements for tracks

All the tracks used in $D^*\ell\nu$ reconstruction are required to be identified as $e^\pm$, $\mu^\pm$, and $K^\pm$ and have SVD hits with its impact parameter $|dr| < 0.2cm$, except for the slow $\pi^\pm$ ($\pi_s^\pm$) from $D^{*\pm}$.

A.1.2 Reconstruction of $D^0 \to K^-\pi^+$

We reconstruct $D^{*\pm}$ through its decay into $D^0(\bar{D^0})\pi^\pm$ and $D^0(\bar{D^0})$ into $K^\mp\pi^\pm$. Hereafter charge conjugation is implied. Using $K^\mp\pi^\pm$ pair which has an opposite charge to each other, the invariant mass was defined as follows:

$$M_{K\pi}^2 = \left(\sqrt{M_K^2 + |\vec{p}_K|^2} + \sqrt{M_\pi^2 + |\vec{p}_\pi|^2}\right)^2 - |\vec{p}_K + \vec{p}_\pi|^2,$$

where M_K and M_π are the nominal mass for the charged kaon and the charged pion, respectively. D^0 candidates are selected by requiring,

$$1.846 < M_{K\pi} < 1.886 \mathrm{GeV}/c^2.$$

Figure A.1 shows the invariant mass distribution of D^0 candidates.

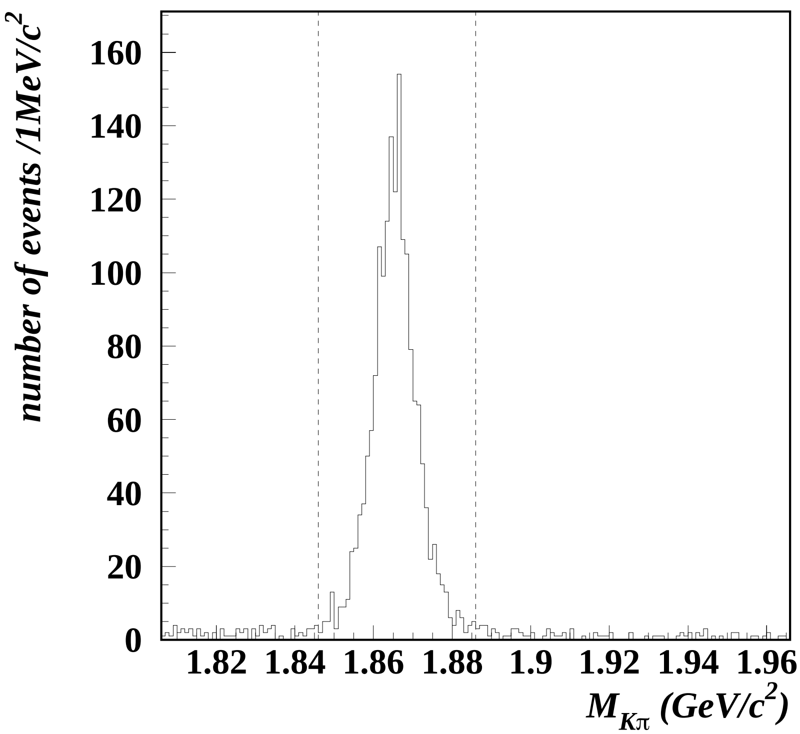

Figure A.1: The invariant mass distributions for $D^0 \to K^-\pi^+$.

A.1.3 Reconstruction of $D^{*\pm} \to D^0\pi_s^\pm$

We combine D^0 candidates with other tracks which have an opposite charge to the kaon in the D^0 candidate. We calculate the invariant mass,

$$M_{K\pi\pi}^2 = \left(\sqrt{M_{K\pi}^2 + |\vec{p}_{K\pi}|^2} + \sqrt{M_{\pi_s}^2 + |\vec{p}_{\pi_s}|^2}\right)^2 - |\vec{p}_{K\pi} + \vec{p}_{\pi_s}|^2 ,$$

where $\vec{p}_{K\pi}$ is vector sum of momenta of the kaon and the pion in the D^0 candidate, $\vec{p}_{\pi_s}$ is the momentum of the attached pion. We required the mass difference, $M_{diff} = M_{K\pi\pi_s} - M_{K\pi}$, to be in a region:

$$0.1434 < M_{diff} < 0.1474(\mathrm{GeV/c^2}).$$

Figure A.2 shows the mass difference distribution. In addition, the $D^{*\pm}$ momentum ($p^*_{D^{*\pm}}$) in the $\Upsilon(4S)$ center-of-mass system (CMS) is required to be $p^*_{D^{*\pm}} < 2.6$ GeV/c so that it is consistent with a daughter particle from B mesons.

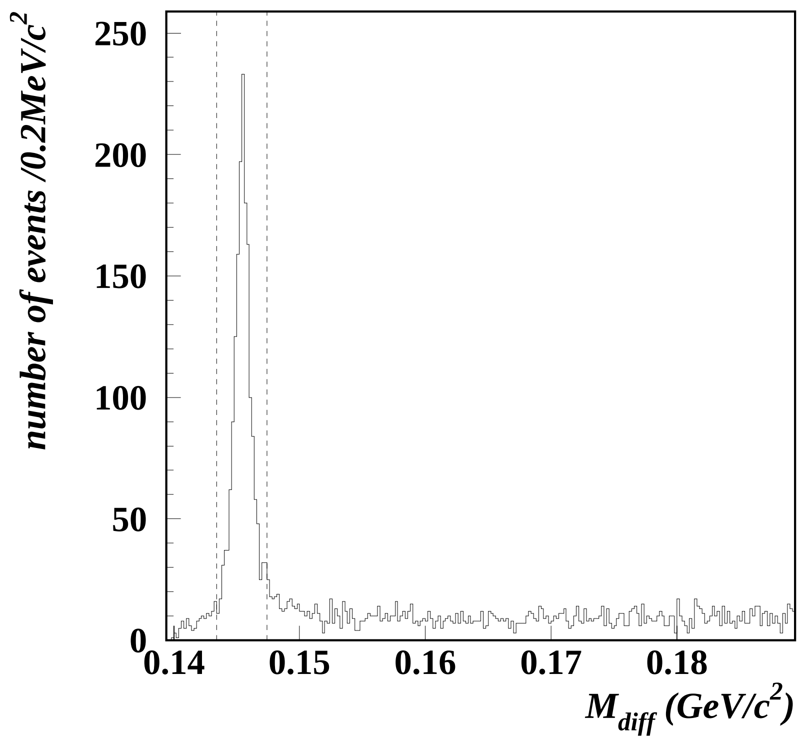

Figure A.2: The mass difference distribution for $D^{*\pm} \to D^0 \pi_s^{\pm}$.

A.1.4 Reconstruction of $B \to D^* \ell \nu$

$D^{*\pm}$ candidates are combined with $\mu^{\mp}$ or $e^{\mp}$ candidates which have opposite charge to the $D^{*\pm}$. Lepton candidates are required to satisfy $1.0 < p_\ell^* < 2.4\text{GeV}/c$, where p_ℓ^* is the momentum in the CMS.

To utilize the approximately massless characteristic of the ν, we calculate the following two values in the CMS,

$$MM^2 = (E_B - E_{D^*\ell})^2 - |\vec{p}_B|^2 - |\vec{p}_{D^*\ell}|^2 \quad (A.1)$$

$$C = 2|\vec{p}_B|\,|\vec{p}_{D^*\ell}| \quad (A.2)$$

where E_B and $|\vec{p}_B|$ are the energy and momentum of the B meson in the CMS, respectively. MM^2 is the measured missing mass squared. E_B and $|\vec{p}_B|$ are calculated from he beam energy and nominal B meson mass.

$$E_B = 5.29\text{GeV/c}^2$$

$$|\vec{p}_B| = \sqrt{E_B^2 - M_B^2} = 325\text{MeV/c} \tag{A.3}$$

$E_{D^*\ell}$ and $|\vec{p}_{D^*\ell}|$ are the sum of the energy and momenta of the $D^{*\pm}$ candidate and lepton candidate in the CMS. These two quantities are related to the mass of the accompanying ν as.

$$M_\nu = MM^2 + C\cos\Theta_{p_B p_{D^*\ell}}, \tag{A.4}$$

where $\Theta_{p_B p_{D^*\ell}}$ is the angle between $\vec{p}_B$ and $\vec{p_{D^*\ell}}$. Since $\Theta_{p_B p_{D^*\ell}}$ can not be measured and $\cos\Theta_{p_B p_{D^*\ell}}$ takes a value ranging between -1 and 1, equation (A.4) leads to the following relation,

$$C \geq |MM^2|. \tag{A.5}$$

We select $D^*\ell\nu$ candidates satisfying the following relations (in GeV/c^2):

$$\begin{aligned} C &\geq -\frac{1.5}{1.65}MM^2, \\ C &\geq \frac{1.2}{1.3}MM^2, \\ C &\leq -\frac{0.3}{2.95}(MM^2 + 1.65) + 1.5. \end{aligned}$$

Figure A.3 shows C vs. MM^2 distribution.

A.1.5 Vertex reconstruction of $D^*\ell\nu$

First, we fit the D vertex using the kaon and the pion tracks. Then we perform a vertex fitting of ℓ and D tracks to obtain the B vertex. The slow pion track from D^* is not used in the fit, since it does not help to improve B vertex resolution.

A.1.6 Flavor tagging and vertex reconstruction of tagging-side

In the tagging-side, the vertex reconstruction method and flavor tagging methods are the same as that of $B \to$ charmonium $+ K_S$.

Table A.1 shows the number of events for different tagging methods.

mode	OF events	SF events	Total
high p_ℓ^*	166	56	222
kaon	316	164	480
medium p_ℓ^*	29	34	63
slow $\pi^\pm$	73	59	132

Table A.1: *The number of signal event for each flavor tagging mode.*

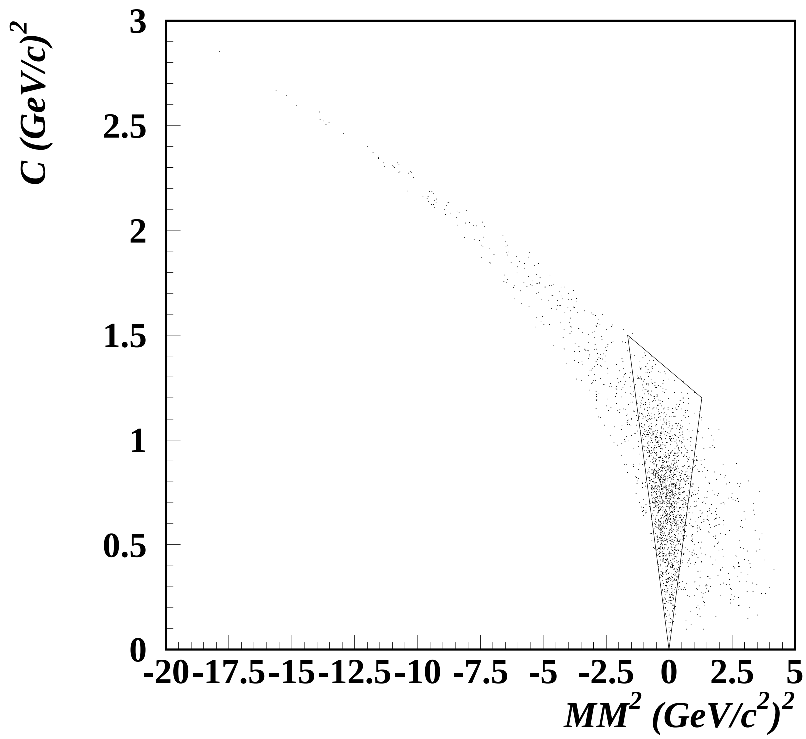

Figure A.3: The C vs. MM^2 distribution.

A.2 Estimation of background

Background events for the $D^*\ell\nu$ decay mode are divided into four categories:

- Combinatoric background in $D^{*\pm}$ reconstruction.
- Uncorrelated $D^{*\pm}$-lepton background. In this class of events the $D^{*\pm}$ and lepton come from different B mesons.
- Correlated $D^{*\pm}$-lepton background. In this case $D^{*\pm}$ and lepton have the same parent that can be either a neutral or charged B.
- Lepton fakes and continuum events

A.2.1 $D^{*\pm}$ combinatoric background

This type of background is further divided into two types. One is the combination of random $K^{\mp}\pi$ pairs and any pion including pions from real $D^{*\pm}$. The other is the combination of a correctly reconstructed D^0 and a random charged pion. We call the former type of background $K\pi$ combinatoric and the latter $D^0\pi$ combinatoric.

The $M_{K\pi}$ distribution of $K\pi$ combinatoric background does not peak at the mass of D^0 meson. We fitted $M_{K\pi}$ distributions of events without flavor tagging with a Gaussian signal plus linear background for each decay mode. The ratios of the number of the background events in the signal region to the upper sideband region are calculated. We define the sideband region as $1.91 < M_{K\pi} < 1.96\text{GeV}/c^2$. We obtained 0.8 as the ratio. We count the number of events in the upper sideband region and scale it with this ratio to estimate this type of background.

The $D^0\pi$ type of background does not have a peak in the M_{diff} distribution, but peaks at the mass of the D^0 meson. We use the M_{diff} upper sideband region to estimate this type of background. We use $0.16 < M_{diff} < 0.19\text{GeV}/c^2$ as this region. We count the number of events in this M_{diff} region and subtract the $K\pi$ combinatoric background using the same method we mentioned above. After that, the number of remaining events is scaled to the M_{diff} signal region and subtracted as this type of background. The scaling factor is determined by fitting the M_{diff} distribution of events without flavor tagging . Since the M_{diff} distribution has a long tail toward the higher M_{diff} region, we fit the sideband region with the background function, $a(M_{diff} - M_\pi)^{\frac{1}{2}} + b(M_{diff} - M_\pi)^{\frac{3}{2}}$ where a and b are free parameters, and extend it into the signal region. We obtained 0.06667 ± 0.00395 as the scaling factor.

A.2.2 Uncorrelated D^*-lepton background

Since the uncorrelated D^*-lepton background can have more energy than one B decay, their MM^2 can have a smaller value than the signal and correlated background. We use the region satisfying $C < 0.8|MM^2|$ and $MM^2 < 0$ to estimate this type of background. Except for combinatoric background, the events in this region are expected to be almost uncorrelated events. We count the number of events in this region and subtract the combinatoric background using the same method mentioned above. After that, the remaining number is scaled to the signal region. The scaling factor is determined with an Monte Carlo study to be $= 0.391 \pm 0.196$.

A.2.3 Correlated $D^{*\pm}$-lepton background

The correlated $D^{*\pm}$-lepton background comes from the decay of a charged or neutral B meson into $D^{*\pm}l^{\mp}\nu+anything$. For the neutral B meson, this background events are able to be treated as the signal events. For the charged B meson, this background is small. Therefore this background is negligible in extraction of w_{tag}. This effect is included in systematic error.

	The number of Signal	background fraction	the number of sideband
successful in flavor tagging	897	0.18 ± 0.05	193
failed in flavor tagging	824	0.14 ± 0.04	157

Table A.2: *The number of $D^*\ell\nu$ events and background fraction.*

A.2.4 Lepton fakes and continuum

Lepton fakes are rare enough to be neglected thanks to the good particle identification capability of Belle. Continuum events were also studied with about $0.6fb^{-1}$ continuum data. We performed the same analysis with this data sample, then the number of remaining events was scaled to the luminosity of $\Upsilon(4S)$ resonance. The scaling factor is 9.846.

A.2.5 Selection of background samples

We must decide background shape function to extract w. This function is estimated using the sideband region of $D^*\ell\nu$ in the real data. The sideband region is the same as that of uncorrelated background ($C < 0.8|MM^2|$ and $MM^2 < 0$).

A.3 Summary of reconstruction of $D^*\ell\nu$ decay

Table A.2 lists the number in the events in the signal and sideband region. We measured wrong tagging fraction using these events.

A.4 Extraction of wrong tagging fraction

A.4.1 Probability density functions

Taking into account the wrong tagging fraction, probability density function (PDF) of neutral B meson pair with the the opposite flavor (OF) and the same flavor (SF) is given by,

$$F^{OF}_{sig}(\Delta t) = \int_{-\infty}^{\infty} P^{OF}_{sig}(\Delta t')R_{sig}(\Delta t - \Delta t')d\Delta t', \quad (A.6)$$

$$F^{SF}_{sig}(\Delta t) = \int_{-\infty}^{\infty} P^{SF}_{sig}(\Delta t')R_{sig}(\Delta t - \Delta t')d\Delta t', \quad (A.7)$$

where,

$$P^{OF}_{sig}(\Delta t) = \frac{1}{4\tau_B} e^{-\frac{|\Delta t|}{\tau_B}} \left(1 + (1 - 2w_{tag}) \cos \Delta m_B \Delta t\right),$$

$$P^{SF}_{sig}(\Delta t) = \frac{1}{4\tau_B} e^{-\frac{|\Delta t|}{\tau_B}} \left(1 - (1 - 2w_{tag}) \cos \Delta m_B \Delta t\right),$$

$$
\begin{aligned}
R_{sig}(\Delta t) &= f_1 G(\Delta t;\mu_1,\sigma_1) + (1-f_1)G(\Delta t;\mu_2,\sigma_2),\\
\sigma_{1(2)} &= S_{1(2)}\sqrt{\sigma_{CP}^2+\sigma_{tag}^2},
\end{aligned}
$$

Δt is the proper time, $\Delta t = \Delta z/c\beta\gamma$, τ_B is the lifetime of B^0, w_{tag} is the wrong tagging fraction of flavor tagging, Δm is the mass difference between two mass eigenstates of B^0, defined as the equation (2.8), and $G(t;\mu.\sigma)$ is Gaussian defined as (5.5). PDF for background is the follows:

$$
\begin{aligned}
F_{bg}(\Delta t) &= \int_{-\infty}^{\infty} P_{bg}(\Delta t')R_{bg}(\Delta t-\Delta t')d\Delta t', \qquad (A.8)\\
P_{bg}(\Delta t) &= (1-f_p)\frac{1}{2\tau_{bg}}e^{-\frac{|\Delta t|}{\tau_B}} + f_p\delta(\Delta t),\\
R_{bg}(\Delta t) &= G(\Delta t;\mu_{bg},\sigma_{bg}),\\
\sigma_{bg} &= S_{bg}\sqrt{\sigma_{CP}^2+\sigma_{tag}^2}.
\end{aligned}
$$

A.4.2 Determination of resolution functions

First, resolution function of signal and background, R_{sig}, R_{bg} are determined using $B \to D^*\ell\nu$ events which were flavor-tagged successfully tagged B flavor. A likelihood function for fitting resolution functions is as follows:

$$
\begin{aligned}
L &= \prod_i [(1-f_{bg})F_{sig}(\Delta t_i) + f_{bg}F_{bg}(\Delta t_i)] \times \prod_j F_{bg}(\Delta t_j),\\
F_{sig}(\Delta t) &= \int_{-\infty}^{\infty} \frac{1}{2\tau_B}e^{-\frac{|\Delta t'|}{\tau_B}} R_{sig}(\Delta t-\Delta t')d\Delta t',
\end{aligned}
$$

where f_{bg} is a background fraction. Table A.3 shows the fitted result.

signal	μ_1	$(-0.16 \pm 0.11)\ ps$
	S_1	$0.95^{+0.16}_{-0.17}$
	f_1	$0.938^{+0.029}_{-0.041}$
	μ_2	$(-3.1^{+1.4}_{-1.7})\ ps$
	S_2	$5.8^{+1.6}_{-1.1}$
background	μ_{bg}	$(-0.12 \pm +0.16)\ ps$
	S_{bg}	$1.51^{+0.33}_{-0.39}$
	τ_{bg}	$(1.62^{+0.34}_{-0.24})\ ps$
	f_p	$0.21^{+0.27}_{-0.21}$

Table A.3: *Parameters of resolution functions for signal and background.*

A.4.3 Measurement of w_{tag}

The PDF used in the fitting is as follows,

$$
\begin{aligned}
F_{OF}(\Delta t) &= (1-f_{bg})F_{sig}^{OF}(\Delta t) + f_{OF}f_{bg}F_{bg}(\Delta t),\\
F_{SF}(\Delta t) &= (1-f_{bg})F_{sig}^{SF}(\Delta t) + (1-f_{OF})f_{bg}F_{bg}(\Delta t),
\end{aligned} \qquad (A.9)
$$

where f_{bg} is a background fraction and f_{OF} is the OF state fraction of background. We estimated f_{OF} with the real data, and obtained to be $f_{OF} = 0.6144 \pm 0.1383$.

A likelihood function is

$$L = \prod_i F_{OF}(\Delta t_i) \times \prod_j F_{SF}(\Delta t_j). \qquad \text{(A.10)}$$

A.5 Systematic errors for the estimation of wrong tagging fraction

A.5.1 Physics parameters

The world average value of the B meson lifetime is [19]

$$\tau_B = (1.548 \pm 0.032) \times 10^{-12} sec. \qquad \text{(A.11)}$$

We estimated the systematic error from B lifetime by varying the lifetime of B meson within the error shown above.

The effect of B^0-$\bar{B}^0$ mixing parameter, Δm, was also estimated with the same method. The world average value is

$$\Delta m = (0.472 \pm 0.017) \times 10^{12}\ \hbar s^{-1}. \qquad \text{(A.12)}$$

A.5.2 Signal and background resolution functions

Resolution functions of signal and background are obtained from the simultaneous fit of the proper time distribution of $B \to D^* \ell \nu$ sample. Error of the parameters of resolution functions is estimated in Table A.3. We varied these parameters within its errors independently, and we refit the resolution functions with all the others floated. Using the modified resolution function obtained we finally refit the wrong tagging fraction.

A.5.3 Background fraction, f_{bg} and f_{OF}

We varied these parameters within its errors independently, and we first refit the resolution functions and then refit the wrong tagging fraction.

A.5.4 Correlated background from the decay of a charged B meson

Correlated background from the decay of a charged B meson was negligible. The difference between wrong tagging fractions with and without taking into account of this background is included in the systematic error.

A.5.5 B flight length

The IP constrained fit includes the uncertainty of the B decay point due to B flight length in the r-ϕ plane. The uncertainty is estimated to be $\sim 20\mu m$ assuming a Gaussian function. The uncertainty was varied by $\pm 10\mu m$ and we repeated the analysis to estimate the error.

A.5.6 Summary

Table A.4 lists systematic errors described above. The largest error is due to uncertainty in the f_{OF}.

	high p_ℓ^*		$K^\pm$		medium p_ℓ^*		slow $\pi^\pm$	
w_{tag}	0.081		0.212		0.415		0.362	
Statistics	+0.0433	-0.0396	+0.0346	-0.0334	+0.1002	-0.0973	+0.0696	-0.0677
Systematic	+0.0394	-0.0395	+0.0370	-0.0362	+0.0419	-0.0354	+0.0372	-0.0370
Lifetime	+0.0011	-0.0009	+0.0016	-0.0013	+0.0063	-0.0060	+0.0034	-0.0032
ΔM_B	+0.0054	-0.0049	+0.0042	-0.0038	+0.0090	-0.0088	+0.0051	-0.0050
R_{sig}	+0.0026	-0.0026	+0.0044	-0.0034	+0.0019	-0.0015	+0.0093	-0.0079
R_{bg}	+0.0064	-0.0065	+0.0042	-0.0055	+0.0014	-0.0007	+0.0025	-0.0017
f_{bg}	+0.0161	-0.0176	+0.0077	-0.0087	+0.0031	-0.0026	+0.0006	-0.0008
f_{OF}	+0.0347	-0.0343	+0.0344	-0.0343	+0.036	-0.0335	+0.0354	-0.0355
correlated BG	+0.004	-0.000	+0.008	-0.000	+0.013	-0.000	+0.000	-0.003
B flight length	+0.000	-0.0006	+0.0003	-0.0004	+0.0003	-0.00055	+0.0006	-0.0007
Total	+0.059	-0.052	+0.051	-0.049	+0.109	-0.105	+0.079	-0.077

Table A.4: *Error estimation of wrong tagging fraction for each flavor tagging method*

Appendix B

Fit ΔE and M_{bc} distributions for $B^0 \to \psi(2S)K_S$ and $B^0 \to \chi_{c1}K_S$

When we calculate the background fraction for each event, the distribution functions of ΔE and M_{bc} are used as we mentioned in Section 5.1.3. For $B^0 \to \psi(2S)K_S$ and $B^0 \to \chi_{c1}K_S$, these functions are estimated from Monte Carlo data. These distributions are shown in Figure B.1-B.3.

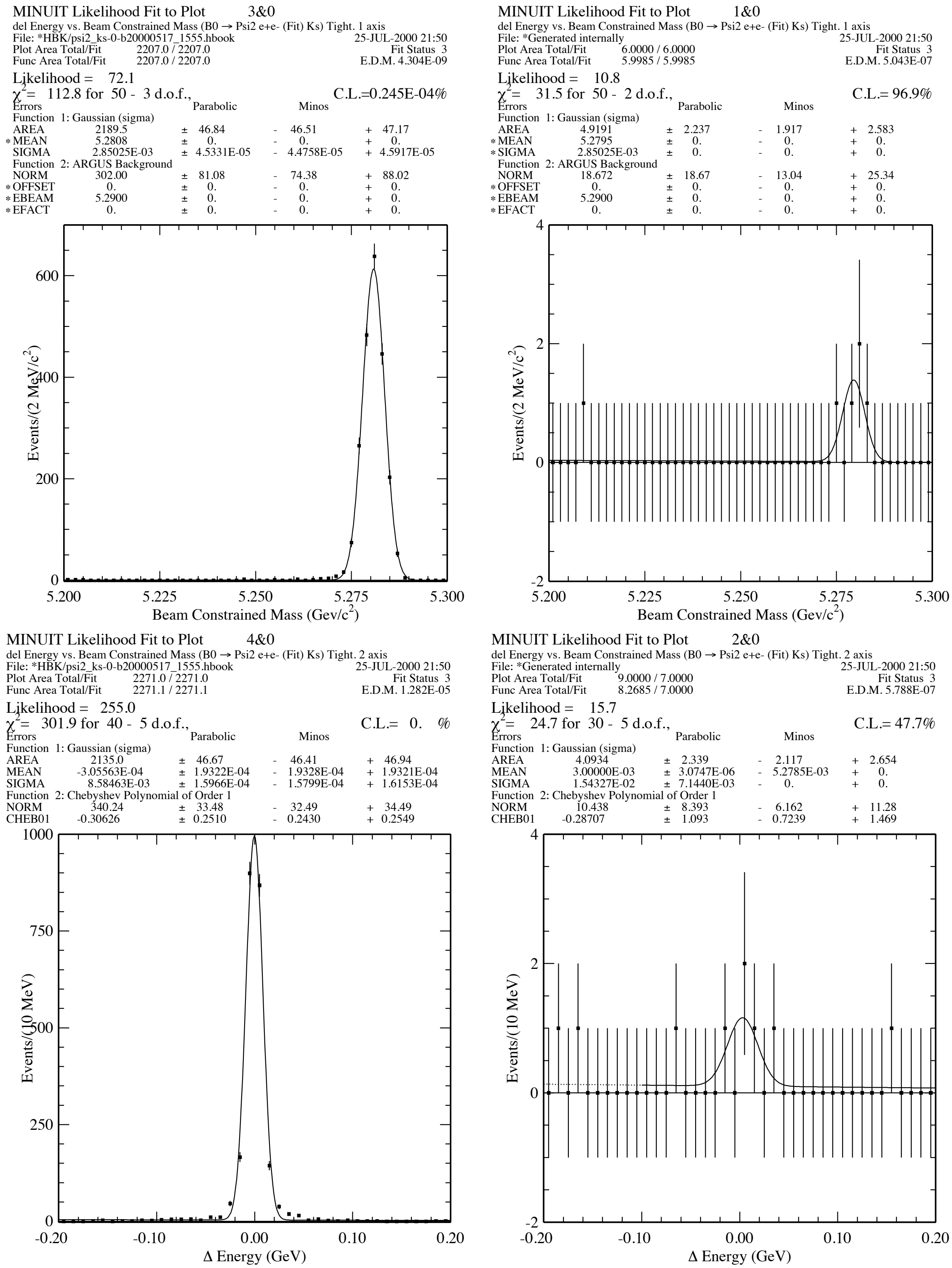

Figure B.1: *Results from fitting ΔE and M_{bc} distributions for $B^0 \to \psi(2S)K_S$, $\psi(2S) \to \ell^+\ell^-$. Top-left figure shows M_{bc} distribution from MC and top-right figure shows M_{bc} distribution from real data. Bottom-left figure shows ΔE distribution from MC and bottom-right figure shows ΔE distribution from real data.*

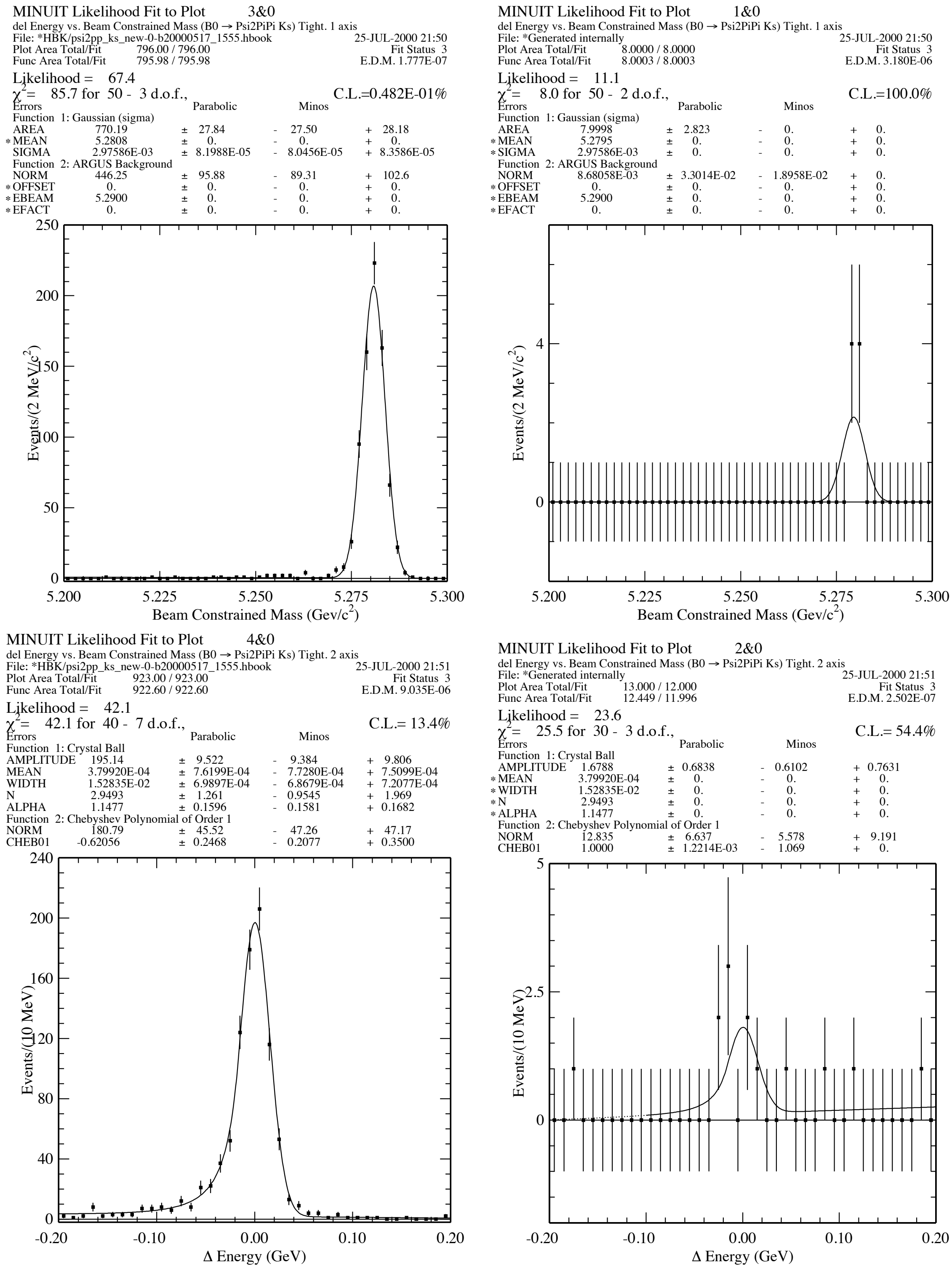

Figure B.2: *Results from fitting ΔE and M_{bc} distributions for $B^0 \to \psi(2S)K_S$, $\psi(2S) \to J/\psi\pi^+\pi^-$. Top-left figure shows M_{bc} distribution from MC and top-right figure shows M_{bc} distribution from real data. Bottom-left figure shows ΔE distribution from MC and bottom-right figure shows ΔE distribution from real data.*

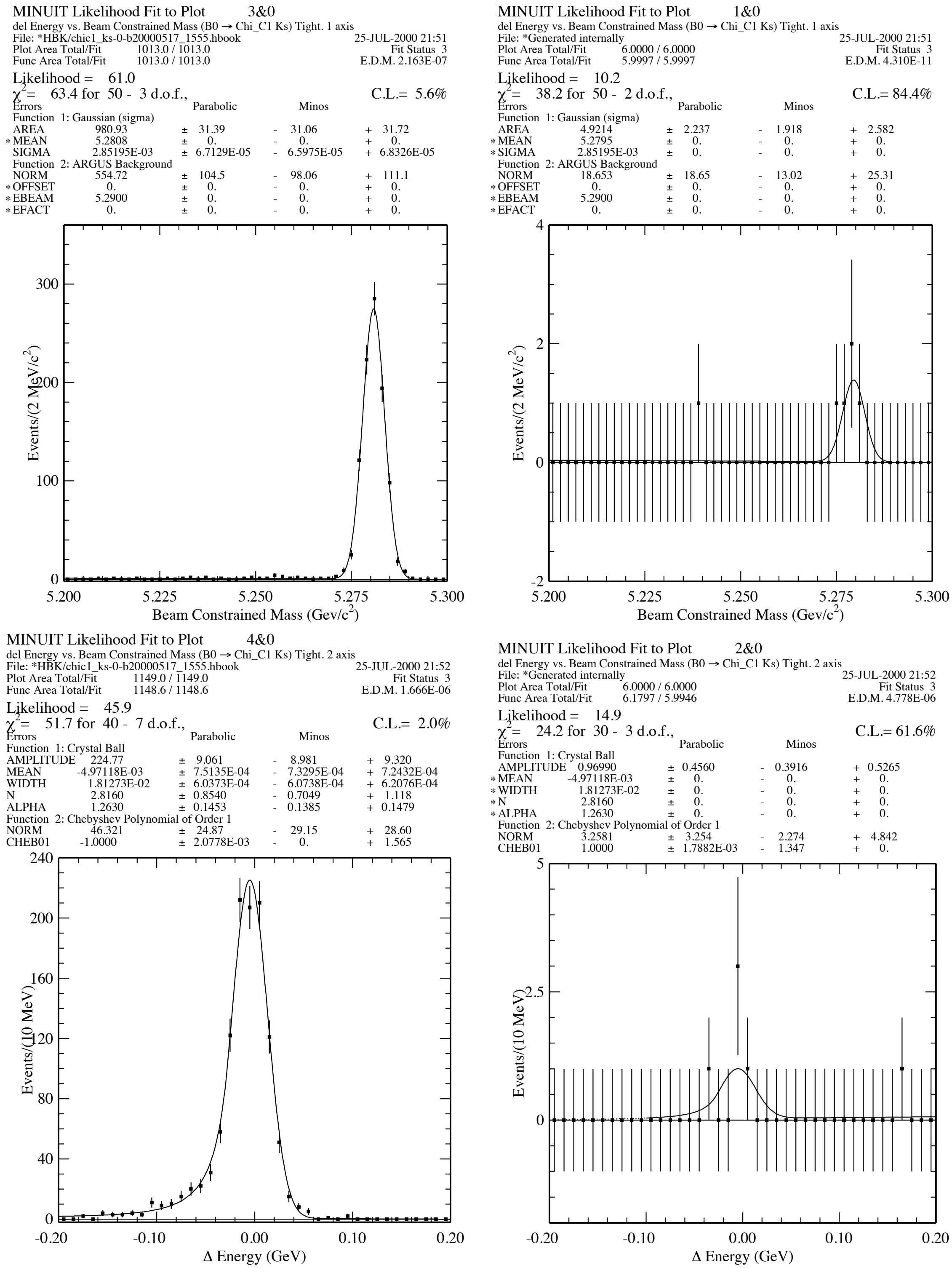

Figure B.3: *Results from fitting ΔE and M_{bc} distributions for $\chi_{c1}K_S$. Top-left figure shows M_{bc} distribution from MC and top-right figure shows M_{bc} distribution from real data. Bottom-left figure shows ΔE distribution from MC and bottom-right figure shows ΔE distribution from real data.*

Appendix C

Statistics

C.1 Bayesian method

Bayes' theorem plays an important role to explain Bayesian method. Hence brief introduction of Bayes' theorem is given first.

The marginal probability density function (PDF) of x (the distribution of x with y unobserved) is

$$P_1(x) = \int_{-\infty}^{\infty} f(x,y)dy, \tag{C.1}$$

and similarly for the marginal PDF $P_2(y)$. We define the conditional PDF of x, given fixed y, by

$$f_1(y|x)P_1(x) = f(x,y). \tag{C.2}$$

Similarly, the conditional PDF of y, given fixed x, is

$$f_2(x|y)P_2(y) = f(x,y). \tag{C.3}$$

From these definitions we immediately obtain Bayes' theorem[64]:

$$f_2(x|y) = \frac{f_1(y|x)P_1(x)}{P_2(y)} = \frac{f_1(y|x)P_1(x)}{\int f_1(y|x)P_1(x)dx}. \tag{C.4}$$

Next, we introduce how to get confidence intervals in the Bayesian method. Suppose that we wish to make an inference about a parameter α whose true value is fixed but unknown. Assume that we do this by making a single measurement of an observable x such that the PDF for obtaining the value x depends on the unknown parameter α in a known way: we call this PDF $f(x|\alpha)$. (Note that x needs not be a measurement of α, though that is often the case; x just needs to be some observable whose PDF depends on α.) Our measurements provide $f(x|\alpha)$, while we really want to know $g(\alpha|x)$, which tells us that, given our measurement x, the "true answer" α lies between α and $\alpha + d\alpha$ with probability $g(\alpha|x)d\alpha$. The connection is provided by the Bayes' theorem expressed by equation (C.4):

$$g(\alpha|x) = \frac{f(x|\alpha)P(\alpha)}{\int f(x|\alpha)P(\alpha)d\alpha}, \tag{C.5}$$

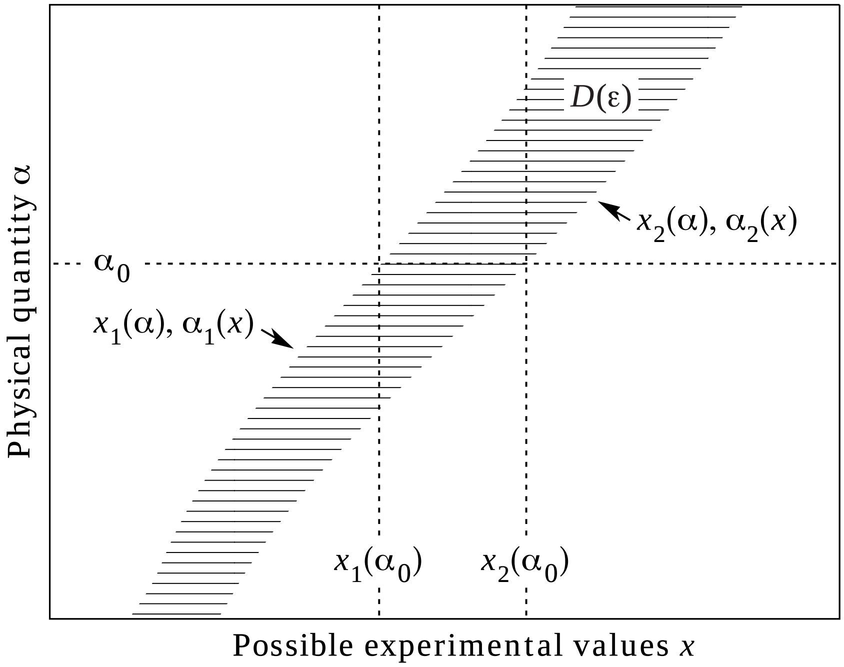

Figure C.1: *Confidence intervals for a single unknown parameter* α. *One might think of the PDF* $f(x|\alpha)$ *as being plotted out of the paper as a function of* x *along each horizontal line of constant* α. *The domain* $D(\varepsilon)$ *contains a fraction* ε *of the area under each of these functions.*

where $P(\alpha)$ is called *prior* PDF. A Bayesian interval $[\alpha_1, \alpha_2]$ corresponding to a confidence level ε can be constructed by requiring

$$\int_{\alpha_1}^{\alpha_2} g(\alpha_t|x) d\alpha_t = \varepsilon. \tag{C.6}$$

The Bayesian concept of probability is not based on limiting frequencies, but is more general and includes *degrees of belief*. It can therefore be used for experiments which cannot be repeated, where a frequency definition of probability would not be applicable (for example, one can consider the probability that it will rain tomorrow). Bayesian methods also allow for a natural way to input additional information such as physical boundaries and subjective information; in fact they *require* as input the *prior distribution* for any parameter to be estimated.

The Bayesian methodology, while well adapted to decision-making situations, is not in general appropriate for the objective presentation of experimental data. Nonetheless it is often used with the flat prior PDF which is still useful when one compares more than one experiments.

C.2 Feldman-Cousins method

Frequentist intervals are obtained with a construction due to Neyman[65]. Feldman-Cousins method is more general method than Neyman one. This method produces confidence intervals with better properties in the neighborhood of a physical limit.

We consider the parameter α whose true value is fixed but unknown. The properties of our experimental apparatus are expressed in the function $f(x|\alpha)$ which gives the probability of observing data x if the true value of the parameter is α. This function must be known in order to interpret the results of an experiment. For a large complex experiment, f is usually determined numerically using Monte Carlo simulation.

Given $f(x|\alpha)$, we can find for every value of α, two values $x_1(\alpha,\varepsilon)$ and $x_2(\alpha,\varepsilon)$ such that

$$P(x_1 < x < x_2|\alpha) = \varepsilon = \int_{x_1}^{x_2} f(x|\alpha)dx. \tag{C.7}$$

This is shown graphically in Figure C.1[19]: a horizontal line segment $[x_1(\alpha,\varepsilon), x_2(\alpha,\varepsilon)]$ is drawn for representative value of α. The union of all intervals $[x_1(\alpha,\varepsilon), x_2(\alpha,\varepsilon)]$, designated in the figure as the domain $D(\varepsilon)$, is known as the *confidence belt*. Typically the curves $x_1(\alpha,\varepsilon)$ and $x_2(\alpha,\varepsilon)$ are monotonic functions of α, which we assume for this discussion.

Upon performing an experiment to measure x and obtaining the value x_0, one draws a vertical line through x_0 on the horizontal axis. The confidence interval for α is the union of all values of α for which the corresponding line segment $[x_1(\alpha,\varepsilon), x_2(\alpha,\varepsilon)]$ is intercepted by this vertical line. The confidence interval is an interval $[\alpha_1(x_0), \alpha_2(x_0)]$, where $\alpha_1(x_0)$ and $\alpha_2(x_0)$ are on the boundary of $D(\varepsilon)$. Thus the boundaries of $D(\varepsilon)$ can be considered to be functions $x(\alpha)$ when constructing D, and then to be functions $\alpha(x)$ when reading off confidence intervals.

Now suppose that some unknown particular value of α, say α_0 (indicated in the figure), is the true value of α. We see from the figure that α_0 lies between $\alpha_1(x)$ and $\alpha_2(x)$ if and only if x lies between $x_1(\alpha_0)$ and $x_2(\alpha_0)$. Therefore we can write:

$$P[x_1(\alpha_0) < x < x_2(\alpha_0)] = \varepsilon = P[\alpha_2(x) < \alpha_0 < \alpha_1(x)]. \tag{C.8}$$

And since, by construction, this is true for any value α_0, we can drop the subscript 0 and obtain the confidence interval:

$$P[\alpha_2(x) < \alpha < \alpha_1(x)] = \varepsilon. \tag{C.9}$$

Method to determine x_1 and x_2 is different between the Neyman method and the Feldman-Cousins one. We explain how to determine x_1 and x_2 in the Feldman-Cousins in the following.

As an example, we consider that α is physically bounded to non-negative values, and conditional PDF $f(x|\alpha)$ is described by the Gaussian function with known fixed *r.m.s.* deviation σ. In convenience, we set σ to unity, *i.e.*:

$$P(x|\alpha) = \frac{1}{\sqrt{2\pi}} \exp(-(x-\alpha)^2/2). \tag{C.10}$$

For the particular x, we let α_{best} be the physically allowed value of α for which $P(x|\alpha)$ is maximum. Then

$$\alpha_{best} = \begin{cases} x, & x \geq 0, \\ 0, & x < 0, \end{cases} \tag{C.11}$$

$$P(x|\alpha_{best}) = \begin{cases} \frac{1}{\sqrt{2\pi}}, & x \geq 0, \\ \frac{\exp(-x^2/2)}{\sqrt{2\pi}}, & x < 0, \end{cases} \tag{C.12}$$

We then compute R using the equation (C.10) and (C.12):

$$R(x) = \frac{P(x|\alpha)}{P(x|\alpha_{best})} = \begin{cases} \exp(-(x-\alpha)^2/2), & x \geq 0, \\ \exp(x\alpha - \alpha^2/2), & x < 0, \end{cases} \tag{C.13}$$

For a given value of α, we find the interval $[x_1, x_2]$ such that $R(x_1) = R(x_2)$ and the equation (C.7).

In this probability statement, α_1 and α_2 are the random variables (not α), and we can verify that the statement is true, as a limiting ratio of frequencies in random experiments, for any assumed value of α. In a particular real experiment, the numerical values α_1 and α_2 are determined by applying the algorithm to the real data. Note that the probability statement is often misinterpreted to be a statement about the true value α for that one needs to have the prior distribution $P(\alpha)$ which is objectively unknown. It should be interpreted as the probability of obtaining values α_1 and α_2 which include the true value of α, in an ensemble of identical experiments.

The detail of the Feldman-Cousins method is described in [66].

Bibliography

[1] A. D. Sakharov, JETP Lett. 5, 24 (1967).

[2] L. H. Christenson, J. W. Cronin, V. L. Fitch, and R. Turlay, Phys. Rev. Lett. **13**, 138 (1964).

[3] M. Kobayashi and T. Maskawa, Prog. Theor. Phys. **49**, 652 (1973).

[4] A. Carter and Phys. A. I. Sanda, Rev. Lett. **45**, 952 (1980); Phys. Rev. **D23**, 1567 (1981); I. I. Bigi and A. I. Sanda, Nucl. Phys. **193**, 851 (1981).

[5] P. Oddone, Proceedings of the UCLA Workshop: Linear Collider $B\bar{B}$ Factory Conceptual Design, edit by D. Stork, World Scientific, 243 (1987).

[6] The BaBar collaboration. Technical Design Report, (1995).

[7] T. Lohse *et al.*, DESY-PRC 94/02, (1994).

[8] "The CDF II Detector, Technical Design Report", FERMILAB-Pub-96/390-E, November 1996; The D0 Upgrade: "The Detector and its Physics", FERMILAB-Pub-96/357-E, October 1996.

[9] LHC-B Letter of Intent, CERN/LHCC 95-5, LHCC/18, August 1995.

[10] W. Pauli. In Niehls Bohr and the Development of Physics, Oxford, Pergamon 2nd edition (1995).

[11] T. D. Lee and C. N. Yang, Phys. Rev. **104**, 254 (1956).

[12] C. S. Wu *et al.*, Phys. Rev. **105**, 1413 (1957).

[13] R. L. Garwin, L. M. Lederman, and M. Weinrich, Phys. Rev. **105**, 1415 (1957).

[14] J. I. Friedman and V. L. Telegdi, Phys. Rev. **106**, 1290 (1957).

[15] Gaillard *et al.*, Phys. Rev. Lett. **18**, 20 (1967); Cronin *et al.*, Phys. Rev. Lett. **18**, 25 (1967).

[16] S. Bennett *et al.*, Phys. Rev. Lett. **19**, 993 (1967).

[17] D. Dorfan *et al.*, Phys. Lett. **19**, 983 (1967).

[18] I. I. Bigi and A. I. Sanda, Phys. Rev. **D60**, 033001 (1999).

[19] Review of Particle Physics, D. Groom *et al*, Eur. Phys. J. **C 15** (2000) 1.

[20] C. Jarlskog, in: CP Violation, edit by C. Jarlskog (World Scientific, Singapore, 1989).

[21] C. Jarlskoog, Phys. Rev. Lett. **55**, 1039 (1985); Z. Phys. C **29**, 491(1985).

[22] L. Wolfenstein, Phys. Rev. Lett. **51**, 1945 (1983).

[23] H. Auinn and A. I. Sanda, Eur. Phys. J. **C 15**, 626 (2000).

[24] M. Neubert, Int. J. Mod. Phys. **A 11** (1998), 4173.

[25] Y. Nir and H. R. Quinn, in: B decays, edit by S. Stone (World Scientific, Singapore, 1994).

[26] A. J. Buras, M. Jamin, and P. H. Weisz, Nucl. Phys. **B347**, 491 (1990).

[27] T. Inami and C. S. Lim, Prog. Theor. Phys. **65**, 297 and 1772 (1981); A. J. Buras, Phys. Rev. Lett. **46**, 1354 (1981).

[28] M. Neubert, Phys. Rev. **D51**, 5101 (1995).

[29] C. T. Sachrajda, in: B decays, edit by S. Stone (World Scientific, Singapore, 1994).

[30] A. Abada *et al.*, Nucl. Phys. **B376**, 172 (1992).

[31] C. Sachradja. "Heavy Flavour Physics", XVIII International Symposium on Lepton and Photon Interactions, July 1997, Hamburg, Germany.

[32] The BABAR Collaboration, BABAR-CONF-00/01 (2000).

[33] F. J. Gilman, K. Kleinknecht, and B. Renk, Eur. Phys. J. **C 15**, 110 (2000).

[34] F. Caravaglios, F. Parodi, P. Roudeau, and A. Stocchi, hep-ph/0002171 (2000).

[35] Pietro Faccioli, hep-ph/0011269 (2000).

[36] K. Ackerstaff *et al.* (OPAL Collaboration). CERN-EP-98-001 Jan (1998); Eur. Phys. J. **C 5** (1998) 3, 379.

[37] T. Affolder *et al.* (CDF Collaboration), Phys. Rev. **D61**, 072005 (2000).

[38] R. Barate *et al.* (ALEPH Collaboration). CERN-EP-2000-119, Sep 2000.

[39] H. Aihara (Belle Collaboration), hep-ex/0010008 (2000).

[40] KEK B-Factory Design Report, KEK Report 95-7 (1995): H. Fukuma *et al.*, European Particle Accelerator Conference (2000).

[41] BELLE Collaboration, Technical Design Report, KEK Report 95-1: BELLE Collaboration, BELLE Progress Report, KEK Report 96-1: BELLE Collaboration, BELLE Progress Report, KEK Report 97-1.

[42] "BELLE SVD Technical Design Report": `http://bsunsrv1.kek.jp/~svd/tdr/tdr.ps` (1998).

[43] H. Hirano. PhD thesis, Tokyo University of Agriculture and Technology, September 2000.

[44] H. Ikeda *et al.*, Nucl. Instr. and Meth. **A441**, 401 (2000).

[45] R. Itoh and S. Ichizawa, BELLE note 97 (1996).

[46] R. Itoh, BELLE note 161 (1996).

[47] S. Nagayama, "Panther - User's guide -": `http://bsunsrv1.kek.jp/~nagayama/panther/` (1997).

[48] H. Ozaki, BELLE note 146 (1996).

[49] See `http://www.lns.cornell.edu/public/CLEO/soft/QQ`.

[50] R. Itoh, "QQ quick reference for BELLE": `http://bsunsrv1.kek.jp/~software/qq/html/belle_qq.html` (1996).

[51] T. Sjöstrand, Computer Physics Commun. **82**, 74 (1994).

[52] B. Anderson *et al.*, Phys. Rep. **97**, 31 (1983).

[53] GEANT detector Description and Simulation Tool, CERN Program Library Long Writeup W0513.

[54] G. Fox and S. Wolfram, Phys. Rev. Lett. **41**, 1581 (1978).

[55] K. Hanagaki *et al.*, BELLE note 312 (2000).

[56] L. Piilonen *et al.*, BELLE note 338 (2000).

[57] H. Hamasaki *et al.*, BELLE note 321 (2000).

[58] CLEO Collaboration, CLNS 00/1688 (2000).

[59] CLEO Collaboration, CLNS 00/1671 (2000).

[60] D. Coffman *et al.* (MARK III collaboration), Phys. Rev. Lett. **68**, 3 (1992).

[61] Flavor Tagging group, BELLE note 320 (2000).

[62] H. Albrecht *et al.* (ARGUS Collaboration), Phys. Lett. **B241**, 278 (1990).

[63] T. Skwarnicki, PhD thesis, Institute for Nuclear Physics, Krakow 1986;
I. C. Brock, "Mn_Fit" homepage :
`http://www-zeus.physik.uni-bonn.de/~brock/mn_fit.html`.

[64] A. Stuart and A. K. Ord, Kendall's Advanced Theory of Statistics, Vol. 1 Distributioin Theory 5th Ed., (Oxford Univ. Press, New York, 1987).

[65] J. Neyman, Phil. Trans. Royal Soc. London, Series A, **236**, 333 (1937).

[66] G. J. Feldman and R. D. Cousins, Phys. Rev. **D57**, 3873 (1998).